INTEGRATED DESIGN OPTIMIZATION METHODS FOR OPTIMAL SENSOR PLACEMENT AND COOLING SYSTEM ARCHITECTURE DESIGN FOR ELECTRO-THERMAL SYSTEMS

BY

SATYA RAVI TEJA PEDDADA

THESIS

Submitted in partial fulfillment of the requirements
for the degree of Master of Science in Systems and Entrepreneurial Engineering
in the Graduate College of the
University of Illinois at Urbana-Champaign, 2018

Urbana, Illinois

Adviser:

Associate Professor James T. Allison

Abstract

Dynamic thermal management plays a very important role in the design and development of electro-thermal systems as these become more active and complex in terms of their functionalities. In highly power dense electronic systems, the heat is concentrated over small spatial domains. Thermal energy dissipation in any electrified system increases the temperature and might cause component failure, degradation of heat sensitive materials, thermal burnouts and failure of active devices. So thermal management needs to be done both accurately (by thermal monitoring using sensors) and efficiently (by applying fluid-based cooling techniques). In this work, two important aspects of dynamic thermal management of a highly dense power electronic system have been investigated.

The first aspect is the problem of optimal temperature sensor placement for accurate thermal monitoring aimed toward achieving thermally-aware electrified systems. Strategic placement of temperature sensors can improve accuracy of real-time temperature distribution estimates. Enhanced temperature estimation supports increased power throughput and density because Power Electronic Systems (PESs) can be operated in a less conservative manner while still preventing thermal failure. This work presents new methods for temperature sensor placement for 2- and 3-dimensional PESs that 1) improve computational efficiency (by orders of magnitude in at least one case), 2) support use of more accurate evaluation metrics, and 3) are scalable to high-dimension sensor placement problems. These new methods are tested via sensor placement studies based on a 2-kW, 60Hz, single-phase, Flying Capacitor Multi-Level (FCML) prototype inverter. Information-based metrics are derived from a reduced-order Resistance-Capacitance (RC) lumped parameter thermal model. Other more general metrics and system models are possible through application of a new continuous relaxation strategy introduced here for placement representation. A new linear programming

(LP) formulation is presented that is compatible with a particular type of information-based metric. This LP strategy is demonstrated to support efficient solution of finely-discretized large-scale placement problems. The optimal sensor locations obtained from these methods were tested via physical experiments. The new methods and results presented here may aid the development of thermally-aware PESs with significantly enhanced capabilities.

The second aspect is to design optimal fluid-based thermal management architectures through enumerative methods that help operate the system efficiently within its operating temperature limits using the minimum feasible coolant flow level. Expert intuition based on physics knowledge and vast experience may not be adequate to identify optimal thermal management designs as systems increase in size and complexity. This work also presents a design framework supporting comprehensive exploration of a class of single phase fluid-based cooling architectures. The candidate cooling system architectures are represented using labeled rooted tree graphs. Dynamic models are automatically generated from these trees using a graph-based thermal modeling framework. Optimal performance is determined by solving an appropriate fluid flow distribution problem, handling temperature constraints in the presence of exogenous heat loads. Rigorous case studies are performed in simulation, with components having variable sets of heat loads and temperature constraints. Results include optimization of thermal endurance for an enumerated set of 4,051 architectures. In addition, cooling system architectures capable of steady-state operation under a given loading are identified. Optimization of the cooling system design has been done subject to a representative mission, consisting of multiple time-varying loads. Work presented in this thesis clearly shows that the transient effects of heat loads are expected to have important impacts on design decisions when compared to steady state operating conditions.

To all my teachers, friends and family members for their love and support.

Acknowledgments

I am immensely grateful to my research advisor Professor James Allison for his constant encouragement and support. Without his dedicated guidance this would have been an impossible task. I greatly admire the way he patiently helped me throughout the course of this program.

I am also very thankful to the members of the Engineering Systems Design Laboratory for both their invaluable suggestions and significant feedback on my research. It was a great experience learning from each one of them. In this regard, I would like to sincerely thank Daniel Herber and Danny Lohan for their assistance in my graduate studies. In addition to them, I would also like to thank Yong Hoon Lee, Anand Deshmukh, Albert Patterson, Tinghao Guo, Madhav Arora, and Junwu Zhang for being such good colleagues at work.

Special thanks to Professor Andrew Alleyne, Center Director for the National Science Foundation (NSF) Engineering Research Center Power Optimization of Electro Thermal Systems (POETS) along with his graduate students, Pamela Tannous and Herschel Pangborn, with whom I thoroughly enjoyed collaborating on several interesting research projects. I also enjoyed working with both Jessica Perez, Education Director and Joe Muskin, Education Co-ordinator at POETS in organizing several STEM outreach activities in and around the campus. I also would like to thank Jodi Gritten, POETS Office Manager and the Department of Industrial and Enterprise Systems Engineering (ISE) faculty members for offering both academic and administrative support whenever I needed.

I sincerely acknowledge the financial support I received from the National Science Foundation Engineering Research Center Power Optimization of Electro Thermal Systems which helped me carry out my research in a smooth fashion.

Last but not the least I am indebted to all my loving teachers and family

members for their constant encouragement and support from India.

TABLE OF CONTENTS

List of Tables

List of Figures

LIST OF ABBREVIATIONS

SIMP	Solid Isotropic Micro-structure with Penalization
MEA	More Electric Aircraft
AES	All Electric Ship
PEV	Plugged-in Electric Vehicle
HEV	Hybrid Electric Vehicle
BEV	Battery Electric Vehicle
OSP	Optimal Sensor Placement
DTM	Dynamic Thermal Management
OEM	Original Equipment Manufacturer
ESS	Energy Storage Systems
IDG	Integrated Drive Generator
WSN	Wireless Sensor Network
NoC	Network on Chip
SoC	System on Chip
ICE	Internal Combustion Engine
EPA	Environmental Protection Agency
EWIS	Electric Wiring Interconnection System
HUMS	Health Utilization and Monitoring Systems
KW	Kilo Watts
MW	Mega Watts

MAC	Modal Assurance Criterion
FIM	Fisher Information Matrix
SHM	Structural Health Monitoring
LQR	Linear Quadratic Regulator
CPS	Cyber Physical System
LPDE	Low Power Density Electronics
HPDE	High Power Density Electronics
PCB	Printed Circuit Board
FCML	Flying Capacitor Multi-Inverter
LP	Linear Programming
MOR	Model Order Reduction
RC	Resistor Capacitor
EFI	Effective Independence
PES	Power Electronic Systems
AC	Alternating Current
DC	Direct Current
FR4	Flame Retardant 4
MOR	Model Order Reduction
LTI	Linear and Time Invariant
FLIR	Forward Looking Infra Red
IR	Infra Red
CPHX	Cold Plate Heat Exchanger
LLHX	Liquid-to-Liquid Heat Exchanger

LIST OF SYMBOLS

R	Electrical Resistance
ρ	Electrical Resistivity
CO_2	Carbon Dioxide
NO_x	Nitrogen x-Oxide
t_{end}	Thermal endurance
N_c	Number of CPHXs
N_f	Number of parallel flows
V_{AC}	AC Voltage
V_{DC}	DC Voltage
K_{Al}	Thermal Conductivity of Aluminium
C	Thermal Capacitance
c	Specific Heat Capacity
V	Region volume
R_{cond}	Thermal Resistance of conducting substance
L	Length of heat conducting body
K	Thermal Conductivity of material
R_{conv}	Convective Resistance
h	Heat transfer coefficient
A_s	Cross-sectional area of surface
A_c	Cross-sectional area of conductive material

C_k	Thermal capacitance at node k
T_k	Temperature at node k
q_k	Net heat flow into node k
T_a	Ambient Temperature
ρ	Material Density
R_{ck}	Conductive heat transfer resistance at node k
Q_s	Heat input from the current source connected to node k
$\dot{\mathbf{x}}$	Derivative of a state vector
$\mathbf{x}$	State vector
$\mathbf{u}$	Input vector
$\mathbf{d}$	Disturbance vector
$\mathbf{e}$	Noise vector
A	System dynamics matrix
B	Input matrix
C	Output matrix
V	Disturbance Matrix
D	Input matrix on the output equation
W	Output noise matrix
$R_{t,o}$	Overall effective convection resistance
η_o	Overall efficiency
A_t	Total surface area of the surface
A_f	Surface area of fins
N	Number of fins
η_f	Efficiency of a fin
A_b	Exposed base area
L_c	Corrected length
t	Thickness

m	Model parameter
$W_{o,linear}$	Linear Observability gramian
σ_i	Singular value of a matrix
Q_o	Observability matrix
r_i	Sensor design variable at location i
G	Graph
N_v	Number of vertices in a graph
N_e	Number of edges in a graph
P_j	Rate of heat transfer at node j
$\mathbf{P^s}$	Power loads
$\dot{\mathbf{m}}$	Mass flow rate
$\mathbf{T}$	Temperature vector states
$\dot{\mathbf{m}}_\mathbf{f}$	Mass flow rate in a parallel channel
$\mathbf{T^t}$	Sink temperature state
$\dot{m}_t$	Mass flow rate in tank
$S(n)$	Sum of partition numbers
$T_{w,0}$	Initial Temperature of the cold plate walls
$T_{f,0}$	Initial Temperature of the cold plate fluids
$T_{l,0}$	Initial Temperature of the cold plate tank and LLHX states
$\mathbf{T_{w,max}}$	Maximum allowable temperatures of the cold plate walls
$\mathbf{T_{f,max}}$	Maximum allowable temperatures of the cold plate fluids
$\mathbf{T_{l,max}}$	Maximum allowable temperatures of the cold plate tanks and LLHX states
$\ddot{\mathbf{m}}_f$	Rate of mass flow rate
$\dot{m}_{pump}$	Mass flow rate in pump
λ	Penalty parameter
$\ddot{\mathbf{m}}_{f,\max}$	mass flow acceleration bound or valve rate limit

CHAPTER 1

INTRODUCTION

1.1 Motivation

Over the decades, there has been tremendous progress throughout the world to move towards more electrification of systems with the discovery of wide-band gap type semiconductor devices, compact battery storage systems, power-dense and superconducting electric machines, converters, and advanced sensing materials. These advances were made in several fields, including, but are not limited to, industrial, commercial, agricultural, and domestic applications, which are the prime benefactors of this revolution [4, 5]. Especially, the rapid pace at which the aircraft and the automobile sectors are electrifying their ground systems in order to lower the rate of fossil fuel consumption and emission of green house gases like CO_2 and NO_x is quite remarkable. The major problem with transportation depending on oils is, it cannot be sustainable over a long period of time considering the rate at which both the on-road and off-road transportation systems are being manufactured. This raises the desperate need to find a reliable, inexpensive and clean source of power to support the modern transportation systems. Some of the recent advances made in the aircraft industry are shown in Fig. 1.1.

1.2 Electrification of Mobile Transportation Systems

System-level efficiency is a key advancement needed for the aviation, marine, and automotive industries.This efficiency depends a lot on the weight, volume, and reliability of these systems. For example if we consider the automotive industry, the U.S. Environmental Protection Agency (EPA) announced new fuel efficiency standards in the year 2012 [6], which state that

Figure 1.1: Some recent concepts of hybrid electric aircrafts and universally electric aircrafts [1].

55 miles per gallon needs to be the average fuel economy of passenger cars and light weight trucks by the year 2025. In order to reach such standards quickly, the new generation vehicles need to be highly efficient to produce a significant reduction in their average fuel usage. The internal combustion engines (ICE) at present have an average efficiency of less than 25% and the ambitious goals set by government agencies cannot be achieved by the ICE technology improvement alone. Currently, switching from conventional ICE-based vehicle power-trains with the support of high-density power electronic converters, electric machines, and electric energy storage systems is an important element of an overall strategy to reach these targets of higher-efficiency and high performance. Similarly, ICE technology depends a lot on the consumption of fossil fuels, which has a direct impact on the environment. Eco-friendly global organizations are coming up with clean energy policies to be abided by several countries that restrict the usage of more fuel-based engine systems. The promising solution seems to be electrification because of it being an efficient and low-pollution energy source of transportation when compared to the tonnes of toxic gases released into the atmosphere by millions of fossil fuel powered vehicles every year around the world.

Furthermore, many subsystems in the aviation industry [7] are being converted to purely electrical systems from mechanical, pneumatic, and hydraulic domains as lighter aircrafts are more efficient and use less fuel. This new design concept is often referred to the as the More Electric Aircraft (MEA) design. An interesting example of MEA is the set of changes that

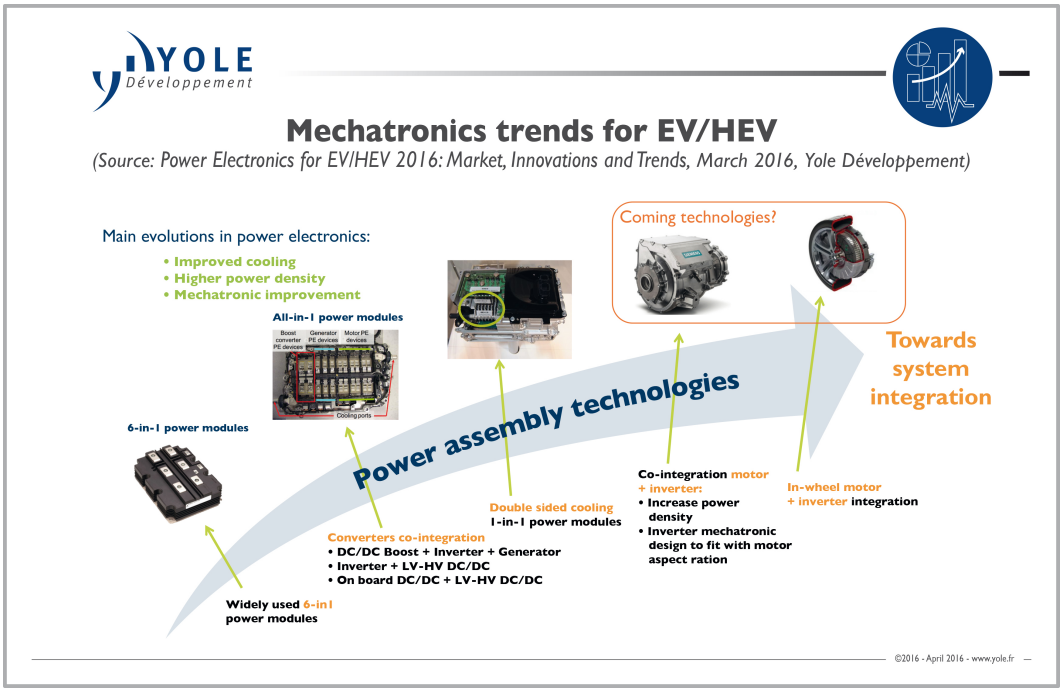

Figure 1.2: Power Assembly Technologies are moving towards System Integration in All Electric and Hybrid-electric vehicles. (Courtesy of Yole Development).

were made recently in the commercial aircrafts with the elimination of the integrated drive generator (IDG). Previously, the speed of the jet engine was controlled using IDG by mechanical means, but now the engine speed is controlled via a gearbox by changing the frequency of electric power. This greatly helped in reducing weight through the removal of now unnecessary mechanical elements in the new aircraft architecture system. A More Electric Aircraft Conference [MEAC] was held at Toulouse, France, Europe in February (2015) and the members who attended identified several advantages of a MEA type design. Firstly, MEA support redundant power options, such as electric generators and battery systems, with the help of a distributed power system. Redundant electrical power systems can involve less mass than redundant hydraulic power systems. Second, effective weight reduction is achieved by the elimination of mechanical elements, such as pumps, tanks, reservoirs and tubing. Third, most pneumatic and hydraulic equipments must be tested before installation, whereas an aircraft's Electrical Wiring Interconnection System (EWIS) can be checked during the installation process. Lastly, it is easier to integrate several other subsystems when utilizing

increasing electrification (for example, Health Utilization and Monitoring systems (HUMS)). Significant related improvements have also been made in the Airbus Boeing B787, making it the most electric commercial aircraft due to its 1.3 MW electrical power generating capacity. Interestingly, this led to the complete elimination of the pneumatic system from its architecture. Figures 1.3 and 1.4 show the difference in power distribution patterns between a conventional aircraft system that has a central power distribution architecture (Fig. 1.3) and a more electric aircraft system (Fig. 1.4), utilizing a remote power distribution network.

A significant number of developments have been made over the past 25 years, specifically in the field of mobile transportation systems toward achieving more electric aircraft (MEA), all electric ships (AESs), hybrid electric vehicles (HEVs), plug-in electric vehicles (PEVs), and battery electric vehicles (BEVs), of which a few developments in these systems have been described earlier.

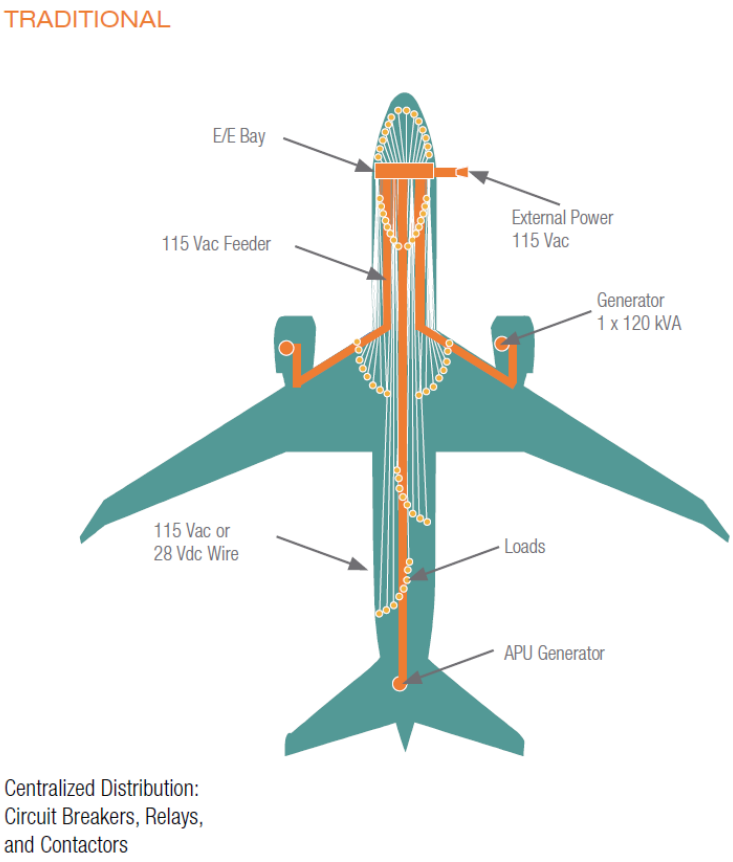

Figure 1.3: Conventional Aircraft Architecture Design with a Central Power Distribution System obtained from Ref. [2].

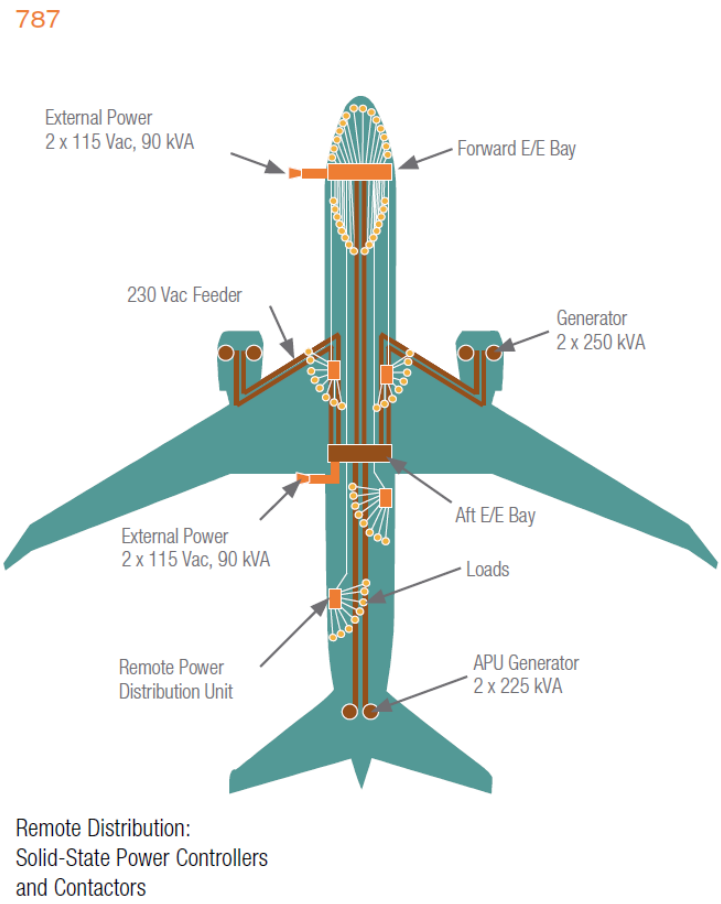

Figure 1.4: More Electric Aircraft Architecture Design with Remote Power Distribution System in Boeing B787 Commercial Aircraft obtained from Ref. [2].

1.3 Need for dynamic thermal management

The previous section clearly identifies some of the major advantages of electrifying systems on a larger scale. Although electrification has the potential to meet the needs of modern industries, it is a well-known fact that any electric system dissipates thermal energy due to conduction losses occurring in its circuits and electronic devices. As systems increase in volumetric power density, heat is dissipated within more localized regions, leading to increased temperatures. Temperature has a direct effect on the operating efficiency of any system, and also may lead to system failure. An important design challenge for dense electronic systems is to carefully manage the heat losses

in such a way that the system remains as efficient as possible and to provide system reliability. High temperature can lead to failure of sensitive components, circuit breakdown, electronic device degradation, thermal stresses in materials, and sometimes even permanent failure. All these phenomena have a direct impact on system reliability and durability.

Dynamic thermal management (DTM) systems perform thermal monitoring and apply cooling techniques to help the system operate at temperatures that maintain reliability and efficiency. In general, any DTM technique serves two purposes: 1) ability to take control action, and 2) to prevent failure. The criticality of a DTM depends on the system and the type of application. For instance, in the case of microprocessors and computer chips that have millions of transistors on them, thermal failure of a few hundred transistors may not be significantly detrimental. In other safety-critical systems, such as an aircraft or an automobile, failure of any subsystem due to heat can at best require an expensive replacement and at worst may harm passengers or others. This may bring infamy to the original equipment manufacturers (OEM) at large causing significant market losses. Other factors increase the difficulty of providing effective thermal management for dense power electronic systems, including the cost and time required to validate complex systems in realistic conditions.

Considering all the drawbacks mentioned above, the task of dynamic thermal management becomes more challenging in the case of highly power dense systems, owing to the fact that their operating powers are in the range of 100s of kilowatts (kW) to 100s of megawatts (MW). Systems operating at high power levels dissipate larger amounts of heat to their surrounding environment. Electronic design engineers now face a two-sided problem in which not only does the system needs to be lighter and more compact, but it should also be able to accommodate sensor networks and cooling circuitry for performing efficient DTM. Moreover, the current state of the art systems also need to incorporate manufacturing and packaging constraints to meet the requirements of the industries. DTM allows engineers to design systems that not only operate within safety limits, but also push the system in achieving higher levels of performance. For instance, in an aircraft there are different subsystems functioning at various time scales. Unlike microprocessors and computer circuit boards where the system is effectively functioning in steady state, aircraft and automobiles (both at system and component level) are

subject to transient loads at time scales that impact thermal performance. The DTM techniques must accomodate the transient nature of the system, providing proper control action to manage thermal losses. Sometimes cooling circuits must be designed in such a way that they account for maximum power dissipation scenarios, although they rarely occur. Sizing DTM systems for extreme events has a direct correlation with the cost and complexity of the overall system. In order to achieve effective DTM, novel system level integration and design methods must be developed to identify-optimally performing solutions.

1.4 Thesis Overview

The remainder of the thesis is organized as follows. Chapter 2 presents some of the significant efforts related to optimal sensor placement in various fields, and describes several related terms and methodologies commonly used for sensor placement. A prototype power inverter system is used in the sensor placement studies and modeling techniques for this inverter are discussed in Chapter 3. The novel and efficient algorithms for optimal sensor placement and the experimentally validated sensor placement results are also presented in Chapter 3. Chapter 4 discusses cooling system architecture design problems. Chapter 5 discusses a specific dynamic system design optimization problem for flow control in detail, followed by cooling system architecture case studies. Chapter 6 presents the conclusion and future work items.

The following overall objectives have been accomplished:

1. Developed integrated system design tools and algorithms for dynamic thermal management and fault detection. Developed new optimization methods for simultaneous control of electrical and thermal flows.

2. Investigated design-appropriate electro-thermal models to support system optimal designs or architectures.

3. Created and tested efficient new sensor placement strategies for 2D and 3D power electronic systems, and thereby expanded the complexity of sensor placement problems that can be solved efficiently.

4. Investigated critical and failure zone based sensor placement for fault diagnosis.

5. Studied optimal system level coolant flow control for multiple cooling system design architectures to support discovery of the capabilities and trade-offs associated with unprecedented system architectures.

CHAPTER 2

OPTIMAL SENSOR PLACEMENT

2.1 Motivation

This chapter explains in detail the concept of optimal sensor placement (OSP). As discussed earlier, DTM [8] is only valuable as long as accurate thermal estimation of the system is performed. Without accurate thermal monitoring, dynamic temperature control will not be effective, which in-turn defeats the purpose of DTM. Thermal monitoring is performed by using a number of temperature sensors in a system. Modern mobile systems contain complex power electronic systems for control, monitoring, user interfacing, and similar tasks, such as measurement and diagnostics, active thermal management, and electric vehicle charging. Increasing the efficiency, performance, reliability, and cost effectiveness of these mobile systems requires increased electrical system power density (both gravimetric and volumetric). Density must be enhanced while managing conflicting objectives, such as the cost, reliability, and efficiency of the electrical system. Of particular concern with dense power electronic systems (PESs) is the development of potentially high temperatures during operation. High temperature can lead to failure of sensitive components, circuit breakdown, electronic device degradation, thermal stresses in materials, and sometimes even permanent failure. All these have a direct impact on the system reliability and durability. The potential of component failure due to high temperature limits the power throughput, and therefore power density.

To perform active thermal management [8], accurate thermal monitoring [9] is essential. Critical regions where temperature-sensitive materials or components are present need to be monitored very carefully. The system-level criticality depends on the type of application; for example, breakdown or thermal burnout of a computer chip or microprocessor will not cause catas-

trophic harm in many cases, but such failures can prove to be lethal in other applications, such as aircraft. Especially in aircraft and automotive applications the hours of operation and expected lifetime are very long compared to smaller power electronic applications. Hence, accurate online estimation of the dynamic thermal profile of these systems is very important for two main reasons:

1. **Thermal management**: First and foremost, it is necessary to perform dynamic thermal management to keep the entire system well within its limiting temperatures. For example, knowing the temperature distribution via sensors and estimators can help inform how to direct coolant or throttle power throughput to maintain desirable system and component temperatures, while achieving high system performance.

2. **Fault detection**: Secondly, faults, burnouts, or degraded components can be detected early, preventing failure and supporting effective system maintenance.

Accurate thermal estimates not only help in supporting active [1] thermal management and cooling of these devices, but also help increase power density by allowing components to be pushed closer to failure (reduced safety factors) while maintaining reliable operation. The goal here is to create fail-safe, thermally-aware PESs.

High-accuracy spatial dynamic thermal system profiles could be achieved using a large number of temperature sensors that cover the entire PES. However, this is an impractical solution for most real systems as it is expensive not only in terms of sensor cost, but also fabrication, power for sensors, as well as the computational cost of monitoring the data and sensor health in real-time. In addition, sensor networks can interfere with packaging, circuit design, and system reliability. Sensors can also interfere with beneficial thermal transport that would occur in their absence, thereby affecting both thermal performance and the accuracy of parameters estimated before adding sensors. Here we explore the optimal tradeoff between accurate online estimation and the cost (and other detriments) of an increased number of sensors. Optimal sensor placement needs to be performed strategically considering the various

[1] Active in this context refers to using an external source such as a pump or a fan to control the system temperatures compared to passive methods such as a heat sink employing natural convection.

modes of system operation, overall system performance, critical locations for accurate temperature estimates, reducing the number of sensors, and other design considerations. The methods presented here are useful for non-trivial sensor placement problems where full coverage, expert intuition, or trial and error methods are not effective. Of particular interest here is improving the computational efficiency of sensor placement methods, as well as supporting the use of performance metrics more aligned with overall system utility than traditional information-based metrics.

2.2 Related work

Many researchers in the past have studied and developed strategies and algorithms for optimal sensor placement and sensor network layout design over wide ranges of applications. Any real time system requires monitoring and measurement of its parameters over time to control its operation. Several studies on optimal sensor placement were done for structural damage detection [10], especially in space structures [11], composite structures [12] and in the field of structural health monitoring (SHM) using modal assurance criterion (MAC) [13, 14], state estimation and observability [15], wireless senor networks [16],and through Fisher Information matrix [17, 18] for maximizing the information from sensors. In case of smart structures, optimal number of piezoelectric sensors and actuators were placed for maximizing various optimization criteria like observability and controllability [19], and for vibration control of plates using Linear quadratic regulator (LQR) based performance metric [20]. Sensor placement studies were also extended to the design of energy efficient buildings for monitoring temperature and indoor air quality [21] and in wind studies [22] to achieve outdoor thermal comfort and reduce energy consumption.

In addition to the above mentioned applications related to various kinds of structures, optimal sensor placement has been used for monitoring soil moisture [23] , remote sensing in precision agriculture [24,25], in monitoring wind and water quality [26],and for leak detection and fault diagnosis in water distribution networks [27–29]. In chemical process industries, concentration of the reactants and gases, temperatures in encased battery cells [30], distillation columns and reacting mixtures [31] must be measured to maintain the

specific operating conditions in order to obtain the desired products. For state estimation of different quantities like concentration and temperature, many gramian based observability criteria [32–36] have been used to place sensors optimally in tubular reactors [37], batch and reactive [31] distillation processes. Apart from passive sensor placement for health monitoring in aircraft gas turbine engines [38] , robot localization [39] and underwater vehicle localization [40], mobile sensor networks are used for studying motion co-ordination strategies and target tracking applications [41]. Sensor placement has also been studied in larger applications like thermal monitoring of hot servers in data centers [42], road transportation networks [43], over wide geographical regions in environmental and habitat monitoring [44].

Advances in power electronic systems: Several optimal sensor placement studies have been performed in thermal monitoring [45, 46] of Low Power-Density Electronics (LPDEs) like microprocessors [47–51], multi-core processors, Network-on Chip (NoC), System on chip (SoC) devices [45, 46, 52–54], data centers [55] and cyber physical systems (CPSs) [56] for dynamic thermal management [47, 48, 52, 57]. Previous work related to optimal sensor placement in power electronics was performed using conventional methods like uniform or non-uniform allocation [49], by grid-based or clustering [47, 52, 58] techniques using distance minimization and greedy approaches [51, 58], heuristics and information based estimation [50, 59, 60], for example, entropy-based [53] metrics.

Despite significant achievements, optimal sensor placement in high-density power electronic systems (HDPEs) remains a challenging task. While sensor placement has been studied extensively for microprocessors and other LPDEs, high power density electronics (HPDEs) have unique requirements. Mature placement strategies for LPDEs, such as coverage, connectivity, and heuristic-based techniques, cannot be extended readily to HPDE sensor placement decisions. Microprocessors are smaller in size than power electronics systems used for mobile transportation, power distribution and transmission, and due to system architecture it is often sufficient to focus temperature monitoring on hot spots. LPDEs often have just a single operating mode (fixed set of operating conditions), simplifying requirements. HPDEs involve multiple operating modes (switching levels), significantly higher power levels, distinct system architectures, and often higher cost. Differences also impact reliability considerations. If some of the millions of transistors on a micropro-

cessor fail, it can remain functional due to redundancy. In contrast, a HPDE device, such as a power inverter, is composed of relatively fewer function specific components. Thus, failure of just one component will not only impact functionality but overall system level performance. Some HPDEs are safety-critical devices (e.g., automotive and aircraft applications), so reliability is paramount. Enhancing the effectiveness of HPDE thermal monitoring systems for improved reliability and power density motivates the development and investigation of new design methods specific for this class of systems.

Many established sensor placement design strategies are driven by metrics that are information-based, such as observability. Information-based performance metrics are effective tools for observer design and estimation purposes, but are normally based on simplified system models to aid real-time computational efficiency. These approximate metrics cannot account for the full range of phenomena that may be important factors in assessing likelihood of thermal failure, especially for HPDEs. More sophisticated measures are needed to support off-line design decisions such as sensor placement. These should account for more detail than the reduced-order models utilized for observer implementation, including spatially-varying properties (component/switch locations, geometry, material properties, etc.).

2.3 Objectives and Contributions

One core objective of this work related to sensor placement is to demonstrate the need to accurately estimate the dynamic thermal profiles of high-density power electronic systems by utilizing a model-based estimation technique (created in previous work [3,61]) in optimal sensor placement. In addition, we present efficient sensor placement algorithms that are accurate and scalable to systems of various sizes. Finally, we validate the methods used based on controlled experiments. The primary contributions of this work are as follows:

1. To demonstrate the importance of using design-appropriate models that support the use of more accurate evaluation metrics. The lumped-parameter thermal model used in this work is shown to be well-suited for performing accurate dynamic thermal estimation.

2. Here a fundamentally new sensor placement technique is created and tested that utilizes a continuous relaxation inspired by a topology optimization method known as SIMP (Solid Isotropic Micro-structures with Penalization). This technique is compatible with very general objective functions for sensor placement.

3. Developed a new sorting algorithm for optimal sensor placement using a linear programming (LP) formulation. This strategy is orders-of-magnitude more efficient than alternative approaches, and is scalable to large-scale/fine-mesh discretized sensor placement problems.

4. Methods presented here support cases where temperature requirements vary spatially, such as in regions containing critical or sensitive components. Temperature estimation accuracy requirements can be tailored spatially to more efficiently allocate sensor locations.

5. Experimental validation of the optimal sensor placement design framework presented here using a prototype inverter.

2.4 Important terms related to sensor placement

- **Thermally-aware electrified systems** - These are power electronic systems of various types spanning from on-chip microprocessors, electromechanical devices, to power inverters and electric machines that have the sensing (via thermal estimation using sensors) and control (via software-based algorithms to maintain frequency and rating of electrical power) capabilities to maintain the system well within its desired temperature conditions. Basically from the name itself it is clear that these systems are aware of their dynamic spatial thermal profiles and take support of thermal management techniques to prevent device degradation or component failure. Not only cooling, but sometimes some devices need to be maintained at higher temperatures to make their operation more efficient. In either case, thermally-aware designs help achieve the system functionalities by overcoming temperature-related hindrances. It is sometimes referred to as temperature-aware design.

- **Sensors and actuators** - Sensors are devices that help detect or measure parameters of a physical environment based on some input. Good sensors do not interfere with the measured property, and their sensitivity relies the a lot on how accurately they can detect a change in output to the input parameters. Some examples are temperature sensors, pressure sensors, current sensors and so on. Actuators are devices or components that are responsible for moving, oscillating, rotating or controlling a system mechanism. They act on a control signal and perform a mechanical or other physical action. Actuators use a source of energy that could be hydraulic, electrical, or pneumatic in nature. Example include fluid valves, piezoelectric devices, etc.

- **Optimal sensor placement** - It refers to embedding or placing a minimum numbers of sensors at ideal locations on a system, subsystem, or a component to provide real-time information of various physical parameters. Some well-known physical parameters of a system include temperature, pressure, thermo-mechanical stress, heat flux, current, and so on. Optimal sensor placement is used as a tool to better monitor the physical health of a system, or to retrieve accurate information for control purposes.

- **Wireless sensor network (WSN)** - A wireless sensor network refers to a collection of sensors that are spatially dispersed for the purpose of measuring or detecting physical conditions such as temperature, humidity, chemical substances, pressure, structural health monitoring, and so on in a certain environment. Each sensor is represented by a node, while the network represents a graph, and sometimes these networks can be layered. Many modern networks are bi-directional, which means they can used both for sensing and control purposes. WSNs can have different network topologies based on their specific applications, and the information hopping across the network is done either using routing or flooding techniques. Routing refers to choosing a specific path while flooding refers to spreading the information to every part of the network. Figure 2.1 shows a typical wireless sensor network. A gateway sensor node refers to the router from where the information is exchanged back and forth between the sensor network and data collection point.

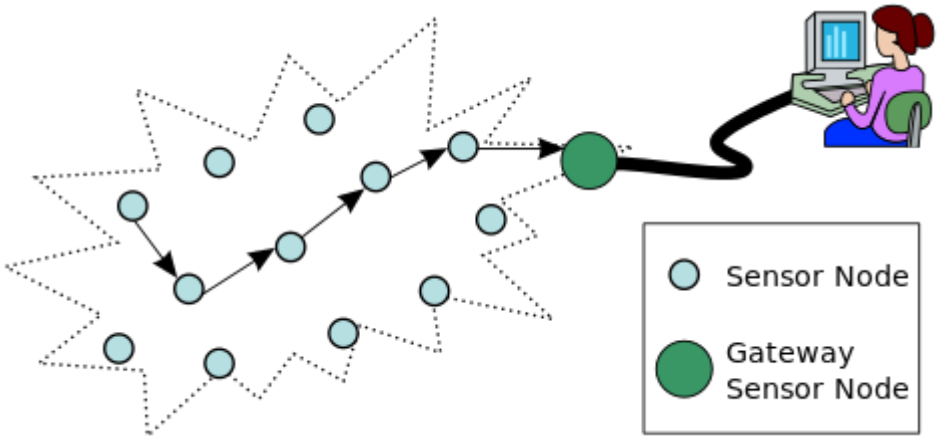

Figure 2.1: A wireless sensor network architecture. [Source-Wikipedia]

2.5 Performance metrics commonly used in OSP

This section describes some of the most commonly-used performance metrics for optimal sensor placement. Sensor networks are widely used in different applications ranging from structures to medical devices, electronic systems to water networks, quality monitoring to robot localization, and so on. Although the principle is to extract maximum information from the system in order to monitor its physical condition, the way is it done depends a lot on the kind of models that are used to represent these systems. For example, structural systems are represented using finite element models, highly dynamic systems, such as electronic circuits, are represented using lumped-parameter graph-based models, geometric coverage/layout problems use distance-based models, and water networks can be represented using computational fluid dynamic models. Several performance metrics, sometimes called objective functions, are used to capture the physical information (such as temperature, pressure, humidity, etc.) pertaining to a particular system. The two most prominent performance measures for OSP in structural systems are described below:

- **Modal Assurance Criterion (MAC):** This metric is very commonly used in Structural Health Monitoring (SHM) and damage detection in building and bridge design [62]. Modal shapes having the highest numbers of degrees of freedom (DOFs) are chosen as the modes where the sensor needs to be located. The MAC has been applied successfully as an objective function to measure the utility of a sensor configuration

in OSP. The MAC is defined to measure the correlation between two mode shapes (e.g., obtained from different sources). Each component of the MAC matrix is written as follows, taking into account the possible sensor locations:

$$MAC_{ij}(\boldsymbol{\vartheta}) = \frac{[\boldsymbol{\phi}_i^T(\boldsymbol{\vartheta})\boldsymbol{\phi}_j^T(\boldsymbol{\vartheta})]^2}{[\boldsymbol{\phi}_i^T(\boldsymbol{\vartheta})\boldsymbol{\phi}_i(\vartheta)][\boldsymbol{\phi}_j^T(\boldsymbol{\vartheta})\boldsymbol{\phi}_j(\boldsymbol{\vartheta})]}, \tag{2.1}$$

where $\boldsymbol{\phi}$ is the mode shape matrix, and the subscripts i and j denote the i^{th} and the j^{th} columns of $\boldsymbol{\phi}$, which are indicator of the orders of the selected modes. The selected mode shapes are functions of the sensor location parameter $\boldsymbol{\vartheta}$. In regard to OSP, the goal is to obtain a sensor layout that gives the minimum off-diagonal values of the MAC matrix so that the mode shapes become easily distinguishable. We herein study two objective functions defined by the off-diagonal elements of the MAC matrix. The first objective function is the largest off-diagonal element, given by:

$$f_1(\boldsymbol{\vartheta}) = \max_{i \neq j}[MAC_{ij}(\boldsymbol{\vartheta})]_{i,j=1,2,\ldots,p}, \tag{2.2}$$

where p is the total number of selected modes for OSP. The second objective function or performanc metric is defined as the sum of the off-diagonal element least squares, that is given by:

$$f_2(\boldsymbol{\vartheta}) = \sum_{i=1,j=1,i\neq j}^{p} [MAC_{ij}(\boldsymbol{\vartheta})]^2. \tag{2.3}$$

An OSP configuration is obtained if the minimum of the objective function is found.

- **Effective Independence Technique (EFI):** The EFI method discussed in [63], developed by Kammer [64], is one of the most popular methods to optimally locate sensors in structural dynamic tests. The starting point of the EFI method is the full modal matrix from a finite-element model of the structure to be studied. The finite element model could be built with any type of elements, but not all DOFs under consideration can be measured. Some of these DOFs are internal, while others are rotations, neither of which can be measured conveniently in

some applications. Hence, the rows corresponding to DOFs that cannot be measured are deleted from the full modal matrix. Furthermore, system identification methodologies from sensor data records can only extract some of the mode shapes of the structure under study. Therefore, a limited number of target modes must be selected to find the best sensor configuration. Consequently, only some rows (potential DOF locations) and columns (target modes) of the full modal matrix are retained. The EFI sensor placement algorithm is based on the FIM (Fisher Information Matrix) F, which is defined as:

$$\boldsymbol{F} = \boldsymbol{\phi}^{\boldsymbol{T}}\boldsymbol{\phi}, \tag{2.4}$$

where $\boldsymbol{\phi}$ is the mode shape matrix. The FIM is symmetric and positive semidefinite. Furthermore, if the mode shape vectors are linearly independent, then the FIM is full rank; i.e., the rank is equal to the number of target mode shapes. The main aim of the EFI method is to select the best DOF configuration (in which sensors are to be placed) that maximizes the FIM determinant. These DOFs are selected in an iterative way, thereby producing a sub-optimal solution to the problem. The selection procedure is based on the orthogonal projection matrix $\boldsymbol{E}$, defined as:

$$\boldsymbol{E} = \boldsymbol{\phi}\boldsymbol{F}^{-\mathbf{1}}\boldsymbol{\phi}^{\boldsymbol{T}}, \tag{2.5}$$

The matrix $\boldsymbol{E}$ is an idempotent matrix with rank equal to the sum of the diagonal terms. Hence, the i^{th} diagonal element of matrix $\boldsymbol{E}$, denoted by E_{ii}, represents the fractional contribution of the i^{th} DOF to the rank of $\boldsymbol{E}$. The DOF with the lowest value of E_{ii} is deleted as a candidate sensor location, and the corresponding row is removed from the modal matrix. The contribution of E_{ii} to the rank of $\boldsymbol{E}$ is often cited as the reason that this procedure retains the linear independence of the mode shapes. However, it is easily shown that :

$$\det(\boldsymbol{F}) = \det(\boldsymbol{F_0})(1 - E_{ii}). \tag{2.6}$$

where $\boldsymbol{F_0}$ is the original FIM and $\boldsymbol{F}$ is the FIM after the removal of the

i^{th} sensor. Thus, every time one row is deleted from the mode shape matrix $\boldsymbol{\phi}$, the determinant of the FIM decreases, and the objective of the selection method is to maintain a high value for this determinant. It is often highlighted that the high determinant ensures the variance of the estimated response is low, and this is used as the criteria for sensor location selection.

Although several such performance metrics exist depending on the type of application, almost all of them are similar to or slight variants of the ones that are listed above in terms of their principles. In case of systems whose dynamic state space models can be obtained, controllability- and observability-based information metrics are used to determine the optimal sensor locations in systems. More details about these metrics are discussed in detail in Section 3.3.1 presented in the next chapter.

CHAPTER 3

OSP CASE STUDY: POWER ELECTRONIC SYSTEM

3.1 Flying Capacitor Multi-Level Inverter System

This section details the multi-level power inverter system that serves as the case study for the optimal sensor placement studies presented in this thesis. The inverter is a 2 kilowatt, 60 Hertz, single-phase, 450-V_{DC} to 240-V_{AC} power inverter printed circuit board (PCB). It is shown in Fig. 3.1 with its various components labeled, and Fig. 3.2 shows the structure and thickness of the various layers it is composed of. It has a planar architecture with active switching components on the top, with the overall dimensions of 64.7 mm by 47.3 mm. The inverter has twelve low-voltage GaN (Gallium Nitride) switches operating at 120 kHz, and features a seven-level Flying Capacitor Multi-level Converter (FCML) [65]. It achieves a high power density of 216 W/in^3 with a peak overall efficiency of 97.6 percent. The GaN transistors are the most significant heat-generating components on the board. Each of these PCBs can be stacked together to form a larger power generating source with a capacity of few 10s or 100s of kilowatts for various applications. The Adum 5210 devices are isolated level shifters that power the gate drivers. The ceramic capacitors reduce the stress on switching devices and help transfer electrical energy. As power levels increase, the temperature of the GaN transistors increases, while the temperature of the Adum 5210 devices remain approximately constant due to constant control losses. The PCB is a layered board that consists of four copper layers, three layers of glass reinforced epoxy laminate (FR4) and two solder mask layers. The material properties related to the PCB are shown in Table 3.1.

Figure 3.3 shows the 3D inverter system that contains both the PCB and the heat sink on its top. The heat sink is made up of aluminum (-highly conductive: K_{Al} 205 W/mK), with a base 8 cm long by 3 cm wide. Each

Table 3.1: PCB constituent material properties.

Material Used	Specific (Heat J/gC)	Thermal Conductivity (W/mK)	Density (g/cm^3)
Copper	0.385 to 0.4	385 to 390	8.9 to 8.96
FR4	0.6 to 0.95	0.25 to 0.3	1.85 to 1.91

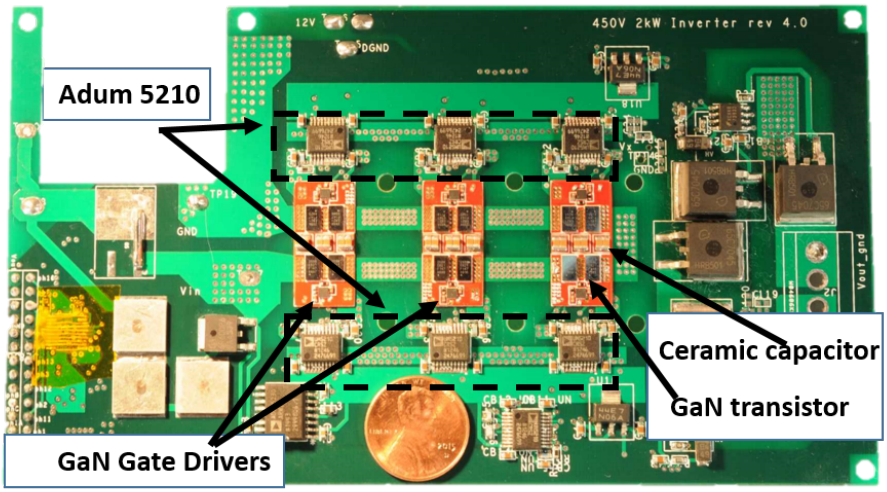

Figure 3.1: A 2 KW, DC-AC, single-phase, 7-level flying capacitor multilevel inverter- 2D system

of the rectangular heat sink fins is 2.5 cm high by 0.8 cm in thickness. A 0.051 cm fiberglass-reinforced polymer thermal gap pad and filler (Gap Pad 5000S35) with a relatively high thermal conductivity is placed on top of the active components. It acts as a filler between the aluminum heat sink and the active components on the PCB. It efficiently conducts heat from the active components to the the heat sink in z direction. From a thermal perspective, the gap pad increases the thermal performance of the inverter, and from an electrical perspective, it enhances electric insulation between the components and heat sink.

3.2 Power Inverter System Modeling

To perform accurate dynamic spatial thermal estimation, we require a model that can help extract information from the power electronic system. A very

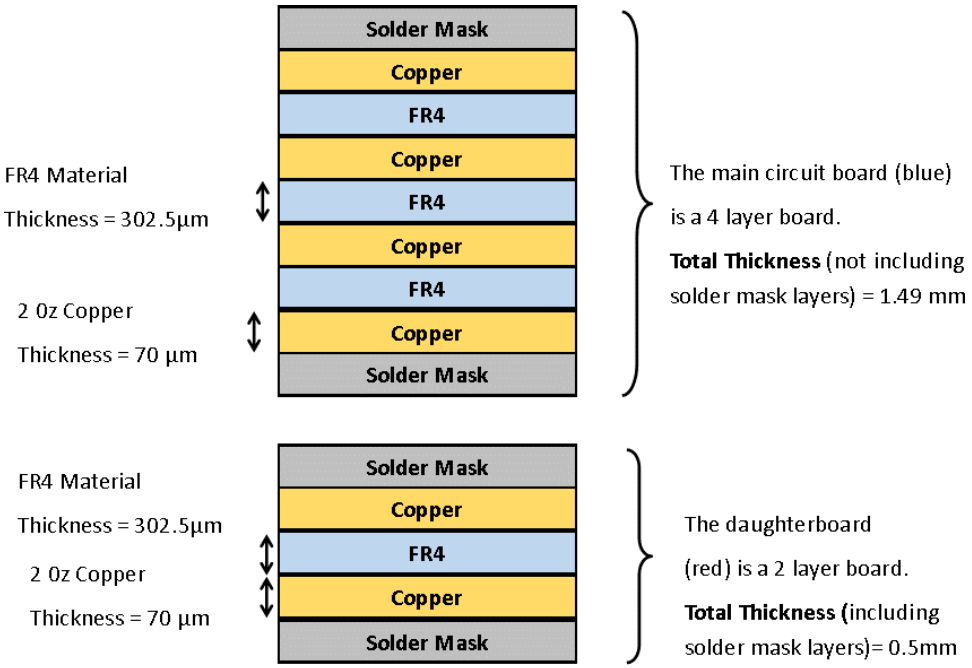

Figure 3.2: Structural depiction of the power inverter board with different layers along with their thicknesses.

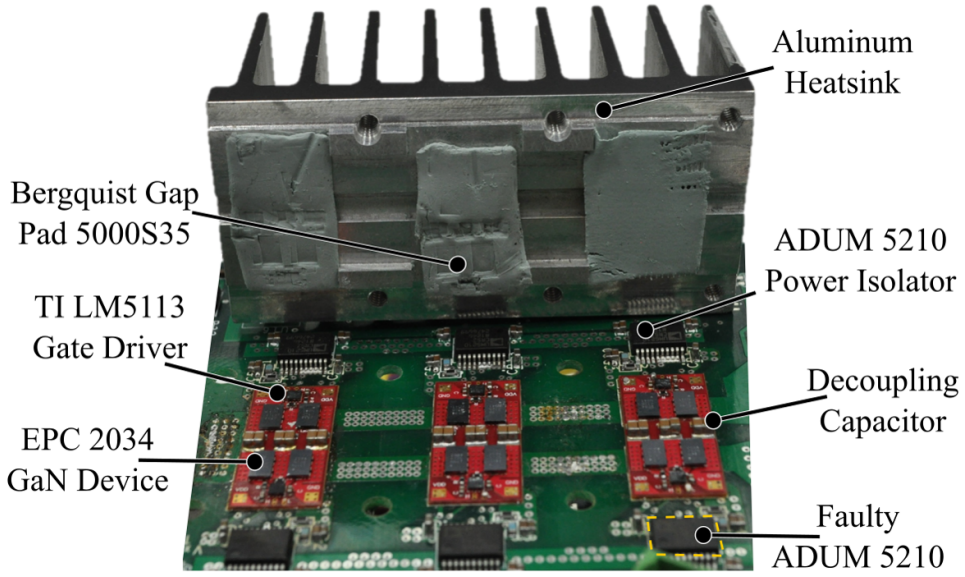

Figure 3.3: PCB with Aluminum heat sink - 3D system

important aspect in modeling a system for design is having the flexibility of evaluating its performance while changing the design variables. Design-specific modeling is very useful for optimizing various parameters of the system. Here we present design-appropriate models for designing thermally-

aware power electronic systems. Here a lumped-parameter resistor-capacitor (RC) graph-based modeling technique has been implemented, considering the duality between thermal and electrical domains based on previous work [61]. On-line estimation becomes more challenging with a higher dimensional thermal model. Therefore, a trade-off exists between the accuracy of thermal estimation and model complexity. A model order reduction (MOR) technique has been used to preserve both the physical information, while simultaneously making the estimation process easier. This is achieved by reducing the number of parameters to be evaluated. Commonly used model order reduction techniques include Hankel-norm Reduction [66] and Proper Orthogonal Decomposition [67]. A MOR technique decreases the size of a high-dimensional graph model by aggregating several nodes into a single super-node to create a reduced-order model. Each super-node contains both the physical and thermal information of its corresponding nodes in the full-order model.

3.2.1 2-dimensional RC Thermal Model

The multilevel power inverter system shown in Fig. 3.1 is open to the ambient environment, i.e., it is not enclosed with a heat sink. Therefore, convective heat transfers occurs in the z-direction while there is conductive heat transfer in both the x and y directions along the inverter. A resistor-capacitor (RC) network was used to model the dynamic thermal behavior of the power electronics system for estimation purposes. This model sacrifices some predictive accuracy to support rapid computation. High-fidelity thermal models would be impractical for real-time estimation, but are important for off-line design and for assessing the quality of real-time temperature estimates.

The RC network is created using an analogy between electrical and thermal systems, where electrical current is analogous to heat flux (both are 'through' or 'flow' variables), and voltage is analogous to temperature (both are 'across' or 'effort' variables) [54, 68]. Electrical resistance and capacitance properties are used to model thermal capacitance and resistance. The thermal model of the multi-level inverter was generated as a 2D RC model. The PCB was divided into planar regions, each associated with a capacitance value. Adjacent regions are connected by resistance elements, enabling heat conduction across region interfaces. Heat generation is modeled as a current

source. Ambient temperature is modeled as a voltage source connected to each capacitor through a resistor that represents convective heat transfer. Thermal capacitance is given by:

$$C = \rho c V, \tag{3.1}$$

where ρ is material density, c is specific heat capacity, and V is the region volume. Thermal conduction resistance is modeled as:

$$R_{\mathbf{cond}} = \frac{L}{K A_c}, \tag{3.2}$$

where L is the length through which the heat is being conducted, K is the thermal conductivity of the material, and A_c is the cross-sectional area of the conductive material. Convective resistance is given by:

$$R_{\mathbf{conv}} = \frac{1}{h A_s}, \tag{3.3}$$

where h is the heat transfer coefficient and A_s is the region area as shown in Fig. 3.4.

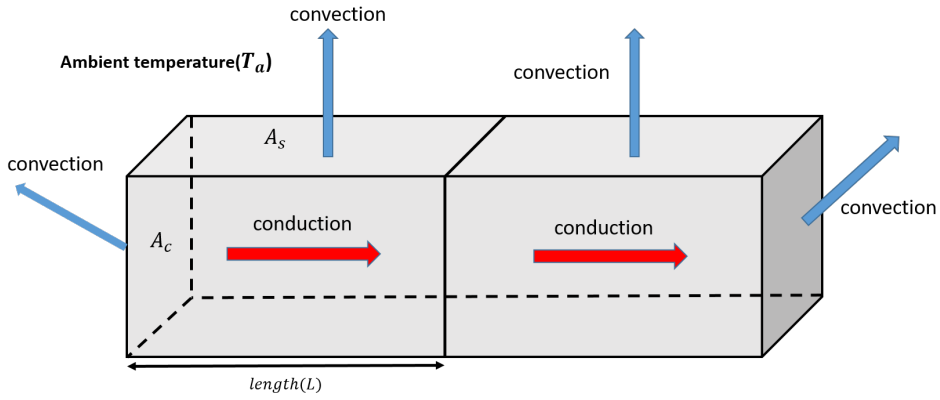

Figure 3.4: Heat transfer mechanisms in a sample discretized two-region system.

A state space model was constructed using the graph-based modeling approach, where each graph node represents an RC model node, and each edge represents resistance between vertices. Conservation of thermal energy is

applied at each vertex to complete the model:

$$C_k \frac{dT_k}{dt} = q_k + Q_s - \frac{1}{R_{ck}}(T_k - T_a), \tag{3.4}$$

where C_k is the thermal capacitance at node k, T_k is the temperature of node k, q_i is the net heat flow into node k, and Q_s is the heat input from the current source connected to node k. The convective heat transfer resistance at node k is R_{ci}, and the ambient temperature is T_a.

The inverter is partitioned into 39 planar regions, each with a functional board component, and each corresponding to a state in the state space model. The switches on the PCB are the primary heat sources. The RC inverter model has been validated experimentally in an earlier study [61]. MOR was performed to produce a nine-state model that preserves correspondence between the physical system and the RC thermal model (Fig. 3.5). The corresponding first order differential equations are:

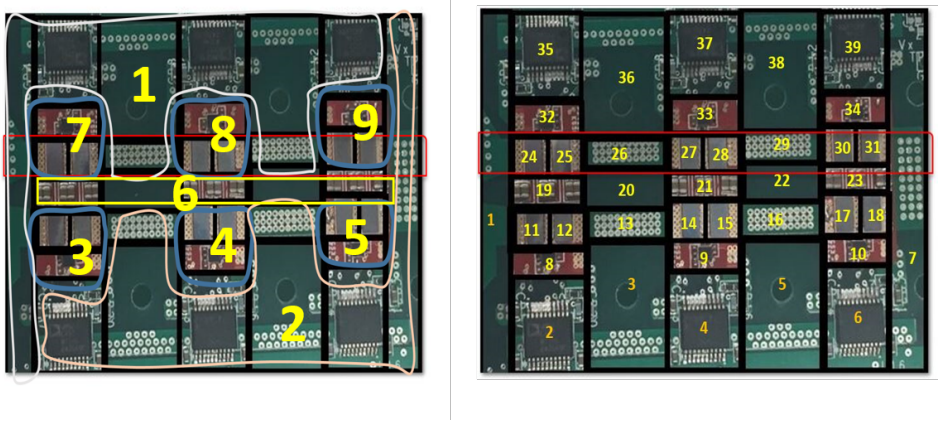

Figure 3.5: Reduced order (9 states) and full-order (39 states) thermal 2D models.

$$\dot{\mathbf{x}} = A\mathbf{x} + B\mathbf{u} + V\mathbf{d} \tag{3.5}$$

$$\mathbf{y} = C\mathbf{x} + D\mathbf{u} + W\mathbf{e} \tag{3.6}$$

The state vector $\mathbf{x}$ (dimension $n \times 1$) represents the temperature of each node on the graph. The number of states is n, and A and C (both with dimension $n \times n$) are the system dynamics and output matrices, respectively.

Table 3.2: Mapping between full-order model states and reduced-order thermal model states.

Reduced-order model state index	**Full-order model state indices**
1	1, 26, 29, 35, 36, 37, 38, 39
2	2, 3, 4, 5, 6, 7, 13, 16
3	8, 11, 12
4	4, 14, 15
5	10, 17, 18
6	19, 20, 21, 22, 23
7	24, 25, 32
8	27, 28, 33
9	30, 31, 34

The input vector $\mathbf{u}$ (dimension $c \times 1$) represents the time-varying heat flux from the c heat generating components. B (dimension $n \times c$) is the input matrix, $\mathbf{d}$ is the state disturbance vector (used to model the ambient temperature, which is assumed to be a constant 30° C), and V is the disturbance matrix. The output trajectories $\mathbf{y}$ are the observed node temperatures. W and $\mathbf{e}$ model sensor noise. Table 3.2 illustrates the mapping from the full-order model states to the reduced-order thermal model states. The predicted state temperatures for the reduced order model and the full order model were validated and shown to be accurate in previous work [61].

3.2.2 Three-dimensional RC thermal model

A model for a planar (two-dimensional) system was just presented. When combining the inverter with a heat sink, the planar model is inadequate. As depicted in Fig. 1.3, heat is conducted in all the three directions (x, y, and z). Due to the heat sink, convective heat transfer is absent between the ambient atmosphere and inverter components. It is assumed that the convective heat transfer from the bottom side of the inverter to the ambient air is negligible because heat-generating components are on top of the PCB, and several layers of material below separate these components from the environment.

The 3D model development is similar to the 2D modeling procedure. While the 2D thermal system was discretized into planar regions, the 3D thermal system is discretized into voxels. Each voxel represents a functional compo-

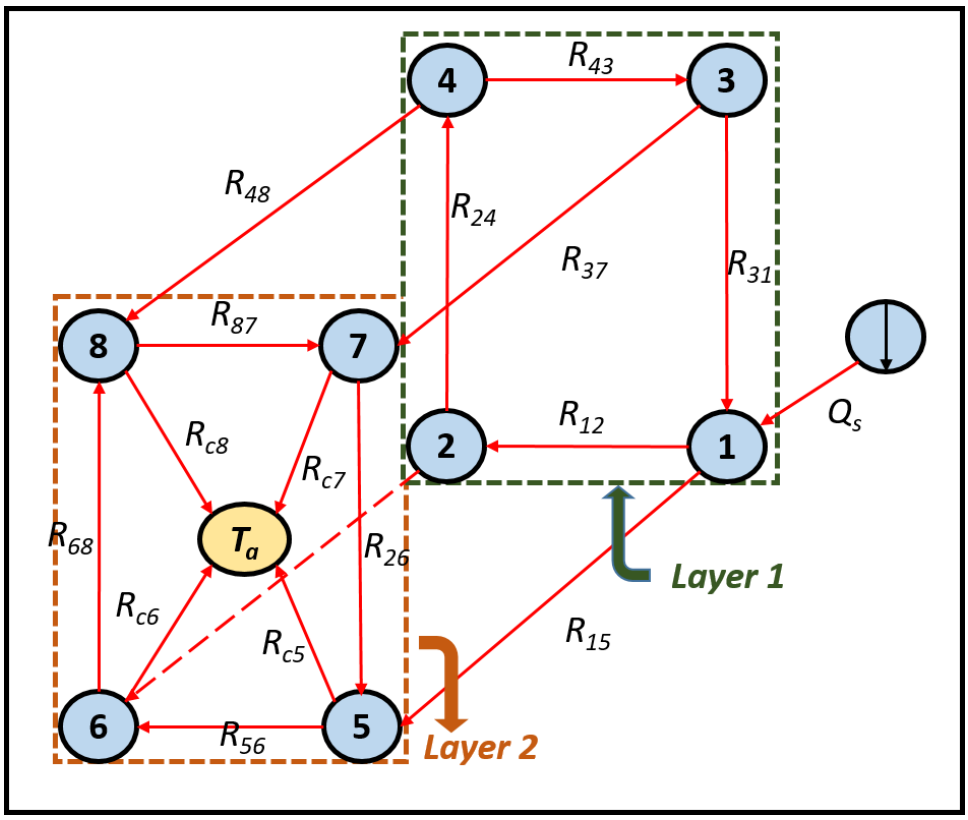

Figure 3.6: 3D thermal network representation.

nent of the 3D system having a capacitance value. Adjacent voxels that are not exposed to the ambient environment are assumed to have heat transfer via conduction alone. However, voxels (if any) that are exposed to the ambient atmosphere include an additional convective resistance edge. Along the x, y and z directions, the conductive resistances are calculated using Eqn. (3.2), whereas the convective resistances cannot be calculated directly using Eqn. (3.3). Instead, the following relationship is used to account also for extended resistances:

$$R_{t,o} = \frac{1}{\eta_o h A_t}, \tag{3.7}$$

where $R_{t,o}$ and η_o are the overall effective convection resistance and the overall efficiency of the array of fins, respectively, A_t is the total surface area (including the extended surface area due to the heat sink), and h is the convection heat transfer coefficient. The fin array overall efficiency η_o is given by:

$$\eta_o = 1 - \frac{N A_f}{A_t}(1 - \eta_f), \tag{3.8}$$

where N, A_f and η_f are the number of fins, surface area of a fin, and the efficiency of a single fin, respectively. The number of fins N is calculated using the formula:

$$A_t = NA_f + A_b, \tag{3.9}$$

where A_b is the exposed base area of the extended surface. The efficiency of a single fin η_f is given by:

$$\eta_f = \frac{\tanh mL_c}{mL_c}, \tag{3.10}$$

where L_c (the corrected length) and the model parameter m are found using:

$$L_c = L + t/2, \tag{3.11}$$

and

$$m = \sqrt{\frac{2h}{kt}}. \tag{3.12}$$

This equation is based on the assumption that rectangular fin width is greater than its thickness. L and t are the length and thickness of the fin, respectively. The dynamics of the 3D PES are obtained using coupled first order differential equations:

$$C_i \frac{dT_i}{dt} = q_i, \tag{3.13}$$

where C_i, T_i, and q_i denote the capacitance, temperature, and the net heat flow at node i of the thermal network (similar to the 2D model differential equations). The 3D thermal model thus contains two layers as shown in Fig. 3.6: the 2D power inverter thermal layer and the heat sink thermal layer that is exposed to the ambient atmosphere. In Fig. 3.6 the PCB is layer 1, and the heat sink is layer 2. Each layer has four nodes. The heat sink nodes are connected to an infinite-capacitance ambient temperature node T_a. Q_s is the input source node. The 3D thermal model was discretized into 78 nodes (39 nodes representing the PCB and the remaining 39 nodes representing the heat sink). MOR techniques were applied to the full-order RC model to produce a reduced order RC model, alleviating the computational expense of estimation. The reduced-order 3D thermal model is represented using 10 nodes (9 nodes for the PCB and a single node for the heat sink). The 3D model used here has been validated experimentally, as reported in Ref. [3].

3.3 Optimal Sensor Placement Strategies

The aim of the methods presented here is to quantify the optimal tradeoff between the number of sensors required and accurate dynamic thermal estimation. In this section, alternative sensor placement strategies are discussed, including methods based on integer programming, continuous relaxation, and strategies combining quantitative tools and intuition.

3.3.1 Information-Based Performance Metrics

A system is observable if its state variables can be reconstructed from available outputs. The RC model is linear and time invariant (LTI), so we can use the linear observability Gramian to quantify observability:

$$W_{o,\text{linear}} = \int_0^\infty e^{A^T t} C^T C e^{At} dt, \tag{3.14}$$

A system is completely observable only when the observability Gramian matrix has full rank. Additional related measures of system observability have been used in optimal sensor placement studies. The three most widely-used metrics are summarized here [37, 69, 70].

Observability Gramian Determinant:

Larger observability Gramian determinants are associated with improved system observability. If $\det(W_{o,\text{linear}}) = 0$, all states cannot be observed. The metric commonly used is: $D = [\det(W_{o,\text{linear}})]^{1/n}$, where n is the number of system states. This metric is less preferred than the next two because if the determinant is zero, it is difficult to determine the states actually contributing to system observability.

Observability Gramian Condition Number:

The condition number of a matrix refers to the ratio of its largest and smallest magnitude eigenvalues. Smaller observability Gramian condition numbers

correspond to improved observability. Often logarithmic scaling is used:

$$C = \log_{10}\left[\frac{\sigma_{\max}(W_{o,\text{linear}})}{\sigma_{\min}(W_{o,\text{linear}})}\right]. \tag{3.15}$$

This metric has been used widely in chemical engineering processes [71].

Observability Gramian Trace:

The observability Gramian trace refers to the sum of all Gramian eigenvalues:

$$\text{Trace}(W_{o,\text{linear}}) = \sum_{i=1}^{n} \sigma_i(W_{o,\text{linear}}). \tag{3.16}$$

Measures based on Gramian condition number and determinant are limited in their ability to obtain information from the whole range of system states. The trace metric does not have this limitation. Maximizing it supports maximum information extraction [35]. It can be thought of as the output observability energy of a system. The larger this value is, the greater the system observability. In studies presented here where only one information-based performance metric is used, the trace metric is chosen.

3.3.2 Enumeration-Based Placement Solution

One way to view the placement problem is as a discrete decision. If we have n_s sensors, in which PCB regions should they be placed to maximize estimation accuracy? In this approach, we do not distinguish between continuous location differences within a PCB region, only if a sensor is in a region or not. A sure method for obtaining a globally-optimal solution for this discrete sensor placement problem is to enumerate all possible unique placements, evaluate each design using the chosen metric, and select the design(s) with the best performance. This strategy is possible for small test problems, but completely impractical for realistic problems (especially if we use a fine spatial discretization for improved placement resolution).

If our model has n states, and we assume that each region can have either zero or one sensor, and if we consider the full range of the possible numbers of sensors ($0 \leq n_s \leq n$), the number of possible sensor placement designs for our 39 and 9 state models are 2^{39} and 2^9, respectively. An enumeration of all

sensor location designs has been performed for the reduced-order (nine-state) model, and assessed using all three information-based performance metrics: determinant, condition number, and the trace of the observability Gramian matrix. The enumeration results are illustrated in Fig. 3.7. For each number of sensors, a spread in performance is observed. As an example, the number of unique sensor placements possible with four sensors on a nine-region PCB is $\binom{9}{4} = 9!/(4!(9-4)!) = 126$. Enumeration results helps us to understand the trends in the performance metrics, and may be used as a benchmark for comparing the other placement methods (at least for the low-dimension nine-region case).

3.3.3 Discrete Optimization

Here we formulate the placement problem as a binary integer programming problem. A binary variable r_i exists for each state/region. If $r_i = 1$, a sensor is placed in region i, and if $r_i = 0$, region i has no sensor. If we want to place exactly k sensors, we require that $\sum_{i=1}^{n} r_i = k$. This problem may be solved with integer programming methods. A genetic algorithm can be used to solve very general formulations of this problem approximately. This integer programming strategy has proven to be inefficient for large-scale problems [72, 73], motivating new solution techniques presented later in this section. The observability matrix Q_o (of order np x n, where p is the length of the output y):

$$Q_o = \begin{bmatrix} C & CA & CA^2 \dots CA^{n-1} \end{bmatrix}^T \tag{3.17}$$

must be full rank for the system to be completely observable. The diagonal output matrix C (size $n \times n$) is:

$$C = \begin{bmatrix} r_1 & 0 & 0 & \dots & 0 \\ 0 & r_2 & 0 & \dots & 0 \\ \vdots & \vdots & \vdots & \ddots & \vdots \\ 0 & 0 & 0 & \dots & r_n \end{bmatrix}.$$

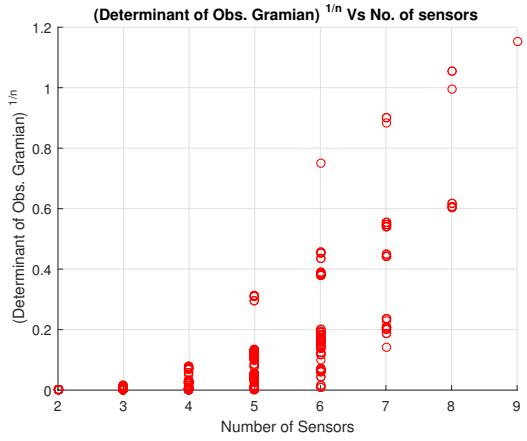

(a) Determinant of $W_{o,\text{linear}}$

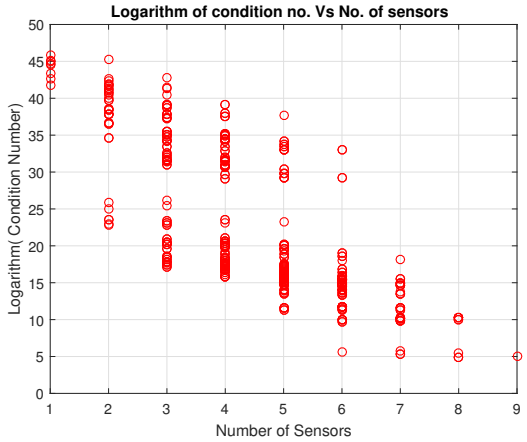

(b) Condition number of $W_{o,\text{linear}}$

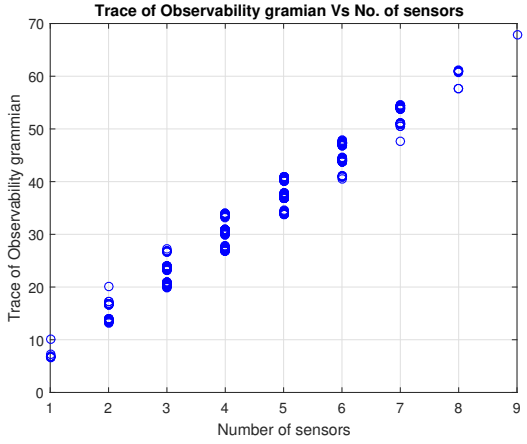

(c) Trace of of $W_{o,\text{linear}}$

Figure 3.7: Enumeration of all possible discrete sensor placement solutions for the nine-state reduced-order model. All three information-based performance metrics are illustrated.

Using the trace metric defined above, we can formulate the sensor placement problem as the following binary integer program:

$$\begin{aligned} \underset{\mathbf{r}}{\text{minimize:}} \quad & \text{-tr}(W_{o,\text{linear}}) \\ & = -\text{tr}\left(\int_{t_0}^{t_1} e^{A^T(t-t_0)} C^T C e^{A(t-t_0)} dt\right) \\ \text{subject to:} \quad & \sum_{i=1}^{n} r_i \leq k \\ & r_i \in \{0,1\} \end{aligned} \tag{3.18}$$

The number of sensors k is varied parametrically. Note that due to monotonicity, the inequality constraint on r_i values is always active, and this inequality constraint is therefore satisfied with equality. This formulation is mathematically equivalent to one requiring an exact number of sensors k. The inequality constraint is used instead of the equality constraint to improve computational solution efficiency.

3.3.4 Continuous Relaxation

In the discrete optimization approach, solution difficulty increases rapidly as system size (n) increases. As with enumeration, it is impractical for scaling up to larger system design problems. Here we present a novel sensor placement strategy based on a continuous relaxation of the binary variables. Such a relaxation enables the use of highly-efficient gradient-based optimization algorithms [74]. Here we allow r_i to take on any value between 0 and 1. Because a fractional sensor does not make physical sense, we can use a creative formulation to bias r_i values toward 0 or 1. While fractional values are allowed, at convergence each r_i is approximately binary.

This solution strategy is analogous to established methods for structural topology optimization where a structural design domain is discretized into pixels (2D) or voxels (3D). Continuous design variable $0 \leq x_i \leq 1$ represents material density for each element. One of the most well-known gradient-based topology optimization methods is the Solid Isotropic Material with Penalization (SIMP) approach [75]. SIMP utilizes a particular type of penalty on x_i values to bias them toward $\{0,1\}$ values. Our continuous relaxation of the sensor placement problem, inspired by SIMP, is:

$$\begin{aligned} \underset{\mathbf{r}}{\text{minimize:}} \quad & f(r_1^p, r_2^p, ..., r_n^p) \\ \text{subject to:} \quad & \sum_{i=1}^{n} r_i \leq k \\ & 0 \leq r_i \leq 1. \end{aligned} \tag{3.19}$$

A finite penalty exponent value p (generally chosen between 2 and 9) can result in a solution that coincides approximately with the discrete solution. Larger penalty values improve binary precision, but this also increases nonlinearity and solution difficulty. This can be ameliorated through a change of variables. Define t_i such that $t_i = r_i^p$, and $r_i = t_i^{1/p}$. A mathematically equivalent problem can be defined in terms of t_i:

$$\begin{aligned} \underset{\mathbf{t}}{\text{minimize:}} \quad & f(t_1, t_2, ..., t_n) \\ \text{subject to:} \quad & \sum_{i=1}^{n} t_i^{1/p} \leq k \\ & 0 \leq t_i \leq 1. \end{aligned} \tag{3.20}$$

Due to the change of variables, this problem can be solved more easily for large p values.

3.3.5 Linear Integer Program Reformulation

The continuous relaxation strategy reduces computational expense significantly, and supports use of more general performance metrics beyond observability metrics that are information-based. We observed, however, an important opportunity for even greater efficiency improvements when using one particular performance metric. It is possible to manipulate the trace of the observability Gramian in a way that enables formulation as a linear program (LP), a convex optimization problem that can be solved efficiently for very large systems (thousands of states or more). Instead taking the integral over time from t_0 to t_1, the trace of the observability Gramian derivative $fd(\mathbf{r})$, which is a linear function, can be calculated using a finite difference method. The gradient can then be used directly in the solution of the corresponding LP. The procedure for obtaining the trace of observability Gramian

derivative is detailed in Algorithm 1. The LP is:

$$\underset{\mathbf{r}}{\text{minimize:}} \quad -fd(\mathbf{r}) \tag{3.21a}$$

$$\text{subject to:} \quad \sum_{i=1}^{n_s}(r_i) \leq n_s \tag{3.21b}$$

$$r_i \in \{0,1\} \tag{3.21c}$$

ALGORITHM 1: Calculation of derivative of trace of observability gramian matrix

Input : *A,B* – system dynamics matrix(A) and input matrix(B) *h* – step-size for forward differencing

Output: **fd** – derivative of trace Observability Gramian

```
1 ns ← length(A)                                   /* store total number of states */
2 fd ← zero                                        /* Initialize Observability derivative */
3 C ← zeros(ns, ns)                                /* Initialize an output matrix */
4 ss ← ss(A, B, C, [])                             /* Calculate state space form */
5 for k ← ns do                                    /* going from 1 to entire length of A */
6 |   fd1(k) ← trace(ObsGram(ss(t0))                /* calculating the trace of obs. Gram. Wo
  |     at instant to */
7 |   fd2(k) ← trace(ObsGram(ss(t0 + h))           /* calculating the trace of obs. Gram.
  |     Wo at instant t0 + h */
8 end
9 fd ← (fd2 - fd1)/h                               /* forward difference method */
```

3.3.6 Critical Zone-Based Sensor Placement

In this strategy we modify our optimization formulation to ensure a specified number of sensors are used to monitor regions near critical locations. This can help bias placement near critical states (components). It can be thought of as a hybrid between intuition and information-based design. It is informed by designer specifications for critical locations. Suppose the designer specifies j specific states as critical locations: $\{S_1, S_2, \ldots, S_j\}$, and the designer wants to allocate a minimum of k sensors from the m total available sensors to monitor these critical states. The rest may be placed elsewhere. The new

formulation is:

$$\begin{aligned}
\underset{r}{\text{minimize:}} \quad & \text{-tr}(W_{o,\text{linear}}) \\
& = -\text{tr}\left(\int_{t_0}^{t_1} e^{A^T(t-t_0)} C^T C e^{A(t-t_0)} dt\right) \\
\text{subject to:} \quad & \sum_{i=1}^{m} r_i = m, \; i \in 1, 2, ...m \\
& r_{S_1} + r_{S_2} + r_{S_3} + ... + r_{S_j} = k \\
& r_i \in \{0, 1\}
\end{aligned} \tag{3.22}$$

An extended version of this method would include detailed failure models for all components and materials in the PES, possibly enabling reduced safety factors and increased power density. This design strategy, however, would require significant modeling and computational effort, and is beyond the scope of the studies presented here.

3.4 Results and Discussion

3.4.1 2D placement results comparison

States where sensors should be located for the 2D reduced order model, based on enumeration and the Gramian trace metric, are given in Table 3.3. The corresponding states where sensors go on the physical domain are shown in Fig. 3.5.

Table 3.3: Optimal sensor locations for 2D reduced-order model.

Number of sensors	State Locations	Trace of Obs. Gramian
1	1	10.014
2	1,2	20.029
3	1,2,6	27.177
4	1,2,6,7	34.072
5	1,2,5,6,7	40.966
6	1,2,3,5,6,7	47.793
7	1,2,3,5,6,7,9	54.607
8	1,2,3,5,6,7,8,9	61.188
9	1,2,3,4,5,6,7,8,9	67.768

An initial comparison is made between the binary integer program, continuous relaxation, and LP placement strategies in terms of their efficiency. The computational solution time required by each method using trace of the observability Gramian as the performance metric has been assessed for both the reduced and full-order models. Results are compiled in Table 3.4. The simulations have been performed using a workstation with an Intel i5-4570 x64 processor with 4 physical cores running in parallel. Computational efficiency improves in the order presented in Table 3.4, with the LP strategy being the most efficient by a significant margin.

Table 3.4: Time comparison between enumeration, discrete, continuous and linear programming based placement schemes.

Computational Method	**Reduced-order (9 states)**	**Full-order (39 states)**
Combinatorial approach	450 sec	2.4 hrs
Discrete optimization	220 sec	0.7 hrs
Continuous method (SIMP)	10-11 sec	17-18 sec
Linear/Sorting program	0.4 to 0.45 sec	0.7-0.8 sec

A study was performed to investigate the efficiency of the LP strategy in placing sensors for high-resolution state space systems. Figure 3.8 shows the resulting Pareto fronts that illustrate the tradeoff between estimation quality and the number of sensors. Table 3.5 shows how computational solution time increases as a function of model order. Figure 3.9 illustrates for a few Pareto-optimal solutions the regions where the sensors must be placed on the board to improve observability.

Although the LP method yields efficient and accurate results, it is limited to using the trace of the observability Gramian as a performance metric. The mathematical structure of this metric can be leveraged for efficient formulation and solution, but this is not the case for more general performance metrics. The continuous relaxation strategy is appealing in that it can solve placement problems relatively efficiently, while admitting very general performance metrics (e.g., metrics must be smooth, continuous functions of the relaxed optimization variables).

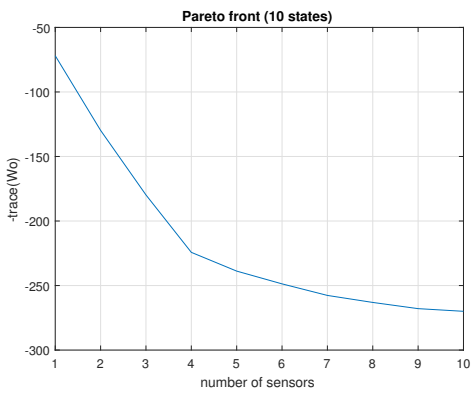

(a) Pareto front (10 states)

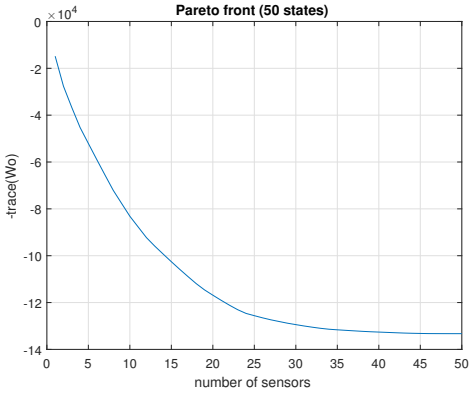

(b) Pareto front (50 states)

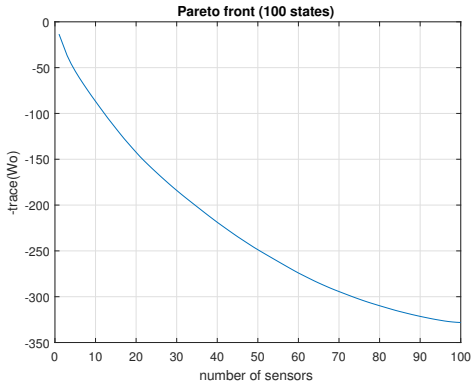

(c) Pareto front (100 states)

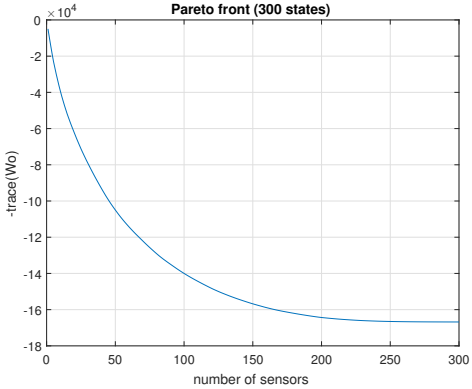

(d) Pareto front (300 states)

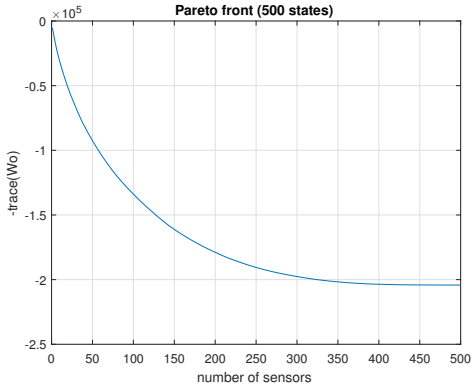

(e) Pareto front (500 states)

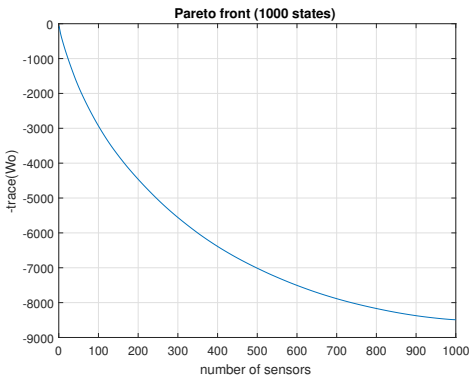

(f) Pareto front (1000 states)

Figure 3.8: Pareto fronts for optimal sensor placement using the LP strategy with random state space models of various sizes.

Table 3.5: Computational time required to obtain Pareto fronts using the LP strategy as a function of model order.

Number of states	10	50	100	300	500	1000
Solution Time (in sec)	0.7	1.2	7.5	9.7	69.5	1352.5

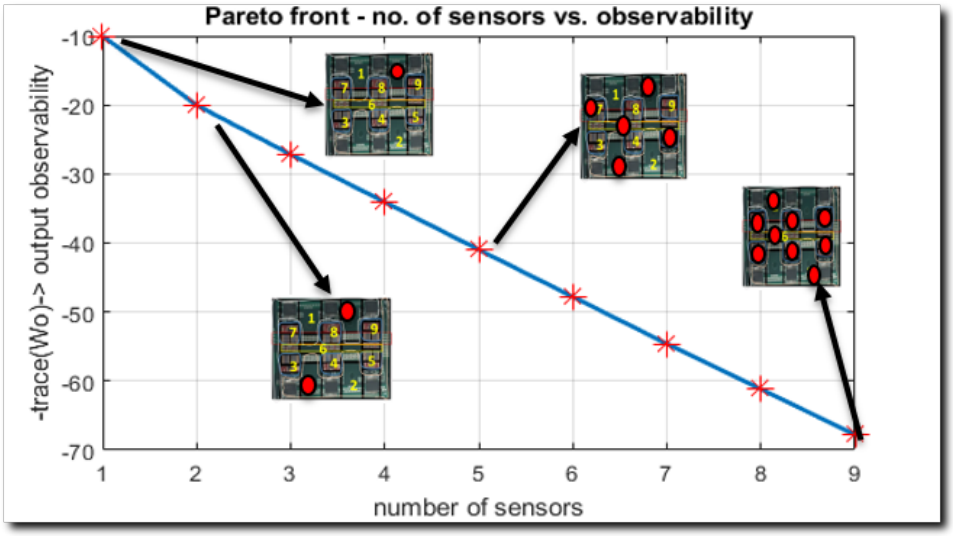

Figure 3.9: Reduced order 2D thermal model results: A selection of Pareto-optimal sensor placements are illustrated on the inverter board.

3.4.2 3D placement results comparison

The 3D sensor placement problem is similar to the 2D problem. The thermal state space model is different, so different optimal placement solutions are expected. The optimal sensor locations for 3D reduced thermal model are listed in Table 3.6. These state locations were obtained using the trace of the observability Gramian as the objective function.

As expected, the optimal sensor locations obtained here are different compared to those obtained for the 2D reduced order thermal model. The 3D system model is different from the 2D system as it takes into consideration the interaction between the heat sink and the PCB. In addition, the 3D model has a different path from the heat-generating components to the atmosphere (through the heat sink). Four of the solution methods presented in Section 3.3 were applied both to the reduced-order and the full-order 3D

Table 3.6: Optimal sensor locations for 3D reduced order model.

Number of sensors	State Locations	Trace of Obs. Gramian
1	2	8.6627
2	1,2	17.3255
3	1,2,6	25.9836
4	1,2,4,6	34.6370
5	1,2,4,6,10	43.2900
6	1,2,4,6,8,10	51.9420
7	1,2,4,5,6,8,10	60.5934
8	1,2,4,5,6,7,8,10	69.2448
9	1,2,4,5,6,7,8,9,10	77.8963
10	1,2,3,4,5,6,7,8,9,10	86.5477

models. The computational solution times are listed in Table 3.7 using the same processor that was used as for the 2D sensor placement problem.

Table 3.7: Solution time comparison between enumeration, discrete, continuous, and LP sensor placement strategies for the 3D inverter system.

Computational Method	Reduced-order (10 states)	Full-order (78 states)
Combinatorial approach	515 sec	6.3 hrs
Discrete optimization	279 sec	2.1 hrs
Continuous method (SIMP)	11-13 sec	36-138 sec
Linear/Sorting program	0.55-0.70 sec	1.2-1.4 sec

3.5 Experimental Validation

The design framework that has been proposed has been experimentally validated using a prototype inverter described in Section 3.1. After the Pareto sets were obtained for the 2D and 3D thermal models, the thermal estimation was performed using an optimal continuous-discrete Kalman filter. The estimation procedure adopted here is detailed in Ref. [61]. Selecting the number of sensors to be used can be supported knowing the state estimation error obtained from the Kalman filter. The sum of the absolute value of the estimation error versus the number of sensors is shown both for the 2D system and the 3D system respectively in Tables 3.8 and 3.9.

It can be seen that in both the cases the error remains nearly constant af-

Table 3.8: Sum of absolute estimation error vs. number of sensors with 2D reduced-order model (9 states)

Number of sensors	2	3	4	5	6	7	8	9
Absolute estimation error (in deg.C)	40	37.6	19.8	5.1	4.7	3.1	1.9	0.4

Table 3.9: Sum of absolute estimation error vs. number of sensors with 3D reduced-order model (10 states)

Number of sensors	2	3	4	5	6	7	8	9	10
Absolute estimation error (in deg.C)	38.4	13.8	6.2	4.0	2.2	2.1	2.0	0.9	0.3

ter reaching a certain number of sensors (five and six sensors for the 2D and 3D systems, respectively). Hence, five and six sensors (for the 2D and 3D systems, respectively), appear to be ideal choices that balance the number of sensors and temperature estimation error. The optimal sensor locations for these two cases listed in Tables 3.3 and 3.6 are (1,2,5,6,7) and (1,2,4,6,8,10), respectively. We know that a group of nodes in the full-order model are combined into a super-node in the reduced order model. Although these optimal locations correspond to the super-nodes of the reduced full-order model, each super-node is comprised of several nodes where a sensor could go. The designer could pick that node (a state location) from the super-node which has greater observability than the other nodes (states) in that super-node. The optimal sensor locations for the full order 2D and 3D thermal models are provided in Table A.1 and Table A.2, respectively, in the Appendix section.

The 2D experimental validation was performed on the prototype inverter using an FLIR T420 IR (Infra-Red) camera that captures a thermal video of the board when it is under operation. Figure 3.10 shows two thermal snapshots of the PCB. The ambient temperature during the operation of the inverter PCB was 30° C. Figure 3.11 (verified in Ref. [61]) shows how temperature estimates of states 1, 2, 5, and 6 of the 2D reduced-order thermal model are in good agreement (error within +/- 3°C) with experimental temperatures of those regions measured using the IR camera. This clearly shows how the estimation technique using the continuous discrete Kalman filter with just 5 sensors can predict accurately the PCB temperatures PCB

within a small tolerance value.

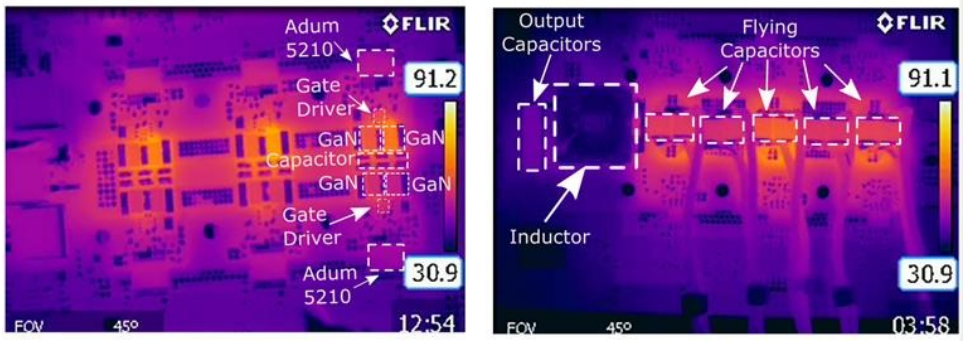

Figure 3.10: Annotated Snapshot from IR Measurement of the operating multilevel inverter at an input power level of 550 W.

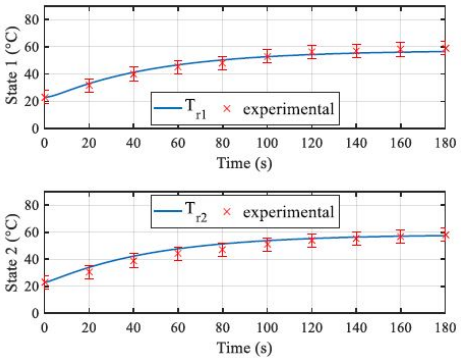

(a) Estimated states 1 and 2 of 2D reduced order model vs experimental IR cam temperature.

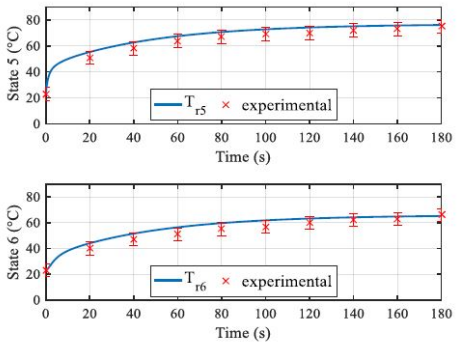

(b) Estimated states 5 and 6 of 2D reduced order model vs experimental IR cam temperature

Figure 3.11: Comparison of estimated states from 2D reduced order model with experimental results.

Since the 3D system is enclosed by an inverter, it is not possible to obtain a direct IR camera image to validate the thermal profile. In order to obtain experimental temperature data, 13 sensors were placed on the inverter board. Figures 3.12 and 3.13 show the experimental setup of the 3D PES with 13 thermocouples installed for reconstructing the dynamic thermal profile and fault diagnosis of the 3D PES tested in Ref. [3]. The measurements obtained from these thermocouples are presented in Fig. 3.14.

It was observed that one of the components on the power inverter failed during this test. The faulty component was detected using the IR camera

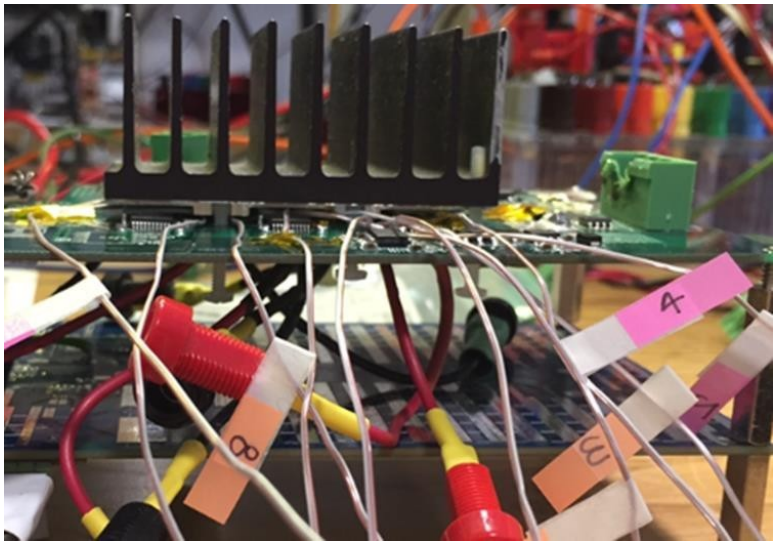

Figure 3.12: Cross-sectional view of the experimental setup with 13 thermocouples.

Figure 3.13: Top view of the experimental setup with a faulty component indicated using a red circle located at the right bottom.

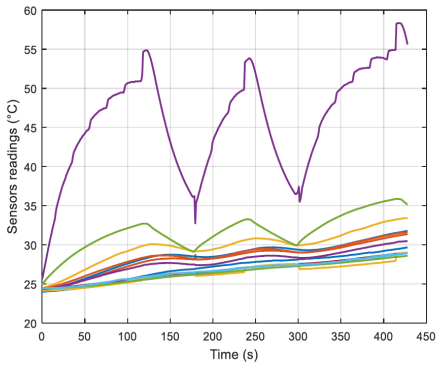

Figure 3.14: Measurements from the 13 thermocouples obtained from the previous work detailed in Ref. [3].

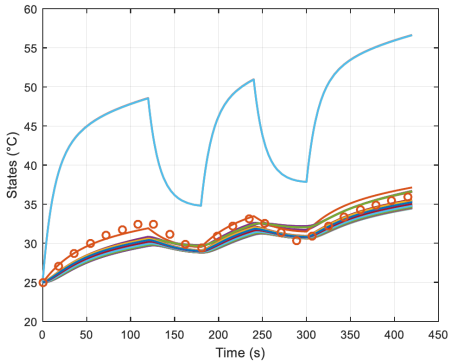

Figure 3.15: The prediction of state 5 using the 78-state full-order model is shown in circles.

without the heat sink on top of the board, and is shown using a red circle in Fig. 3.13. Figure 3.15 shows the estimated readings of all the 78 states of the 3D full-order thermal model. They agree well with the experimental readings shown in Fig. 3.14 obtained using 13 physical sensors, accounting for the faulty component. Based on these experiments, it can be seen clearly how the online estimation procedure based on optimal sensor placement is not only helpful in accurately reconstructing the dynamic thermal behaviour of the inverter but also useful in fault diagnosis.

CHAPTER 4

COOLING SYSTEM ARCHITECTURE DESIGN

4.1 Motivation

There is an emergent need for the development of high performance cooling systems for efficient fluid-based thermal management of high density power electronic systems. As the size and complexity of electro-thermal systems increases, it is becoming a challenging task to design cooling system architectures that are both cost-effective and optimal, especially when neither intuition nor human experience are adequate. Dense circuitry and tight packaging of power electronic systems makes thermal management a very difficult design task. As discussed in Chapter 1, removal of waste heat is critical to ensuring reliability and sustainability of systems in extreme environments. The goal of this research is to provide a general design methodology for cooling system architecture design that is relevant to a range of applications.

4.2 Related Works

The 21st century is seeing a continuing trend toward greater electrification of systems in industrial, transportation, agricultural, and consumer applications [4, 5, 76]. Large quantities of waste thermal energy are generated by high-power electrical systems, including electro-mechanical devices, electronic power converters, battery systems, and other electro-thermal systems. The performance, efficiency, safety, and life cycle of components within these systems can depend strongly on temperature. Therefore, thermal management systems are tasked with maintaining operating temperatures to within their specified limits. While waste thermal energy must ultimately be rejected to the environment, it is often first transferred from heat-generating

components to a liquid coolant circulating through a network of pipes. Control of these fluid-based thermal management systems requires determining command inputs to all valves and pumps in the fluid network. Designing and controlling such systems becomes a challenging task as they increase in both size and complexity, commensurate with the systems that they cool.

A thermal management system must not only be energy efficient and reliable, but also help reduce capital cost in terms of cooling network size, complexity, and fabrication cost. Mobile systems have additional considerations, such as size and weight limitations, and possibly more limited options for cooling mechanisms. Cooling system architecture can affect all of the above attributes. Poor architectures can result in sudden failure of temperature-sensitive components or lead to long-term degradation when operating temperature constraints cannot be maintained, while over-cooling can reduce the component efficiency. The cooling system architecture design must balance maintaining the temperature constraints of individual components with overall system considerations such as pumping efficiency and geometric packaging. Performance metrics can vary widely. For example, aircraft thermal management systems can be characterized by their thermal endurance, defined as the duration of operation before any temperature constraint is violated, to ensure safe operation and maximum range [77]. Other applications, such as hybrid-electric vehicles [78] or server farms [79] may have a different set of requirements. As new cooling system applications and requirements emerge, engineers must learn how best to meet new needs, sometimes without the benefit of design heritage or the associated expert knowledge for particular systems. Cooling system architecture design problems can have a vast design space that is cognitively difficult to navigate, motivating efficient systematic design methods with the flexibility to explore and assess new configurations.

Even without the use of systematic design methods, recent work has illustrated the sub-optimality of conventional thermal management architectures. For example, Ref. [77] demonstrates that a dual fuel tank topology for an aircraft can achieve a 35% improvement in thermal endurance over a conventional single fuel tank topology under closed-loop control. In the dual configuration, one tank is used in a standard recirculation loop, while the second tank acts as an auxiliary reservoir. This reduces the thermal capacitance of the recirculation loop as compared to the single tank topology,

allowing the temperature of the fuel feeding the engine to increase faster and therefore removing more thermal energy from the system when that fuel is burned early in flight. The decision to analyze this dual-tank topology aligns with the concept of minimizing exergy destruction in thermal systems [80], however, in the absence of exhaustive or other systematic design studies it is left to engineering intuition to conceive of unconventional topologies such as this. This begs the question of whether systematic design methods could suggest additional modifications to conventional configurations for this class of systems to improve performance, efficiency, or robustness.

Many past efforts have focused on improving individual components in a cooling system, but few have addressed overall system design. Examples of the latter include Refs. [81, 82]. In Ref. [81] a design methodology was developed to predict cooling tower performance considering heat load distributions. In Ref. [82], interactions between a heat exchanger network and cooling tower were considered. Cooling system architecture studies typically focus on a single application such as process utilities in petrochemical plants [83] or multi-chip processors [84], as opposed to a general design framework. Existing architecture studies have often been limited in scope to improve tractability. For example, rearranging components in a given topology restricts problem complexity, but limits broad exploration of new designs [85].

4.3 Design Methodology and Contributions

In this work, simplifying model assumptions are made that support tractability while retaining important physical effects and applicability to a wide range of thermal management system applications. Many of these assumptions have been validated in previous experimental work [86], and are discussed in more detail in later sections where appropriate. The design methodology presented here:

- Uses dynamic graph-based modeling to provide flexibility in assessing a variety of different cooling system types,
- Supports systems with multiple temperature-sensitive components having high heat loads and different maximum allowable temperatures,

- Is applicable to small to medium-scale systems, whereas extension to large-scale systems is a topic of ongoing work. Here small and medium-scale architecture design problems are defined to be those that are solvable via recently-developed efficient enumeration techniques [87]).
- Uses flexible solution methods such as variable-horizon direct optimal control, and
- Determines optimal coolant flow distribution across the system, balancing competing objectives.

Primary contributions include 1) a new method for enumerating system architectures modeled using graphs as labeled rooted trees, and 2) a rigorous method for comparison between candidate architectures [1]. The first contribution builds on recent work in efficient methods for architecture enumeration [87]. The second contribution is enabled by recent advancements in direct optimal control [88, 89] .

For each architecture, flow is distributed optimally across the system such that thermal endurance is maximized across components operating under different heat loads and temperature constraints. The highest performing architectures are then determined as those with the greatest thermal endurance. Here the design scope is limited to a fluid-based thermal management system with a single junction and single-split. However, the class of architectures considered in this work can be used as canonical architectures that can be built upon to generate other complex architectures. Hence, future work will expand this to include architectures with greater degrees of freedom in topological design.

4.4 Graph-based system modeling

The class of thermal management system architectures considered in this thesis is depicted in Fig. 4.1. The primary purpose of the system is to manage the operating temperature of a number of heat-generating electrical or mechanical components, each mounted to a cold plate heat exchanger (CPHX)

[1] The work presented in this chapter on graph-based modeling and labeled rooted tree graph generation was performed in collaboration with graduate student Herschel Pangborn (pangbor2@illinois.edu) and post-doctoral scholar Daniel Herber (herber1@illinois.edu).

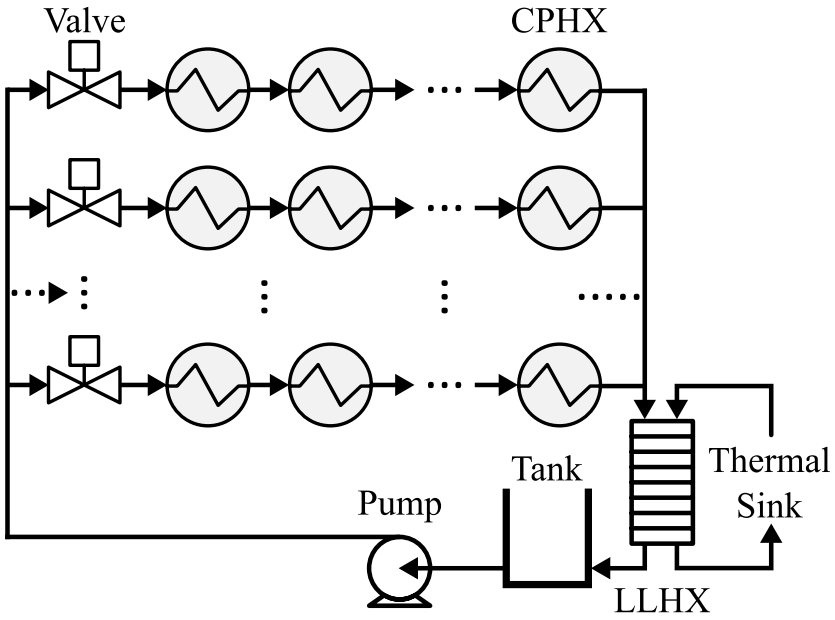

Figure 4.1: Illustration of the class of cooling system architectures considered, consisting of cold plate heat exchangers (CPHXs) in series and parallel, and constrained to have a single split/junction in the coolant flow.

through which a coolant flows. This fluid is stored in a tank and driven by a pump through a set of N_f *parallel* flows, each of which includes a variable-aperture valve v. The fluid in each parallel flow passes through a number of CPHXs in *series*, absorbing thermal energy from the CPHX walls. Thermal energy is transferred from the fluid to a thermal sink (e.g., a secondary loop regulated by a vapor compression cycle system [86]) via a liquid-to-liquid heat exchanger (LLHX). This class of architectures is representative of many single-phase fluid-based thermal management systems, such as those found in aircraft [90, 91], electrified automobiles [92], and server farms [79].

The total number of CPHXs, which is assumed to be fixed for a given design study, is denoted as N_c. We assume that the heat load applied to each CPHX, as well as the temperature and mass flow rate of the thermal sink fluid, are known exogenous disturbances. and that the temperature of each heat-generating component is the same as the temperature of the wall of the CPHX to which it is mounted. The thermal management system is controlled by commanding the rotational speed of the pump and the position of each variable-aperture valve.

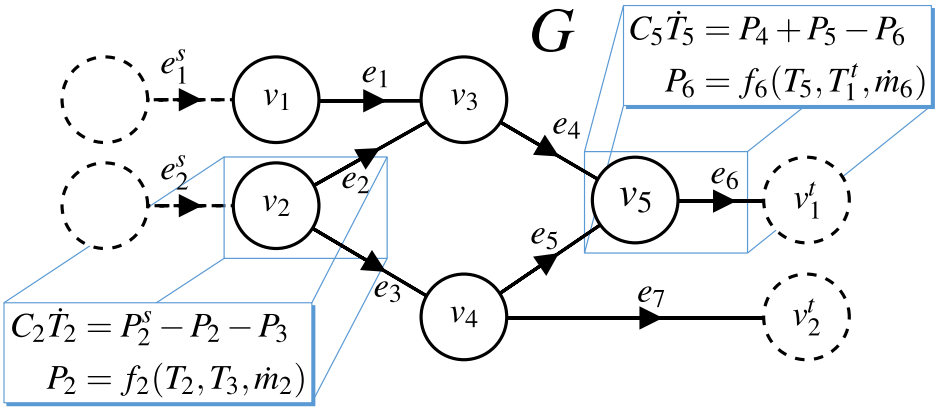

Figure 4.2: Notional graph example to demonstrate key features of the modeling approach.

4.4.1 Dynamic Graph-Based Modeling

One approach for the lumped parameter dynamic modeling of power flow systems, including the class of thermal management architectures considered here, is to apply conservation equations within a graph-based framework, where vertices represent the capacitive storage of energy and edges represent the paths along which power can flow between vertices [86, 93–96]. This graph-based approach is particularly well-suited for architecture exploration and optimization because the models are generated from a structural mapping of interconnections that can be constructed in a programmatic way and leveraged in both system analysis and control design. The remainder of this subsection presents an overview of the graph-based modeling approach, which is then contextualized to the type of architectures considered in this thesis.

In graph-based modeling, the structure of interconnections of the system is described by the oriented graph $G = (\boldsymbol{v}, \boldsymbol{e})$ of order N_v with vertices $\boldsymbol{v} = [v_i], i \in \{1, 2, ..., N_v\}$, and size N_e with edges $\boldsymbol{e} = [e_j], j \in \{1, 2, .., N_e\}$. As shown in the notional graph example of Fig. 4.2, each edge e_j is incident to two vertices and indicates directionality from its *tail* vertex v_j^{tail} to its *head* vertex v_j^{head}. The set of edges directed into vertex v_i is given by $e_i^{head} = \{e_j | v_j^{head} = v_i\}$, while the set of edges directed out of vertex v_i is given by $e_i^{tail} = \{e_j | v_j^{tail} = v_i\}$ [97].

Each vertex has an associated dynamic state associated with energy storage. For thermal systems, this state is the temperature of a thermal element,

T_i. Each edge has an associated quantity P_j describing the rate of transfer of thermal energy (equivalently referred to as thermal power flow in this thesis) between adjacent vertices. The orientation of each edge indicates the convention assigned to positive power flow, from v_j^{tail} to v_j^{head}. Therefore, the dynamics of each state satisfy the conservation equation:

$$C_i \dot{T}_i = \sum_{\left\{j | e_j \in e_i^{head}\right\}} P_j - \sum_{\left\{j | e_j \in e_i^{tail}\right\}} P_j \tag{4.1}$$

where $C_i > 0$ is the thermal capacitance of the vertex. In words, Eqn. (4.1) states that the rate of thermal energy storage in the vertex is equal to the total thermal power flow into the vertex minus the total thermal power flow out of the vertex.

For the fluid-based thermal system in this work, the power flow P_j along each edge is a function of the temperature states of the vertices to which it is incident and may also be a function of an associated mass flow rate $\dot{m}_j$ which can be treated as an input to the thermal system model [86, 93–95]. The transfer rate along each edge is therefore given generically by:

$$P_j = f_j\left(T_j^{tail}, T_j^{head}, \dot{m}_j\right) \tag{4.2}$$

Figure 4.2 includes examples of Eqns. (4.1) and (4.2) as applied to several vertices and edges.

In addition to capturing the exchange of energy within the graph, the modeling framework must account for exchange with entities external to the graph. Sources to graph G are modeled by source edges $\boldsymbol{e}^s = [e_j^s], j \in \{1, 2, ..., N_s\}$ with associated power flows $\boldsymbol{P}^s = [P_j^s]$, which are treated as disturbances to the system that may come from neighboring systems or the environment. Therefore, edges belonging to $\boldsymbol{e}^s$ are not counted among the edges $\boldsymbol{e}$ of graph G, and transfer rates in $\boldsymbol{P}^s$ are not counted among the internal transfer rates $\boldsymbol{P}$ of the system.

Sinks of graph G are modeled by sink vertices $\boldsymbol{v}^t = [v_j^t], j \in \{1, 2, ..., N_t\}$ with associated states $\boldsymbol{T}^t = [T_j^t]$. The sink vertices are counted among the vertices $\boldsymbol{v}$ of graph G, but the sink states $\boldsymbol{T}^t$ are not included in the state vector $\boldsymbol{T}$ of the system. Instead, the sink states $\boldsymbol{T}^t$ are treated as disturbances to the system associated with neighboring systems or the environment.

To describe the structure of edge and vertex interconnections of a graph,

the incidence matrix $\boldsymbol{M} = [m_{i,j}] \in \mathbb{R}^{N_v \times N_e}$ is defined as:

$$m_{i,j} = \begin{cases} +1 & v_i \text{ is the tail of } e_j, \\ -1 & v_i \text{ is the head of } e_j, \\ 0 & \text{else.} \end{cases} \tag{4.3}$$

$\boldsymbol{M}$ can then be partitioned as:

$$\boldsymbol{M} = \begin{bmatrix} \bar{\boldsymbol{M}} \\ \underline{\boldsymbol{M}} \end{bmatrix} \text{ with } \bar{\boldsymbol{M}} \in \mathbb{R}^{(N_v - N_t) \times N_e}, \tag{4.4}$$

where the indexing of edges is assumed to be ordered such that $\bar{\boldsymbol{M}}$ is a structural mapping from power flows $\boldsymbol{P}$ to states $\boldsymbol{T}$, and $\underline{\boldsymbol{M}}$ is a structural mapping from $\boldsymbol{P}$ to sink states $\boldsymbol{T}^t$.

Similarly, the connection of external sources to the system is given by $\boldsymbol{D} = [d_{i,j}] \in \mathbb{R}^{(N_v - N_t) \times N_s}$ where:

$$d_{i,j} = \begin{cases} 1 & v_i \text{ is the head of } e_j^s, \\ 0 & \text{else.} \end{cases} \tag{4.5}$$

Following from the conservation equation for each vertex in Eqn. (4.1) and the above definitions of $\bar{\boldsymbol{M}}$ and $\boldsymbol{D}$, the dynamics of all states in a system are given by:

$$\boldsymbol{C}\dot{\boldsymbol{T}} = -\bar{\boldsymbol{M}}\boldsymbol{P} + \boldsymbol{D}\boldsymbol{P}^s \tag{4.6}$$

where $\boldsymbol{C} = \text{diag}([C_i])$ is the diagonal matrix of capacitances.

Following from Eqn. (4.2), the vector of all power flows $\boldsymbol{P}$ in a system is given by:

$$\boldsymbol{P} = \boldsymbol{F}(\boldsymbol{T}, \boldsymbol{T}^s, \dot{\boldsymbol{m}}) = [f_j(T_j^{tail}, T_j^{head}, \dot{m}_j)]. \tag{4.7}$$

4.5 Candidate Architecture Modeling

To demonstrate the design methodology, the scope of studies in this thesis have been limited to a specific class of cooling system architectures.

4.5.1 Graph-Based Model for the Class of Architectures

Figure 4.3 shows the graph corresponding to the class of system architectures considered in this thesis. To model this class using the graph-based approach of Section 4.4.1, vertices are assigned to represent the temperature of the fluid in the tank, the temperature of the fluid in each CPHX and the wall of each CPHX, and the temperature of the fluid in each side of the LLHX and the wall of the LLHX. The thermal capacitance associated with states representing a fluid temperature in Eqn. (4.1) is given by $C_i = \rho V_i c_p$, where V is the volume of the stored fluid, c_p is the specific heat capacitance of the fluid, and ρ is the density of the fluid. The thermal capacitance associated with states representing a wall temperature is given by $C_i = M_{w,i} c_{p,w,i}$, where M_w is the mass of the wall and $c_{p,w}$ is the specific heat capacitance of the wall material. All thermal capacitances in this work are assumed to be constant.

In this thesis, the modeling of two types of thermal power flow is required to capture the exchange of thermal energy between temperature states of the graph. The first is power flow due to convective heat transfer, given by $P_j = h_j A_{s,j}(T_j^{tail} - T_j^{head})$, where A_s is the convective surface area and h is the heat transfer coefficient, assumed to be constant in this thesis. This type of power flow occurs between the wall and the fluid of each CPHX, and between the wall and the fluid on each side of the LLHX.

The second type of thermal power flow is advection associated with fluid flow, given by $P_j = \dot{m}_j c_p T_j^{tail}$, where $\dot{m}$ is the mass flow rate of the fluid and c_p is the specific heat capacitance of the fluid, assumed to be constant in this work. When fluid flows in a loop between two thermal elements, as between the secondary side of the LLHX and the thermal sink, the advective power flow in each direction can be combined into a single "bidirectional advection" power flow, given by $P_j = \dot{m}_j c_p (T_j^{tail} - T_j^{head})$.

Based on the above discussion, for every power flow in the graph-based model of the class of architectures, Eqn. (4.2) can be put in the form:

$$P_j = a_{1,j} T_j^{tail} + a_{2,j} T_j^{head} + b_{1,j} \dot{m} T_j^{tail} + b_{2,j} \dot{m} T_j^{head} \tag{4.8}$$

where the coefficients $a_{i,j}$ and $b_{i,j}$ are constants. The source power flows P^s of the graph-based model for the class of system architectures consist of the heat load to each CPHX from the heat-generating device to which it is

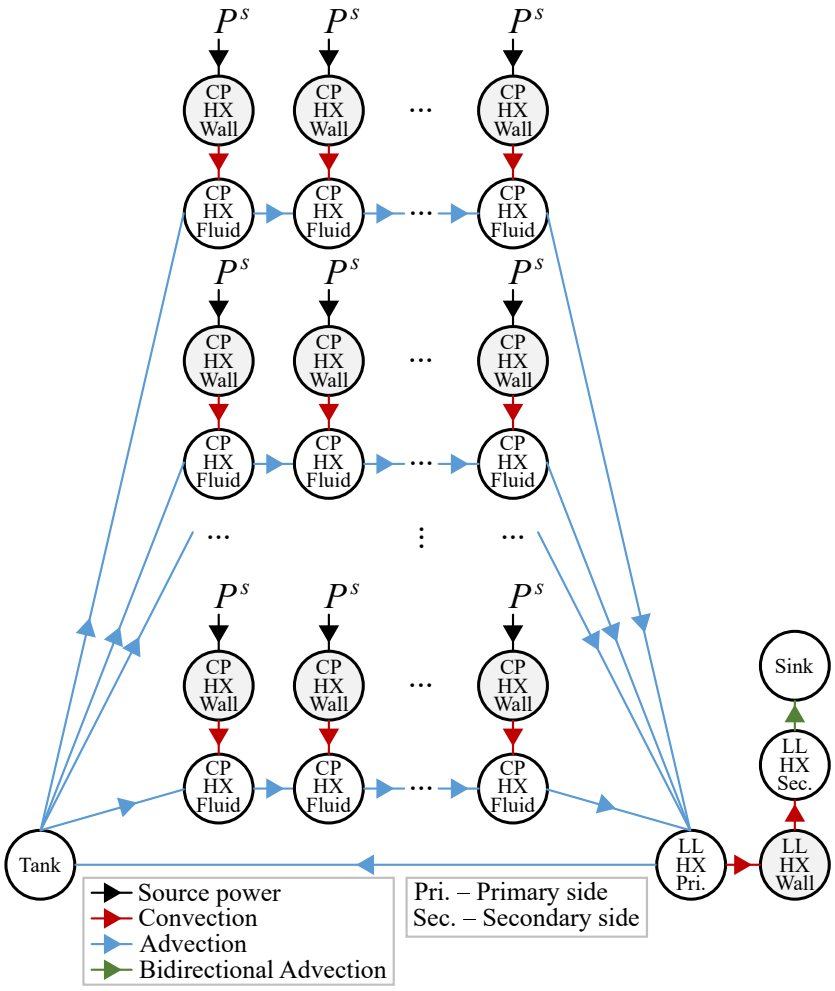

Figure 4.3: Graph for the class of thermal management architectures considered in this thesis. Vertices representing fluid temperatures are colored white, while vertices representing wall temperatures are colored gray.

mounted. The lone sink state of the system T^t is the temperature of the thermal sink.

In this thesis, as in Ref. [77], it is assumed that the valves can be controlled such that the flow through the pump can be split with any desired proportioning into each of the parallel flows. It is also assumed that the upper and lower bounds on the mass flow rate achievable by the pump are independent of the number of parallel flows, number of CPHXs in each parallel flow, and valve positions. While the hydraulic modeling that would be necessary to remove this assumption falls outside the scope of this study, previous work has included graph-based modeling of the hydrodynamics of a fluid system, where it is demonstrated that hydraulic and thermal graphs-based models of a system can be interconnected to capture both these domains using a common modeling approach [86, 93].

Experimental validation of the graph-based modeling approach for similar fluid-thermal architectures can be found in Refs. [86, 93, 95]. This has shown the modeling approach to be consistently accurate within approximately 2 °C, including under transient behavior, while executing orders of magnitude faster than real time on modern desktop computers. This provides both sufficient accuracy and sufficient computational simplicity to support studies in system and control design. The parameters used in Section 5.2 were nominally sized in accordance with the parameters used for experimental validation in the previous work [86, 93, 95]. Several of the key parameters are listed in Table 5.1. Each CPHX is assumed to be identical, although the heat load applied to each CPHX may be different. The working fluid is assumed to be an equal parts mixture of propylene glycol and water.

4.5.2 State Equations for the Graph-Based Model

Let $\boldsymbol{M}_a = [\tilde{m}_{i,j}]$ be a weighted incidence matrix defined by:

$$\tilde{m}_{i,j} = \begin{cases} a_{1,j} & \text{if } v_i \text{ is the tail of } e_j, \\ a_{2,j} & \text{if } v_i \text{ is the head of } e_j, \\ 0 & \text{else.} \end{cases} \tag{4.9}$$

where $a_{i,j}$ are the coefficients in Eqn. (4.8). $\boldsymbol{M}_b$ can be defined similarly

using the coefficients $b_{i,j}$ in Eqn. (4.8).

Note that there is not a one-to-one relationship between the mass flow rates of the system architecture and the edges of its thermal graph. For example, the mass flow rate through each CPHX of a given parallel flow is the same. Therefore, the set of unique mass flow rates of the system can be mapped to the set of edges of the graph by:

$$\dot{\boldsymbol{m}}_e = \boldsymbol{Z} \begin{bmatrix} \dot{m}_p \\ \dot{\boldsymbol{m}}_f \\ \dot{m}_t \end{bmatrix}, \qquad \boldsymbol{Z} \in \{0,1\}^{N_e \times (2+N_f)}, \tag{4.10}$$

where $\dot{m}_p$ is the mass flow rate rate through the pump, $\dot{\boldsymbol{m}}_f$ is the vector of mass flow rates through each parallel flow, and $\dot{m}_t$ is the mass flow rate of the thermal sink. From Eqn. (4.6) and Eqns. (4.8)--(4.10), the state-space equation for the system architecture can be written as:

$$\dot{\boldsymbol{T}} = \boldsymbol{A} \begin{bmatrix} \boldsymbol{T} \\ T^t \end{bmatrix} + \boldsymbol{B}_1 \text{diag} \left(\boldsymbol{Z} \begin{bmatrix} \dot{m}_p \\ \dot{\boldsymbol{m}}_f \\ \dot{m}_t \end{bmatrix} \right) \boldsymbol{B}_2 \begin{bmatrix} \boldsymbol{T} \\ T^t \end{bmatrix} + \boldsymbol{D}\boldsymbol{P}^s, \tag{4.11}$$

where:

$$\boldsymbol{A} = -\boldsymbol{C}^{-1}\bar{\boldsymbol{M}}\bar{\boldsymbol{M}}_a^T \tag{4.12a}$$

$$\boldsymbol{B}_1 = -\boldsymbol{C}^{-1}\bar{\boldsymbol{M}} \tag{4.12b}$$

$$\boldsymbol{B}_2 = \bar{\boldsymbol{M}}_b^T \tag{4.12c}$$

and $\boldsymbol{D}$ is as defined in Eqn. (4.5). For a given number of parallel flows and number of CPHXs in each flow, the corresponding state-space model in the form of Eqn. (4.11) can be programmatically generated.

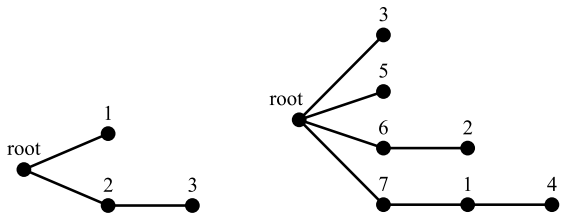

(a) $1-23$. (b) $3-5-62-714$.

Figure 4.4: Two labeled rooted tree graphs in the class of graphs of interest.

4.6 Generating New Architectures with Labeled Rooted Tree Graphs

4.6.1 Representation as Labeled Rooted Tree Graphs

The class of architectures $\mathcal{A}$ can be represented as labeled rooted tree graphs. In graph theory, a tree is a undirected graph in which any two vertices are connected by unique simple path [98,99]. An equivalent definition is an undirected graph that is connected and has no cycles. Here a labeled rooted tree is a tree where the root is labeled with 0 and each other vertex is assigned a unique integer value from 1 to N_c [99]. The architectures in $\mathcal{A}$ are representable by labeled rooted trees because the labels in the tree (other than the root) correspond to specific CPHXs in a predefined list and the fluid is defined to flow away from the root. Finally, to completely define $\mathcal{A}$, we require all the vertices in the tree except the root to have at most one child. Two example trees are shown in Fig. 4.4 along with a unique direct representation. This direct representation, specific to single-split architectures, utilizes "–" to indicate a connection to the root (split) and neighboring CPHX numbers that are connected in series, with the leftmost number connected to the root.

The number of unlabeled rooted trees of interest with $N_c + 1$ nodes is equivalent to the partition numbers (i.e., different ways of writing N_c as a sum of positive integers). For a given partition, each summation represents an additional valve, and the integers represent the number of CPHXs in series with a particular v. For example, $1+3+3$ and $1+1+2+3$ are two of the 15 unique partitions for $N_c = 7$. The number of partitions for different N_c is

given by OEIS A000041 [99, 100]:

$$S_u = 1, 2, 3, 5, 7, 11, 15, 22, 30, 42, 56, \ldots \tag{4.13}$$

However, trees generated using these partitions are unlabeled. To determine the number of labeled rooted trees, we can naively consider all permutations of the vertices for each partition, providing the upper bound on the number of architectures as:

$$|\mathcal{A}(N_c)| = S_l(N_c) \leq N_c! \times S_u(N_c) \tag{4.14}$$

This is only an upper bound as there will potentially be isomorphic graphs [99] using the naive permutations. Fortunately, we can directly account for the isomorphic graphs by considering the number of instances of a specific integer in the partition and their permutations:

$$|\mathcal{A}(N_c)| = \sum_{k=1}^{S(N_c)} \left[N_c! \times \left(\prod_{i=1}^{N_c} I(k,i)! \right)^{-1} \right] \tag{4.15}$$

where $I(k,i)$ is the number of times the integer i appears in partition k (e.g., if we have partition $k : 1 + 2 + 2 + 2$, then $I(k,2) = 3$) and I can be computed with Ref. [101]. The first few values for the number of unique architectures for increasing N_c are:

$$S_l = 1, 3, 13, 73, 501, 4051, 37633, 394353, \ldots \tag{4.16}$$

The 13 unique cooling system architectures for $N_c = 3$ are shown in Fig. 4.7. This information will be used when generating each of the trees. Table 4.1 below shows the time complexity to generate trees for N_c ranging from 1 to 10. The labelled rooted trees generated for a sample $N_c = 4$ and 6 are shown in Fig. 4.5 and Fig. 4.6 respectively.

4.6.2 Generating the Labeled Rooted Tree Graphs

Here we will utilize the parent pointers representation of a tree graph where the kth child (vertex labeled with k) of vector V has the parent node $V(k)$ [98]. For example, $V = [0\ 3\ 0]$ defines the labeled rooted tree in Fig. 4.7c. To enu-

Table 4.1: Time complexity to generate labeled rooted trees for N_c from 1 to 10

n	**S(n)**	**N**	**t(s)**
1	1	1	0.000075
2	2	3	0.000105
3	3	13	0.00016
4	5	73	0.000522
5	7	501	0.003206
6	11	4051	0.027741
7	15	37633	0.288439
8	22	394353	3.382594
9	30	4596553	44.315895
10	42	58941091	646.033944

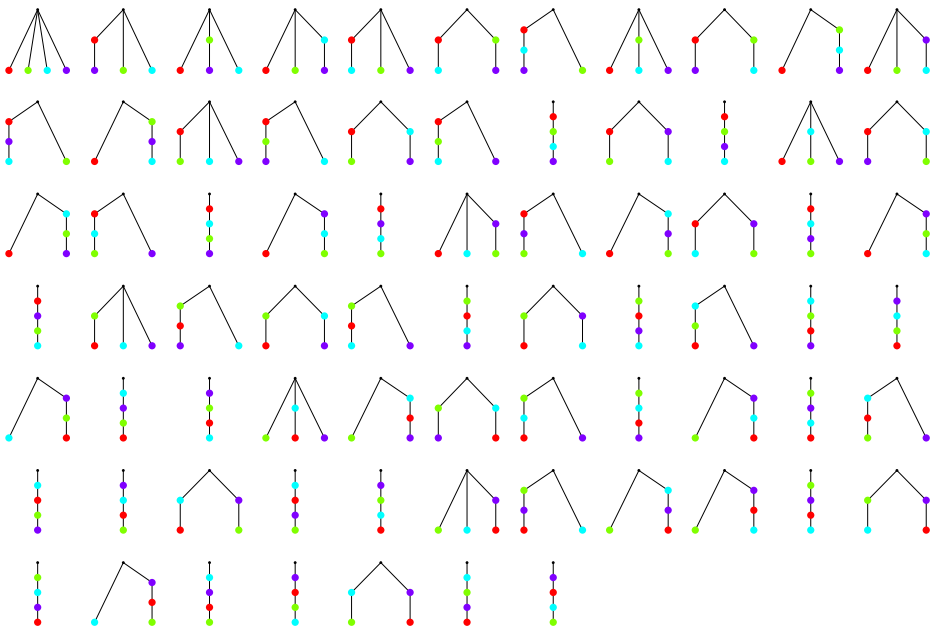

Figure 4.5: All 73 labeled rooted tree graphs for $N_c = 4$.

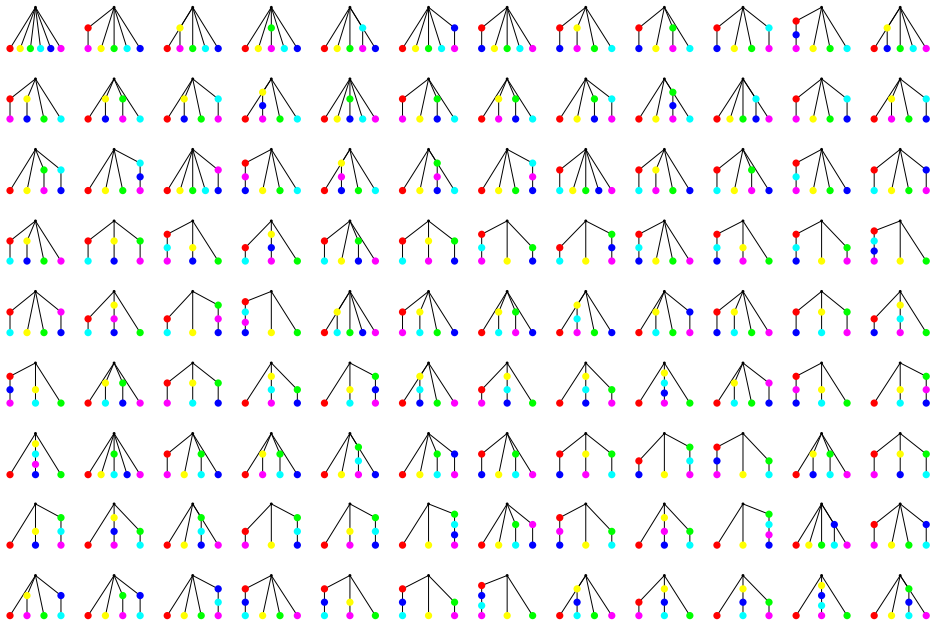

Figure 4.6: All 501 labeled rooted tree graphs for $N_c = 6$.

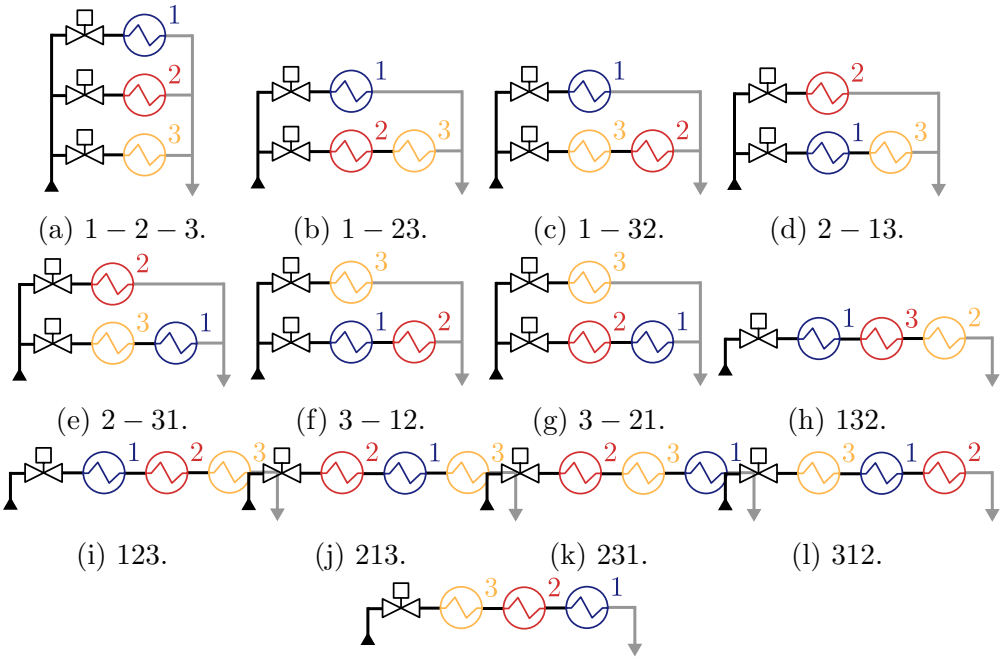

Figure 4.7: The 13 unique architectures when $N_c = 3$.

merate all possible labeled rooted trees with all the vertices except the root having at most one child, a recursive algorithm was developed.

Some key features of the approach are:

1. Recursively generating all vectors of length N_c with integer entries from 0 to N_c by adding one child-parent entry at a time.

2. Keeping a list of potential parents and removing vertices that already have a child from this list during the recursion. The root node is always a potential parent. This ensures the single-junction structure of the trees.

3. Removing any graphs that have a cycle added during the recursion (since they are not trees).

Due to the special structure of the parent pointers representation, all of the generated trees are unique. We can readily generate the listing of all the trees up to $N_c = 10$, where we start to have data storage issues due to the combinatorial nature of the problem. These listings will serve as a basis for evaluating all potential cooling system architectures for a given problem.

CHAPTER 5

OPTIMAL FLOW CONTROL PROBLEM

5.1 Optimal Coolant Flow Control Problem

To study the thermal performance of the candidate architectures, a dynamic optimization problem is posed. The goal of this optimization problem is to maximize the thermal endurance of a candidate architecture, defined as the length of time before any temperature state violates its upper bound under a given heat load profile. To continue operation past this time, the system must risk failure or degradation due to operating beyond its thermal limits, or the devices generating thermal energy must be throttled to reduce the heat loads applied to the cooling system. Increasing thermal endurance therefore often facilitates improved performance or capability of the systems being cooled. In many cases, heat load profiles may resemble square waves, pulsing in accordance with the duty cycle of electrical or mechanical devices. Thermal endurance under a constant heat load is then representative of the maximum pulse duration that can be tolerated before the system must be allowed to cool down.

The variable time optimal control problem provides an upper limit on length of the time horizon t_{end} such that the constraints of the problem are still satisfied:

$$\min_{\dot{\boldsymbol{m}}_f, t_{\text{end}}} \quad -t_{\text{end}}, \tag{5.1}$$

where $\dot{\boldsymbol{m}}_f$ are the open-loop control variables used to regulate the valve flow rates.

The dynamics for this problem are then a combination of Eqn. (4.11) and

additional states to capture $\ddot{\boldsymbol{m}}_f$:

$$\dot{\boldsymbol{\xi}} = \begin{bmatrix} \dot{\boldsymbol{T}} \\ \ddot{\boldsymbol{m}}_f \end{bmatrix} \tag{5.2}$$

where $\boldsymbol{T}$ is the vector of temperature states, $\dot{\boldsymbol{T}}$ is given in Eqn. (4.11), T^t is the temperature of the thermal sink (the chiller), and there are $n_\xi = 4 + 2N_c + N_f$ states.

The next constraint initializes the temperature states of the system:

$$\boldsymbol{T}_w(0) = T_{w,0}, \quad \boldsymbol{T}_f(0) = T_{f,0}, \quad \boldsymbol{T}_l(0) = T_{l,0} \tag{5.3}$$

where $T_{w,0}$ is the initial temperature of the cold plate walls, $T_{f,0}$ is the initial temperature of the cold plate fluids, and $T_{l,0}$ is the initial temperature of the tank and LLHX states.

To ensure that each component remains within an upper bound on its operating temperature, we include the following linear inequality path constraints on the temperature states:

$$\boldsymbol{T}_w(t) \leq \boldsymbol{T}_{w,\max}, \quad \boldsymbol{T}_f(t) \leq \boldsymbol{T}_{f,\max}, \quad \boldsymbol{T}_l(t) \leq \boldsymbol{T}_{l,\max} \tag{5.4}$$

where $\boldsymbol{T}_{w,\max} \in \mathbb{R}^{N_c}$ are the maximum allowable temperatures for the CPHX walls, $\boldsymbol{T}_{f,\max} \in \mathbb{R}^{N_c}$ are the maximum allowable temperatures for the CPHX fluids, and $\boldsymbol{T}_{l,\max} \in \mathbb{R}^4$ are the maximum allowable temperatures for the tank and LLHX states.

We also ensure nonnegative flow through each of the valves (i.e, no fluid flow in the reverse direction) with the following linear inequality path constraint:

$$0 \leq \dot{\boldsymbol{m}}_f \tag{5.5}$$

A static form of conservation of mass ensures that the total mass flow rate through all the parallel flows is equal to the mass flow rate through the pump with the following linear equality path constraint:

$$\sum_{i=1}^{N_f} \dot{m}_{f,i}(t) = \dot{m}_{\text{pump}} \tag{5.6}$$

where $\dot{m}_{\text{pump}}$ is the mass flow rate of the pump, assumed to be constant in this thesis.

To model a limit on the rate of change of the valve positions, we also enforce constraints on the derivative of the mass flow rates:

$$|\ddot{\boldsymbol{m}}_f(t)| \leq \ddot{m}_{f,\max} \tag{5.7}$$

where $\ddot{m}_{f,\max}$ is the rate limit.

Finally, we impose a small quadratic penalty term on the controls to both smooth the solution trajectories and improve convergence, modifying Eqn. (5.1) to:

$$\min_{\ddot{\boldsymbol{m}},t_{\text{end}}} \quad -t_{\text{end}} + \lambda \int_0^{t_{\text{end}}} \|\ddot{\boldsymbol{m}}_f(t)\|_2^2 \, dt \tag{5.8}$$

where λ is the penalty parameter. Larger values of λ help regularize the problem, but extremely large values push the solution away from the desired unpenalized value for t_{end}. We ensure that the additional penalty term has a limited overall effect on the objective function value by setting $\lambda \ll 1/(N_f \ddot{m}_{f,\max}^2)$, noting that $\lambda t_{\text{end}} N_f \ddot{m}_{f,\max}^2$ is the maximum value for the penalty term. Therefore, selecting $\lambda = 0.01/(N_f \ddot{m}_{f,\max}^2)$ ensures that the total penalty cost is always at most 1% of the final value for t_{end}.

For the pure series architectures ($N_f = 1$), we developed a simple shooting-based, bisection method that quickly determines the maximum value of t_{end} for each architecture under the given pump mass flow rate.

5.2 Case Studies

Here we present four case studies to demonstrate both the efficacy and utility of the design methodology for cooling system architectures. The nonlinear optimal control problem presented in Section 5.1 was solved using GPOPS-II, which discretizes the problem using pseudospectral methods into a finite-dimensional nonlinear program [88]. The key model and optimization problem parameters used in the case studies are given in Table 5.1.

Table 5.1: Key model and optimization problem parameters.

Parameter	Value
CPHX wall mass	1.15 kg
LLHX wall mass	1.2 kg
Tank fluid mass	2.01 kg
Thermal sink temperature T^t	15 °C
Tank/LLHX initial temperatures, $T_{l,0}$	15 °C
CPHX initial wall temperatures, $T_{w,0}$	20 °C
CPHX initial fluid temperatures, $T_{f,0}$	20 °C
Thermal sink mass flow rate, $\dot{m}_t$	0.2 kg/s
Pump mass flow rate, $\dot{m}_p$	0.4 kg/s
Valve rate limit, $\ddot{\boldsymbol{m}}_{f,\max}$	0.05 kg/s^2
Penalty parameter, λ	$0.01/(N_f \ddot{m}^2_{f,\max})$

5.2.1 Case Study 1

Here we study cooling system architectures that have three CPHXs. As shown in Fig. 4.7 and Section 4.6, there are thirteen unique architectures possible. For these results, we assume that all temperature constraints are equal to 45 °C and that the total heat load on the cooling system is equal to 15 kW.

Identical Heat Loads

The first set of results has an identical heat load to each CPHX, resulting in only three unique architectures. The results are shown in Fig. 5.1. The optimal values for t_{end} were $(133, 129, 123)$ s, for the (pure parallel, hybrid, pure series) architectures, respectively. This result indicates that the pure parallel architecture is the best one under these conditions. Note that in each of the cases, at least one of the temperature constraints is active at the final time (a necessary stopping condition), and for both $1-2-3$ and $1-32$, all the wall temperatures are at their maximum allowable value.

Unique Heat Loads

The next set of results, shown in Fig. 5.2, have a unique and linearly spaced heat load to each CPHX. Here the best architecture is a series topology, 321, with $t_{\text{end}} = 234$ s (in fact, there would only be a minor constraint violation of

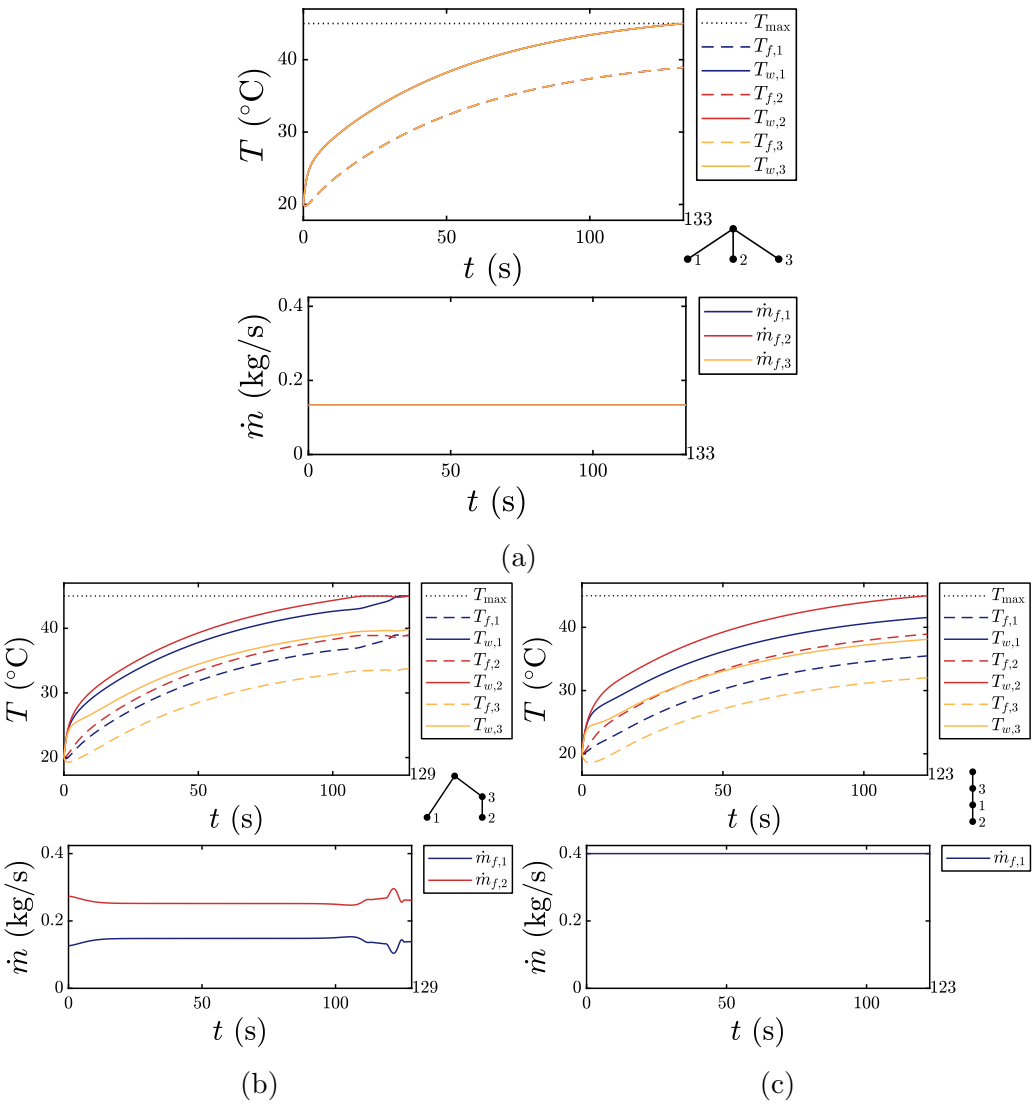

Figure 5.1: Optimal temperature and flow trajectories for the architectures with $\boldsymbol{P}^s = [5, 5, 5]'$ kW and $T_{\max} = 45$ °C: **(a)** $N_f = 3$; **(b)** $N_f = 2$; **(c)** $N_f = 1$.

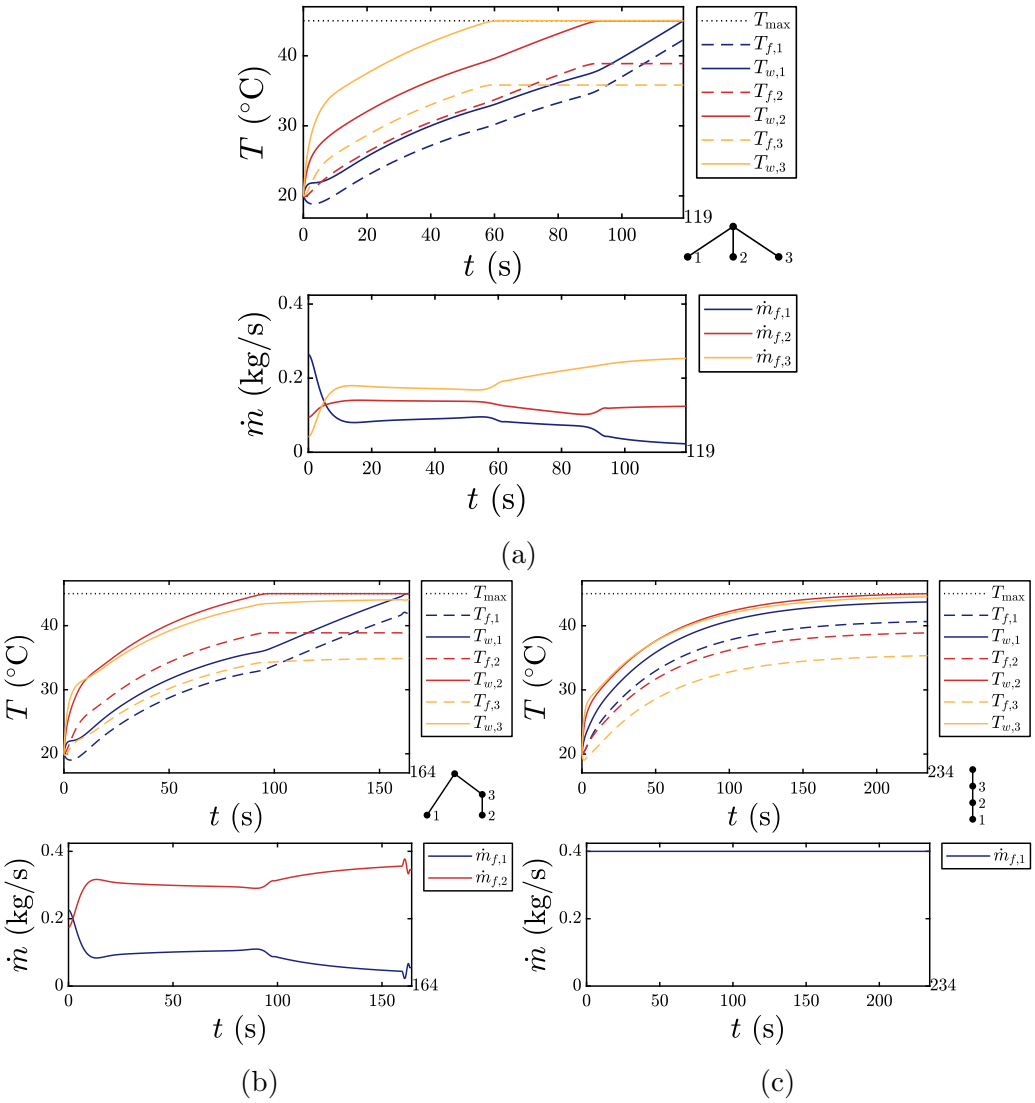

Figure 5.2: Optimal temperature and flow trajectories for the best architectures with $\boldsymbol{P}^s = [2.5, 5, 7.5]'$ kW and $T_{\max} = 45$ °C: **(a)** best architecture with $N_f = 3$ $(1 - 2 - 3)$; **(b)** best architecture with $N_f = 2$ $(1 - 32)$; **(c)** best architecture with $N_f = 1$ (321).

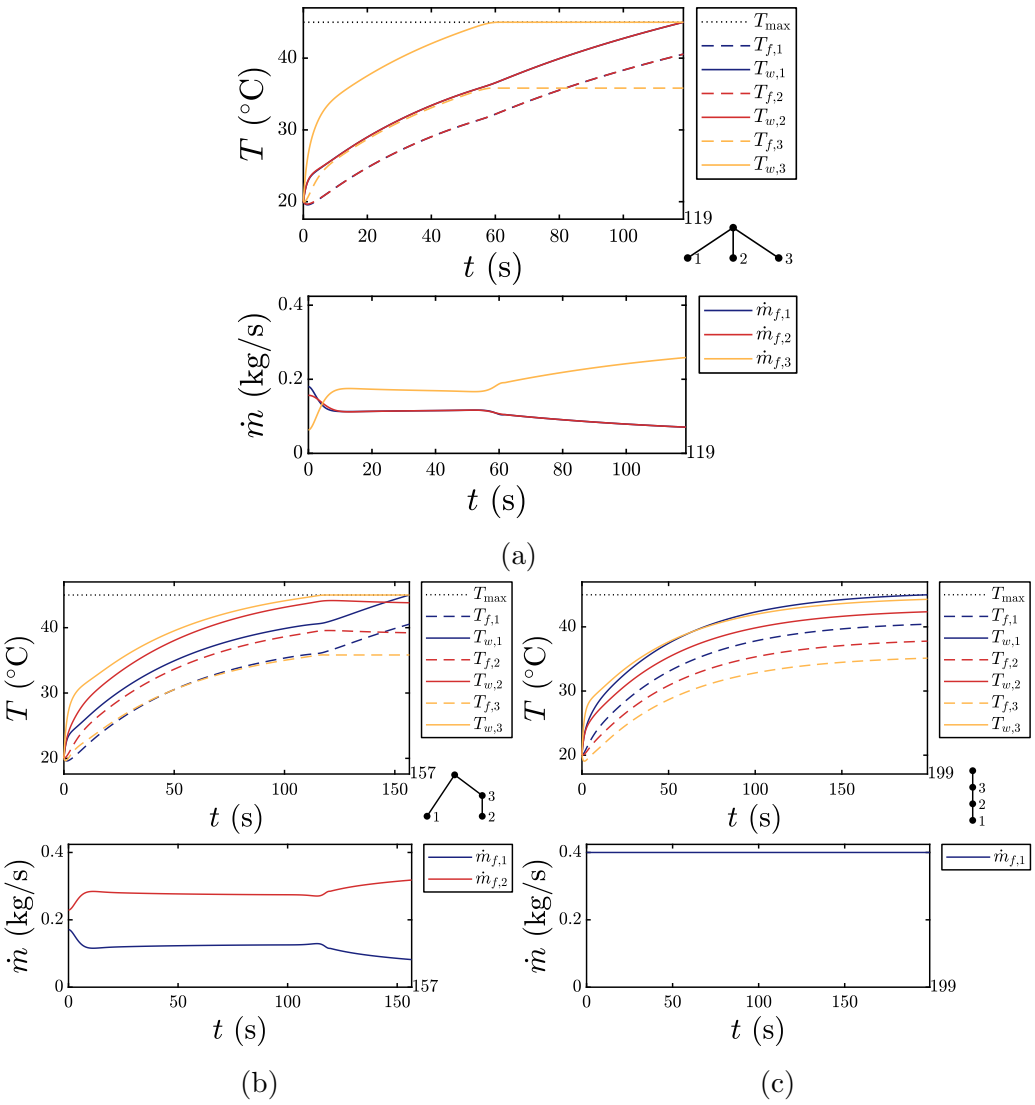

Figure 5.3: Optimal temperature and flow trajectories for the best architectures with $\boldsymbol{P}^s = [3.75, 3.75, 7.5]'$ kW and $T_{\max} = 45$ °C: **(a)** best architecture with $N_f = 3$ $(1-2-3)$; **(b)** best architecture with $N_f = 2$ $(1-32)$; **(c)** best architecture with $N_f = 1$ (321).

0.25 °C were the constraint softened such that the system could reach steady-state). The pure parallel architecture was 7th best overall with $t_{\text{end}} = 119$ s. The worst result was found to be 123, with $t_{\text{end}} = 71$ s. It is observed that the CPHX with the highest heat load (3) should always be connected to the root to achieve good thermal endurance. In addition, many of the solutions have some of the temperature path constraints active for long periods of time (up to 80 s).

Grouped Heat Loads

Here we consider the case when two CPHXs have the same heat load and the third is double the heat load of the first two. The results are shown in Fig. 5.3. Again, the series architectures 321 and 312 (identical models) performed the best with $t_{\text{end}} = 199$ s, while the pure parallel architecture was 5th with $t_{\text{end}} = 119$ s. Comparing these results to those under unique heat loads, we see that the best architecture performs worse with these grouped heat loads than in the unique case, even though the total heat load on the system is the same.

5.2.2 Case Study 2

Unlike in Case Study 1, here we select different values for both the temperature constraints and heat loads among the CPHXs; thus, it is quite challenging to determine through intuition the optimal architecture.

Enumeration with Four CPHXs

For this first result, we consider architectures with four CPHXs and:

$$\boldsymbol{P}^s = [2.5, 6.5, 9.6, 8.7]' \text{ kW}, \quad \boldsymbol{T}_{w,\max} = [47, 59, 41, 53]' \text{ °C}$$

The results for all 73 architectures is summarized in Fig. 5.4. The best architecture was $3 - 421$. This differs from the previous case study, where either pure series or pure parallel was determined to be the best. Observing the trajectories in Fig. 5.5a shows a large amount of constraint activity, with all four wall temperature constraints active at the end. The pure parallel

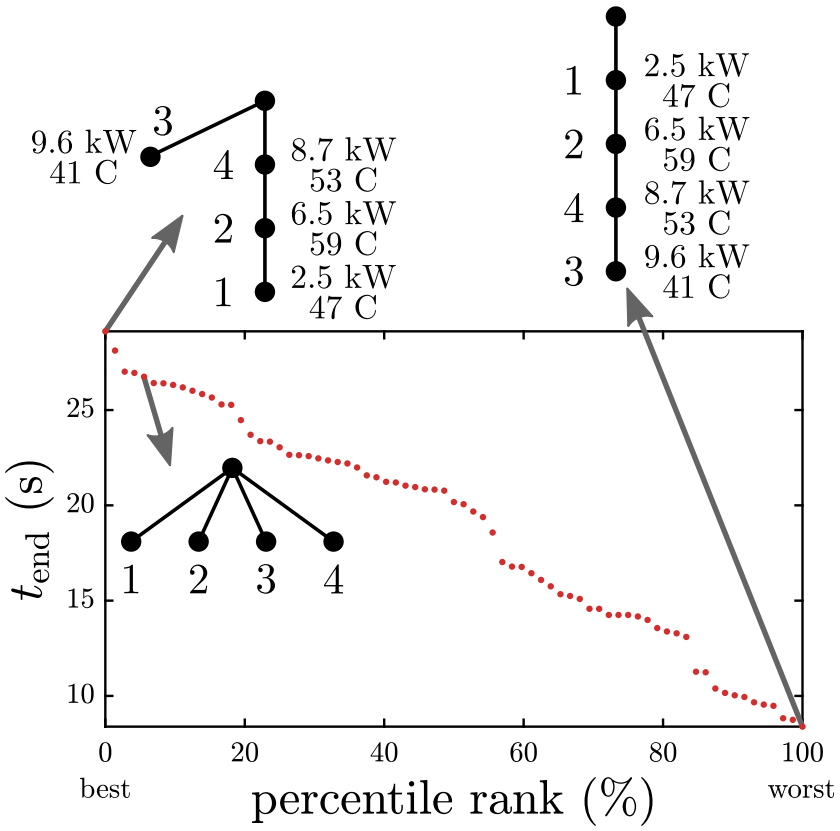

Figure 5.4: Sorted results for all 73 architectures.

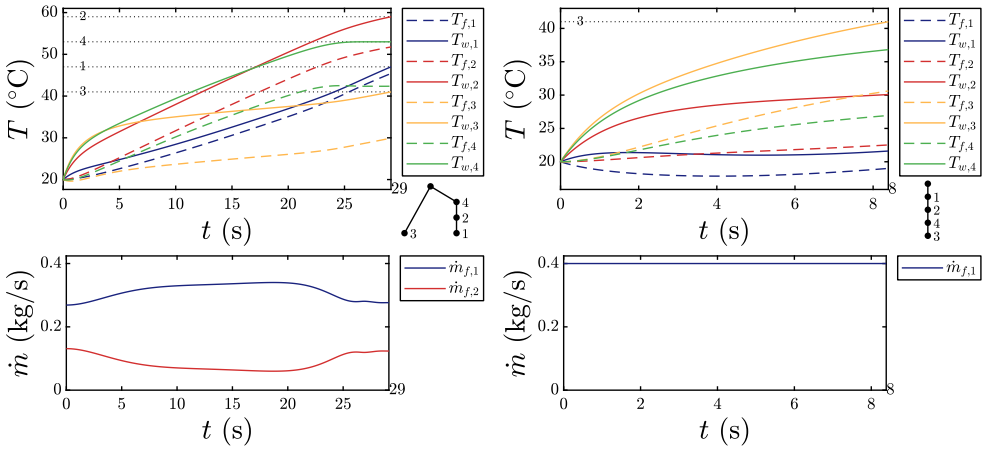

Figure 5.5: Results from Case Study 2 for Enumeration with Four CPHXs: **(a)** best architecture $(3-421)$; **(b)** worst architecture (1243).

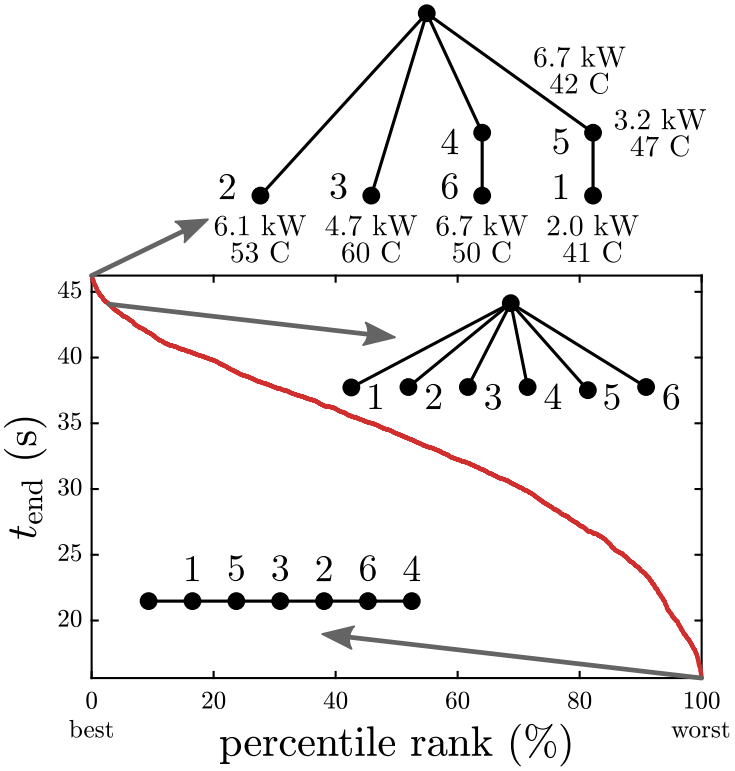

Figure 5.6: Sorted results for all 4051 architectures.

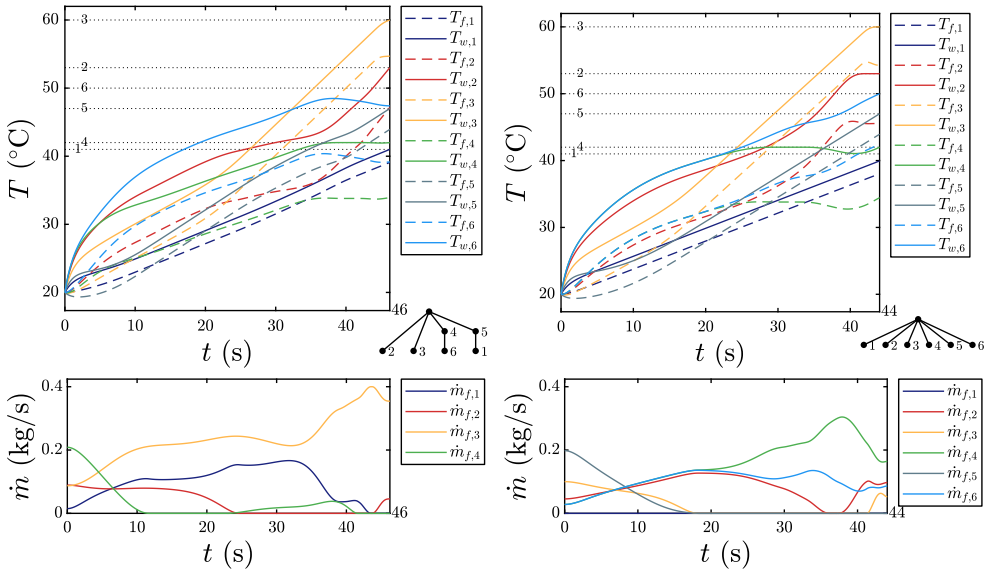

(a) (b)

Figure 5.7: Results from Case Study 2 for Enumeration with Six CPHXs: **(a)** best architecture with $N_f = 3$ $(1 - 36 - 542)$; **(b)** best architecture with $N_f = 4$ $(1 - 5 - 34 - 62)$.

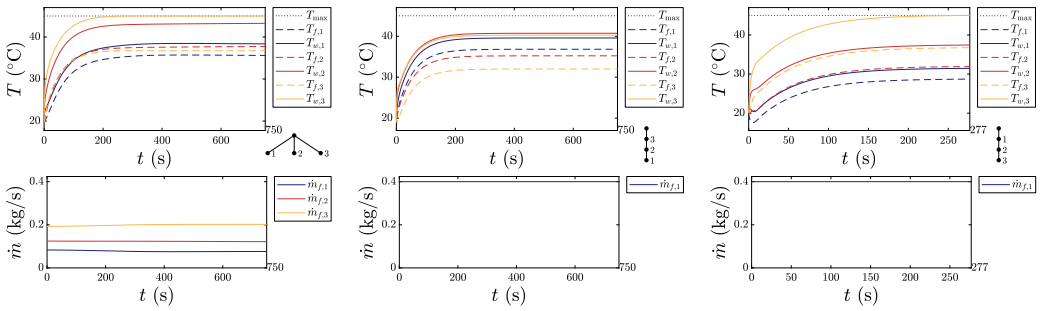

Figure 5.8: Select results for $\boldsymbol{P}^s = [2.25, 4.5, 6.75]$ kW and $T_{\max} = 45$ °C with steady-state solutions: **(a)** feasible architecture with $N_f = 3$ $(1-2-3)$; **(b)** feasible architecture with $N_f = 1$ (321); **(c)** infeasible architecture with least t_{end} (123).

architecture was the 5th best architecture, with marginally shorter thermal endurance than the best (26.8 s vs. 29.1 s).

Enumeration with Six CPHXs

This study is structured similarly to the previous result but with six CPHXs:

$$\boldsymbol{P}^s = [2.0, 6.1, 4.7, 6.7, 3.2, 6.7]' \text{ kW}$$
$$\boldsymbol{T}_{w,\max} = [41, 53, 60, 42, 47, 50]' \text{ °C}$$

The results for all 4051 architectures are summarized in Fig. 5.6. Here, the best architecture was $2-3-46-51$, and had a thermal endurance of 46.2 s. The pure parallel architecture was the 116th best architecture and lasted for 44 s. The temperature and flow rate trajectories for both of these architectures are shown in Figs. 5.7a and 5.7b, respectively. As with the previous result, the solution is not necessarily intuitive. Additionally, since we evaluated all 4051 architectures, we have a large amount of information to aid in choosing the architecture that is the best for the requirements in this case study. For example, patterns with desirable properties can be observed for the problem of interest, which is beyond what is possible when only generating a *single* optimal design. From these results, one clear pattern is improved thermal endurance when CPHX 4 is placed at the root.

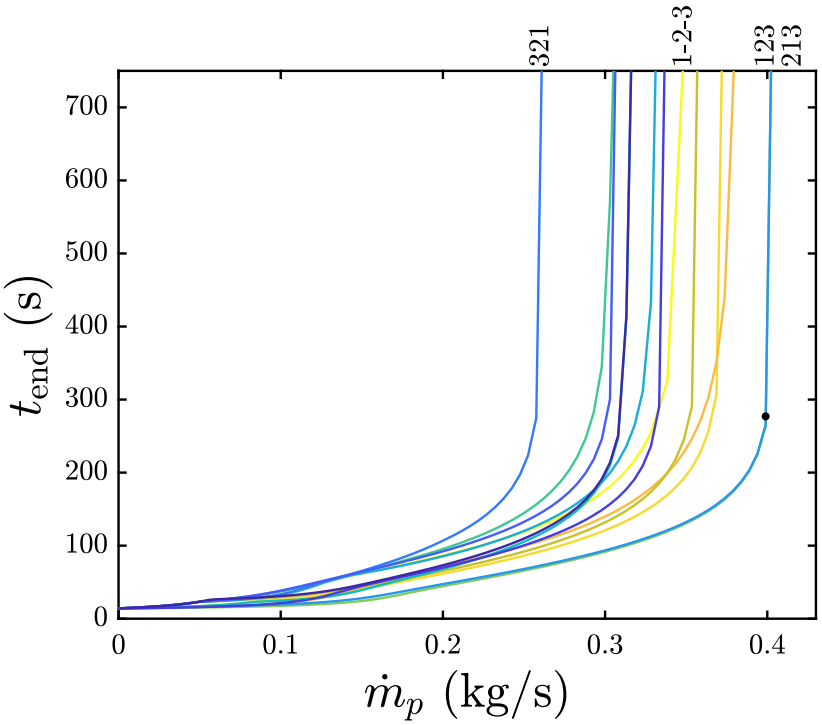

Figure 5.9: Thermal endurance results for $\boldsymbol{P}^s = [2.25, 4.5, 6.75]$ kW and $T_{\max} = 45$ °C with varying values of the pump mass flow rate (select architectures are labeled).

5.2.3 Case Study 3

In the third case study, we consider the goal of determining whether a feasible steady-state operating condition can be reached for a given set of heat loads and temperature constraints. To test this property, we set an upper bound on t_{end} of 1000 s as a conservative estimate of the maximum duration that a feasible architecture could take to reach state-state. Here we used unique and linearly spaced heat loads with $N_c = 3$, similar to Section 5.2.1 except now with a slightly reduced total heat load of 13.5 kW. The results for several of the architectures are shown in Fig. 5.8. Of the 13 candidates, 11 were able to handle the heat loads for 1000 s. The two that were unable to satisfy the conditions were 123 and 213. The remaining candidates with feasible steady-state solutions are distinguished by differing numbers of CPHXs hitting their upper temperature bound. Architecture 321 in Fig. 5.8b had the lowest maximum temperature of 41 °C, so none of the constraints were active. These results demonstrate the sensitivity of thermal endurance with respect to the total heat load, as many architectures with 13.5 kW total heat load can

operate indefinitely, while the best architecture with 15 kW could only last 234 s.

These results suggest several interesting design questions, such as which architecture achieves steady-state behavior with the lowest pump mass flow rate $\dot{m}_p$ (i.e., the smallest pump size), and is there a value for $\dot{m}_p$ such that all the architectures can achieve steady-state behavior? To investigate these questions, a pump sensitivity study was performed using the same conditions as Fig. 5.8. The results of the study are shown in Fig. 5.9 for all thirteen architectures, where each architecture is represented by a distinct curve, and each point on each curve represents maximal t_{end} for a given $\dot{m}_p$ value for the corresponding architecture. The pump flow rates start increasing from zero kg/s, where all architectures have a similar thermal endurance of 14.1 s. For each of the architectures, the thermal endurance increases when the pump flow rate increases. However, the rate of change can be different between the architectures and we can observe that the rankings of the architectures may be different at different flow rates. The pure series architecture (123), shown in Fig. 5.8c, that was infeasible when $\dot{m}_p = 0.4$ kg/s is marked by the black dot in Fig. 5.9. We can observe that only a small increase above 0.4 kg/s is required to achieve indefinite operation as all the architectures exhibit a steep increase in thermal endurance when near the steady-state asymptote. Overall, all the architectures do achieve steady-state behavior around 0.41 kg/s. To minimize the required pump size, the pure series architecture (321) is clearly the best architecture, achieving steady-state behavior with the lowest pump mass flow rate.

5.2.4 Case Study 4

In the final case study, time-varying electronic heat load profiles were considered, unlike the previous case studies with constant profiles. In many applications, the loads are dynamic and cooling system design becomes very challenging and less intuitive. Also, the computational cost is typically higher as compared to the previous studies with constant heat loads due to the more dynamic behavior of the solutions.

Here, three unique trapezoidal pulse profiles, shown in Fig. 5.10, were used with different peak powers and duty cycles. Under these conditions, the pure

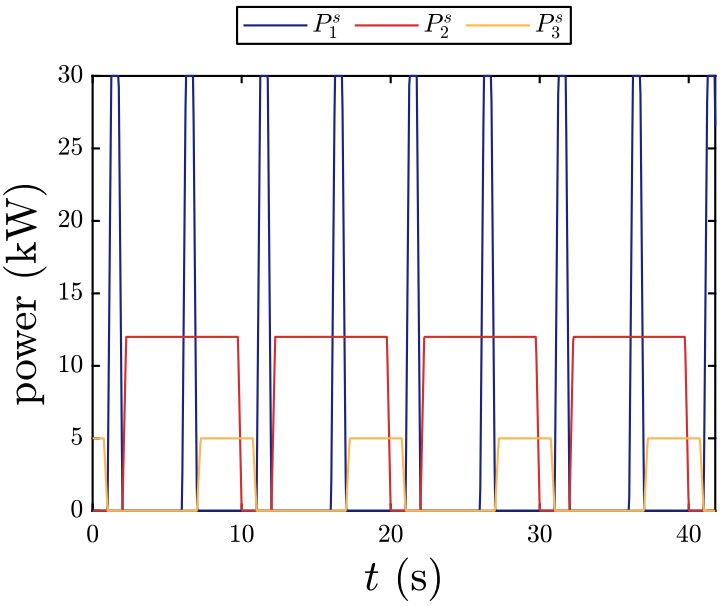

Figure 5.10: Time varying power flows used in this Case Study 4.

parallel architecture $(1-2-3)$ had the maximum thermal endurance of 41.8 s, while the 312 pure series architecture was the worst, lasting for only 27.5 s. The temperature and flow rate trajectories for both of these architectures are shown in Figs. 5.11a and 5.11b, respectively. For the pure parallel architecture, the fluid was dynamically distributed between the two more challenging heat load profiles, P_1^s and P_2^s. For P_3^s, there was no coolant flow across the entire time horizon, demonstrating that under certain conditions, certain components should not be actively cooled in maximizing thermal endurance. At the final point of constraint violation, we observe that the flow was controlled such that just enough cooling was provided to prevent both component 1 and 2 from overheating at different points, but fails in the end due to the control limits. Therefore, it seems that the pure parallel architecture was the best because fluid could be directly diverted to the necessary components.

5.3 Summary of Case Studies

The first case study (Sec. 5.2.1) contains three sub-cases in which a total heat load of 15 kW is divided in different ways among three CPHXs, while

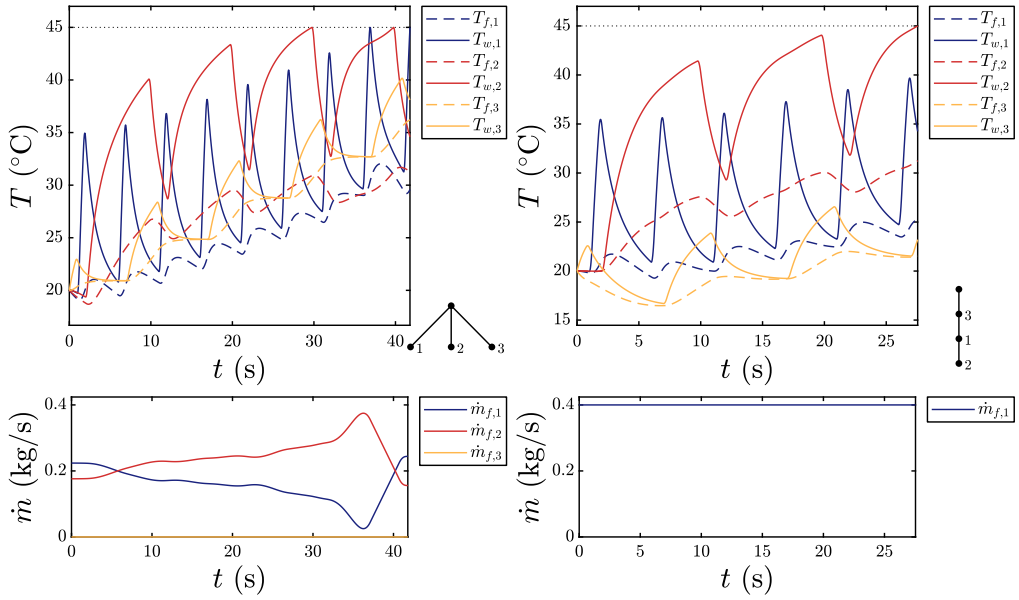

Figure 5.11: Results from Case Study 4 with time-varying power flows:**(a)** best architecture $(1-2-3)$; **(b)** worst architecture (312).

the temperature constraints on each CPHX remain the same throughout the study. In the second case study (Sec. 5.2.2), both the heat loads and the temperature constraints vary among the CPHXs. To determine whether a steady-state feasible operating condition can be reached for a given set of temperature constraints and heat loads, a third case study (Sec. 5.2.3) was performed using three CPHXs. This case study also explores the sensitivity of thermal endurance to pump mass flow rate. Unlike the first three case studies, the fourth case study (Sec. 5.2.4) maximizes thermal endurance subject to time varying load profiles.

CHAPTER 6

CONCLUSION AND FUTURE WORK

6.1 Thesis summary

In this chapter the thesis is summarized in addition to highlighting the main contributions that have been made. A number of future work items that could be done are also outlined.

As mentioned earlier, this thesis involves two main parts: optimal sensor placement and optimal cooling system architecture design. Both sensor placement and cooling methods complement each other in efforts to improve DTM. While the design methods developed in the former were validated on a prototype inverter as a good test case problem, the latter was solved for a candidate single-split and single junction type electro-thermal circuit system.

Optimal sensor placement: An essential component of a dynamic thermal management problem is accurate thermal monitoring. Accuracy of the online estimation of electro-thermal systems depends significantly on the modeling methods used and the optimal sensor placement scheme that supports it. In Chapter 2 of this thesis, many previous optimal sensor placement applications were reviewed, and a clear distinction was made as to how optimal sensor placement in high-density power electronic systems stands as a unique case against previous problems tackled by several researchers in the past. To perform accurate thermal estimation, RC-based lumped-parameter thermal models were used for representing 2D and 3D prototype multi-level inverter power electronic system based on previous work [61]. Novel and computationally-efficient optimal temperature sensor placement methods for active and complex high-density power electronic systems have been presented. A rigorous study of the sensor placement algorithms has been performed and their computational efficiencies have been compared. A

new sensor placement method was introduced based on a continuous relaxation, which was inspired by the SIMP topology optimization method. An important advantage of the relaxation method is improvement in computational efficiency, while admitting much more general performance metrics to be used for sensor placement optimization. A new reformulation based on the trace of the observability Gramian resulted in an LP with dramatically faster solution time, with potential to scale to much larger placement problems. The LP method, however, cannot utilize more general performance metrics. Finally, the design method has been validated experimentally using a highly power dense FCML prototype inverter through dynamic estimation via a continuous-discrete Kalman filter. The temperatures obtained both experimentally and via estimation were in a very close agreement with each other, having errors within 2-3% of the actual experimental values. Thus, not only do the methods developed support accurate dynamic temperature estimation, but also are scalable and applicable to a range of PESs. These advances may help achieve unprecedented performance for thermally-aware power electronic systems that are highly reliable and robust. Future work will incorporate more realistic performance metrics, increased model fidelity, redundant sensor placement techniques, more detailed failure and reliability models, and increased system level design considerations including component layout and cooling system control design.

Enumeration and Design of Optimal Cooling Systems Architectures: To complement the optimal sensor placement problem, efficient cooling system design is necessary. Similar kind of graph based modeling technique has been used to generate candidate architectures relevant to this study. Single-split and single-junction type architectures have been considered as an initial step in order to gain insights on cooling system design. The optimal flow control problem for each candidate architecture has been solved using a commercial software total, GPOPS-II. The optimization formulation is done in a way that all the candidate design architectures possible for a certain case study could be evaluated and sorted according to their thermal endurances. The optimal control problem also provides the flexibility of adding various types of temperature, mass flow rate, and other system-level constraints that one would be interested in. The enumeration could become more computationally challenging as the number of cold plate heat exchangers in the

system goes beyond ten. In that case, more efficient algorithms need to be developed to scale up larger system design problems. Considering that the design method is both scalable to larger problems and flexible enough to incorporate more realistic system level design considerations, such as geometric layout and reliability factors, it could be applied in several real-time applications ranging from low power electronic systems to high end electro-thermal systems. This work serves as a preliminary study toward the design of novel fluid-based thermal management architectures with optimal coolant flow distribution. Candidate cooling system design architectures have been generated using labeled trees and a graph-based dynamic thermal modeling framework. A variable-horizon optimal control problem was posed to identify cooling architectures having maximum thermal endurance. Four case studies were performed that demonstrated the effectiveness and potential of the proposed design methodology. The optimal solutions obtained show that intuition and experience may not be sufficient to identify the best-performing cooling architectures, especially as complexity increases. In particular, this methodology serves as a powerful tool to aid engineers in finding feasible and optimal architectures under different operating conditions. The identified optimal control trajectories can also serve as a basis for the realization of implementable feedback controllers. Finally, this work highlights some of the challenges associated with utilizing enumerative methods in architecture design as well as the automated construction and solving of the corresponding dynamic optimization problems.

6.2 Future Work

The following future work items have been identified that have the potential to improve the design of high density power electronic systems:

- Complete a comprehensive study of sensor location problems with more realistic metrics, integration with control design, and more complete design considerations.
- Further investigation into more comprehensive failure models, including thermo-mechanical modeling of stress and reliability. This is expected

to become increasingly important with integration of new cooling system architectures and increases in system density.

- Develop effective design tools for multi-type sensor placement in both 2D and 3D power electronic systems. Multi-type sensors include stress sensors, flux sensors and current sensors apart from temperature sensors used for this study.

- Cooling system architectures studied here are only limited to a single split and a single junction. Efforts could be made to evaluate more general cooling system architectures having multiple loops, tanks, cooling pumps, etc.

- Further investigation into a more complete physical representation of the cooling system design by incorporating hydraulic models that account for pressure drops across cooling channels.

- In addition, an alternative fixed-horizon optimization problem in which the objective is to minimize violations of soft upper bounds on component temperatures, similar to that used for control in Ref. [86], will be considered.

- To utilize new machine learning techniques to enable solution of much larger synthesis problems with dimension reduction and active learning to support strategic evaluation described in Ref. [102], based on the data obtained via enumeration.

- Lastly, a subset of the best designs identified here will be experimentally validated on a reconfigurable fluid-thermal testbed recently developed as described in Refs. [86, 93].

- One long term goal is to provide engineers design guidelines based on this work to support the development of unprecedented cooling systems that enable future power electronic applications.

APPENDIX A

Supplementary Information for Optimal Sensor Placement

The system dynamics matrix **A**, input **B** matrix and heat generation **u** vector used in optimal sensor placement for the reduced order model are given below:

$$A = \begin{bmatrix} -0.28 & 0.22 & 0.01 & 0.00 & 0.00 & 0.01 & 0.02 & 0.01 & 0.01 \\ 0.22 & -0.28 & 0.01 & 0.01 & 0.02 & 0.01 & 0.00 & 0.00 & 0.01 \\ 0.25 & 0.21 & -0.94 & 0.00 & 0.00 & 0.39 & 0.00 & 0.00 & 0.00 \\ 0.00 & 0.33 & 0.00 & -0.81 & 0.00 & 0.39 & 0.00 & 0.00 & 0.00 \\ 0.00 & 0.46 & 0.00 & 0.00 & -0.94 & 0.39 & 0.00 & 0.00 & 0.00 \\ 0.03 & 0.03 & 0.07 & 0.07 & 0.07 & -0.50 & 0.07 & 0.07 & 0.07 \\ 0.46 & 0.22 & 0.01 & 0.00 & 0.00 & 0.39 & -0.94 & 0.00 & 0.00 \\ 0.33 & 0.22 & 0.01 & 0.00 & 0.00 & 0.39 & 0.00 & -0.81 & 0.00 \\ 0.21 & 0.25 & 0.00 & 0.00 & 0.00 & 0.39 & 0.00 & 0.00 & -0.94 \end{bmatrix}$$

$$B = \begin{bmatrix} 0 & 0 & 0 & 0 & 0 & 0 \\ 0 & 0 & 0 & 0 & 0 & 0 \\ 12.5 & 0 & 0 & 0 & 0 & 0 \\ 0 & 12.5 & 0 & 0 & 0 & 0 \\ 0 & 0 & 12.5 & 0 & 0 & 0 \\ 0 & 0 & 0 & 0 & 0 & 0 \\ 0 & 0 & 0 & 12.5 & 0 & 0 \\ 0 & 0 & 0 & 0 & 12.5 & 0 \\ 0 & 0 & 0 & 0 & 0 & 12.5 \end{bmatrix}$$

$$u = \begin{bmatrix} 1.20 & 1.50 & 1.40 & 0.16 & 0.25 & 0.16 \end{bmatrix}$$

Note: These are just representative matrices for the readers to understand the material presented in the paper. More estimation related information can be found in [61]. The following table A.1 shows the optimal sensor

locations for the full-order 3D model comprising 39 states with the trace of the observability gramian as the performance metric.

Table A.1: Optimal sensor locations for 2D full order model.

Number of sensors	**State Locations**
1	3
2	5,38
3	5,20,22
4	3,4,20,22
5	4,5,20,37,38
6	3,5,22,36,37,38
7	3,4,5,16,20,22,36
8	2,7,13,20,22,29,36,37
9	1,4,13,16,22,29,35-37
10	1,3-5,13,20,22,26,36,37
11	2-5,16,20,22,29,36-38
12	2,5,13,16,19,20,22,26,35-39
13	3-6,13,16,20,22,26,36-39
14	2-5,7,13,20,22,26,29,35-38
15	1-6,13,16,20,22,26,35-38
16	1-6,8,13,19,20,22,35-39
17	1-7,13,16,20,22,26,29,36-39
18	1-5,8,11,13,16,20,22,26,29,35-39
19	1-6,13,16,19,20,22,26,29,31,35-39
20	1-5,7,8,12,16,20,22,23,25,26,29,35-39
21	1-8,12,13,16,20,22-24,26,29,35,37-39
22	1-7,11,13,16,19,20,22,23,26,29,34-39
23	1-8,13,16,19,20,22,23,26,29,31,32,35-39
24	1-8,11-13,16,17,19,20,22,26,29,32,35-39
25	1-7,11,13,16,20-23,25,26,29-32,35-39
26	1-8,11-14,16,19,20,22,23,25,26,2932,35-39
27	1-8,11-13,16,19,20,22-26,29,31,32,35-39
28	1-9,12,13,16,17,19,20,22-26,29,32,34-39
29	1-8,11-13,15,16,19,20,22,23,25,26,29,30,32-39
30	1-8,11-13,16,19-23,25,26,29-39
31	1-8,11-14,16,19,20,22-26,29-39
32	1-8,11-13,15,16,19-32,35-39
33	1-8,11-13,16,18-32,34-39
34	1-9,11-13,15-17,19,20,22-27,29-39
35	1-39 (except 10,15,17,33)

Continued on next page

Table A.1 – continued from previous page

Number of sensors	State Locations
36	1-39 (except 10,15,18)
37	1-39 (except 14 and 17)
38	1-39 (except 10)
39	1-39

The following table A.2 shows the optimal sensor locations for the full-order 3D model comprising 78 states with the trace of the observability gramian as the performance metric. TOG stands for the Trace of the Observability Gramian matrix.

Table A.2: Optimal sensor locations for 3D full order model.

No. of sensors	State Locations	TOG
1	75	0.6733
2	42,75	1.3466
3	44,75,77	2.0198
4	42,44,75,77	2.6931
5	3,40,42,46,75	3.3469
6	40,42,44,46,75,77	4.0275
7	36,40,42,44,46,75,77	4.6935
8	3,5,36,42, 44,46,75,77	5.3583
9	5,38,40-42, 44,46,75,77	6.0219
10	1,3,36,38,40,42,44,46,75,77	6.6892
11	1,3,5,36,38,40,42,44,46,75,77	7.3552
12	1,3,5,36,40,41,42,44,46,74,75,77	8.0139
13	1,3,5,7,36,38,40-42,44,46,75,77	8.6813
14	1,3,5,7,36,38,40-42,44,46,74,75,77	9.3437
15	1,3,5,7,36,38-42,44,46,74,75,77	9.9953
16	1,3,5,7,35,36,38-42,44,74,75,77,78	10.6422
17	1-3,5,7,35,36,38,40-42,44-46,74,77,78	11.2985
18	1-3,5,7,35,36,38,40-42,44-46,74,75,77,78	11.9718
19	1-3,5-7,35,36,38,40-42,44-46,74,75,77,78	12.6128
20	2,3,5-7,35,36,38-46,74,75,77,78	13.24
21	1-3,5-7,35,36,38-46, 74,75,77,78	13.9093
22	1-3,5-7,35,36,38-46, 74-78	14.5434
23	1-7,35,36,38-46, 74-78	15.1671
24	2-7,20,35-46, 74-78	15.6918
25	1-5,7,20, 35-46, 52,74-78	16.2391
26	1-7,20,22, 35-46,74-78	16.9201
27	1-7,20,22, 35-46,71,74-78	17.4693
28	1-7,20,22, 35-46,49,71,74-78	18.0185
29	1-7,20,22, 35-46,49,71,73-78	18.5677
30	1-7,20,22, 35-46,49,52,65,71,73-78	19.1031
31	1-7,20,22, 35-47,49,52,71,73-78	19.6523
32	1-7,20,22, 35-47,49,52,65,71,73-78	20.1876
33	1-7,13,20,35-47,49,52,65,68,71,73-78	20.6895

Continued on next page

Table A.2 – continued from previous page

No. of sensors	State Locations	TOG
34	1-7,16,20,22,35-47,49,55,65,68,71,73-78	21.2542
35	1-7,13,20,22,35-47,49,52,55,65,68,71,73-78	21.7895
36	1-7,13,16,20,22,26,35-47,49,52,55,68,71,73-78	22.3167
37	1-7,13,16,22,26,29,35-47,49,52,55,65,68,71,73-78	22.8186
38	1-8.16,20,22,26,29,35-47,49,52,55,65,68,71,73-78	23.3644
39	1-7,13,16,19,20,22,26,29,35-47,49,52,55,63,65,71,73-78	23.9012
40	1-7,13,16,20,22,26,29,35-47,49,50,55,57,5863,70,71,73-78	24.4135
41	1-7,13,16,19,20,22,23,29,35-47,49,50,52,55,57,68,70,71,73-78	24.9520
42	1-7,13,19,20,22,26,29,35-47,49,50,52,55,57,63,65,68,70,71,73-78	25.4917
43	1-7,13,20,22,23,25,29,35-47,49,52,55,57,58,62,63,65,68,70,71,73-78	26.0049
44	1-7,13,16,19,20,22,26,29,35-47,49, 50,52,55,57,59,63,65,68,70,71,73-78	26.5415
45	1-7,13,16,19,20,22,26,29,35-47,49, 50,52,55,57,59,63,65,68,70,71,73-78	27.0684
46	1-7,13,16,19,20,22,23,26,29,35-47,49,50, 52,55,57,58,62,63,65,68,70,71,73-78	27.5894
47	1-7,13,16,19,20,22-24,26,29,35-47,49,50, 52,55,57,58,62,63,65,68,70,71,73-78	28.1018
48	1-7,13,18-20,22,23,26,29,35-47,49-52, 55,57,58, 62, 63,65,68,70,71,73-78	28.6129
49	1-78, except 9-12,14,15,17,18,21,24,25,27,28, 30-33,48,51,53,54,56,60,64,66,67,69,72	29.1313
50	1-78, except 9-12,14,15,17,18,21,24,25,27,28, 30-34,48,53,54,60,64,66,67,69,72	29.6515
51	1-78, except 8,9,12,14,15,17,18,21,24,25,27,28, 30,31,33,34,48,53,54,60-62,66,67,69,72	30.1660
52	1-78, except 8,9,12,14,15,17,18,21,24,25,27,28,30, 31,33,34,48,53,54,60-62,66,67,69,72	30.6647
53	1-78,except 9,11,12,14,15,17,18,21,24,25,27, 28,30,31,33,34,48,53,54,56,60,66,67,69,72	31.1909
54	1-78, except 8-11,14,15,17,18,21,24,25,27,28,30, 31,33,34,48,53,54,60,66,67,69	31.6724
55	1-78, except 8,9,11,14,15,17,18,21,24, 25,27,28,30-33,48,53,54,60,66,67,72	32.2176
56	1-78, except 9,11,14,15,17,18,21,24, 27,28,30,31,33,34,48,51,53,54,60,66,67,72	32.7289
57	1-78, except 9,11,14,15,17,21,24,25,27, 28,30,31,33,34,48,53,54,60,66,67,72	33.2425
58	1-78, except 9,12,14,15,17,18,21,25,27,28,30,31,33,48,53,54,60,66,67,72	33.7549
59	1-78, except 9,12,14,15,17,21,25,27,28,30,31,33,48,53,54,60,66,67,72	34.2675
60	1-78, except 9,12,14,15,17,21,25,27,28,31,33,48,53,54,60,66,67,72	34.7797
61	1-78, except 9,12,14,15,21,25,27,28,30,33,48,53,54,60,66,67,72	35.2921
62	1-78, except 9,14,15,17,21,27,28,30,33,48,53,54,60,66,67,72	35.8044
63	1-78, except 9,14,15,21,27,28,30,33,48,53,54,60,66,67,72	36.3166
64	1-78, except 14,15,21,25,27,28,33,48,53,54,60,66,67,72	36.7524
65	1-78, except 9,14,15,21,27,28,33,53,54,60,66,67,72	37.3096
66	1-78, except 9,15,21,27,28,33,53,54,60,66,67,72	37.7452
67	1-78, except 9,14,15,21,27,28,33,53,54,60,67	38.2310
68	1-78, except 9,14,15,21,27,28,33,60,66,67	38.6717
69	1-78, except 9,14,15,21,27,28,33,60,67	39.1125

Continued on next page

Table A.2 – continued from previous page

No. of sensors	State Locations	TOG
70	1-78, except 9,14,15,21,27,33,60,67	39.5841
71	1-78, except 9,14,15,27,28,33,60	39.9924
72	1-78, except 9,15,27,28,33,60	40.4280
73	1-78, except 9,15,27,28,33	40.8642
74	1-78, except 14,15,27,28	41.3001
75	1-78, except 14,15,28	41.7357
76	1-78, except 14,15	42.1713
77	1-78, except 15	42.6069
78	1-78	43.0425

REFERENCES

[1] C. Pornet and A. Isikveren, "Conceptual design of hybrid-electric transport aircraft," *Progress in Aerospace Sciences*, vol. 79, pp. 114 – 135, 2015. [Online]. Available: http://www.sciencedirect.com/science/article/pii/S0376042115300130

[2] M. Sinnett, "787 no-bleed systems: saving fuel and enhancing operational efficiencies," *Boeing Aero Mag.*, vol. 4, pp. 6–11, 2007.

[3] P. J. Tannous, "Dynamic temperature estimation of power electronics systems," *Masters thesis, University of Illinois at Urbana Champaign*, 2017, http://hdl.handle.net/2142/98135.

[4] J. G. Kassakian and T. M. Jahns, "Evolving and emerging applications of power electronics in systems," *IEEE Journal of Emerging and Selected Topics in Power Electronics*, vol. 1, no. 2, pp. 47–58, June 2013, doi:10.1109/JESTPE.2013.2271111.

[5] B. Lequesne, "Automotive electrification: The nonhybrid story," *IEEE Transactions on Transportation Electrification*, vol. 1, no. 1, pp. 40–53, June 2015, doi:10.1109/TTE.2015.2426573.

[6] B. Bilgin, P. Magne, P. Malysz, Y. Yang, V. Pantelic, M. Preindl, A. Korobkine, W. Jiang, M. Lawford, and A. Emadi, "Making the case for electrified transportation," *IEEE Transactions on Transportation Electrification*, vol. 1, no. 1, pp. 4–17, June 2015.

[7] B. Sarlioglu and C. T. Morris, "More electric aircraft: Review, challenges, and opportunities for commercial transport aircraft," *IEEE Transactions on Transportation Electrification*, vol. 1, no. 1, pp. 54–64, June 2015.

[8] M. Marz, "Thermal management in high-density power converters," in *IEEE International Conference on Industrial Technology, 2003*, vol. 2, Dec 2003, doi:10.1109/ICIT.2003.1290835. pp. 1196–1201 Vol.2.

[9] A. Livshitz, B. H. Chudnovsky, B. Bukengolts, and B. A. Chudnovsky, "On-line temperature monitoring of power distribution equipment," in *Record of Conference Papers Industry Applications Society 52nd Annual Petroleum and Chemical Industry Conference*, Sept 2005, doi:10.1109/PCICON.2005.1524558. pp. 223–231.

[10] W. J. Staszewski and K. Worden, "Overview of optimal sensor location methods for damage detection," *Proc. SPIE*, vol. 4326, pp. 179–187, 2001, doi:10.1117/12.436472. [Online]. Available: http://dx.doi.org/10.1117/12.436472

[11] S. Beygzadeh, E. Salajegheh, P. Torkzadeh, J. Salajegheh, and S. S. Naseralavi, "An improved genetic algorithm for optimal sensor placement in space structures damage detection." *International Journal of Space Structures*, vol. 29, no. 3, pp. 121 – 136, 2014, doi:https://doi.org/10.1260/0266-3511.29.3.121.

[12] Z.Guo, K. Kim, G. Lanzara, N. Salowitz, P. Peumans, and F. K. Chang, "Micro-fabricated, expandable temperature sensor network for macro-scale deployment in composite structures," in *2011 Aerospace Conference*, March 2011, doi:10.1109/AERO.2011.5747597. pp. 1–6.

[13] T. Yi, H. Li, and M. Gu, "Optimal sensor placement for structural health monitoring based on multiple optimization strategies," *The Structural Design of Tall and Special Buildings*, vol. 20, no. 7, pp. 881–900, 2011, doi:10.1002/tal.712. [Online]. Available: http://dx.doi.org/10.1002/tal.712

[14] C. He, J. Xing, J. Li, Q. Yang, R. Wang, and X. Zhang, "A combined optimal sensor placement strategy for the structural health monitoring of bridge structures," *International Journal of Distributed Sensor Networks*, vol. 9, no. 11, p. 820694, 2013, doi:10.1155/2013/820694. [Online]. Available: http://dx.doi.org/10.1155/2013/820694

[15] E. M. Hernandez, "Efficient sensor placement for state estimation in structural dynamics," *Mechanical Systems and Signal Processing*, vol. 85, pp. 789 – 800, 2017, doi:10.1016/j.ymssp.2016.09.005. [Online]. Available: http://www.sciencedirect.com/science/article/pii/S0888327016303442

[16] M. Z. A. Bhuiyan, G. Wang, J. Cao, and J. Wu, "Sensor placement with multiple objectives for structural health monitoring," *ACM Trans. Sen. Netw.*, vol. 10, no. 4, pp. 68:1–68:45, June 2014, doi:10.1145/2533669. [Online]. Available: http://doi.acm.org/10.1145/2533669

[17] S. L. Zhan, J. Y. Lai, and F. Huang, "Optimal sensor placement for high-rise building via genetic algorithms and improved information matrix criterion," in *Advances in Civil Engineering and Architecture Innovation*, ser. Advanced Materials Research, vol. 368. Trans Tech Publications, 1 2012, doi:10.4028/www.scientific.net/AMR.368-373.1653. pp. 1653–1659.

[18] M. Meo and G. Zumpano, "On the optimal sensor placement techniques for a bridge structure," *Engineering Structures*, vol. 27, no. 10, pp. 1488 – 1497, 2005, doi:10.1016/j.engstruct.2005.03.015. [Online]. Available: //www.sciencedirect.com/science/article/pii/S014102960500146X

[19] V. Gupta, M. Sharma, and N. Thakur, "Optimization criteria for optimal placement of piezoelectric sensors and actuators on a smart structure: A technical review," *Journal of Intelligent Material Systems and Structures*, vol. 21, no. 12, pp. 1227–1243, 2010, doi:10.1177/1045389X10381659. [Online]. Available: http://dx.doi.org/10.1177/1045389X10381659

[20] K. R. Kumar and S. Narayanan, "The optimal location of piezoelectric actuators and sensors for vibration control of plates," *Smart Materials and Structures*, vol. 16, no. 6, p. 2680, 2007, http://stacks.iop.org/0964-1726/16/i=6/a=073. [Online]. Available: http://stacks.iop.org/0964-1726/16/i=6/a=073

[21] J. A. Burns, J. Borggaard, E. Cliff, and L. Zietsman, "An optimal control approach to sensor actuator placement for optimal control of high performance buildings," in *International High Performance Buildings Conference*, Paper 76 2012, https://docs.lib.purdue.edu/ihpbc/76/.

[22] M. Papadopoulou, B. Raphael, I. F. Smith, and C. Sekhar, "Optimal Sensor Placement for Time-Dependent Systems: Application to Wind Studies around Buildings," *Journal of Computing in Civil Engineering*, vol. 30, no. 2, p. 04015024, Mar. 2016, doi:10.1061/(ASCE)CP.1943-5487.0000497.

[23] X. Wu, M. Liu, and Y. Wu, "In-situ soil moisture sensing: Optimal sensor placement and field estimation," *ACM Trans. Sen. Netw.*, vol. 8, no. 4, pp. 33:1–33:30, sep 2012, doi:10.1145/2240116.2240122. [Online]. Available: http://doi.acm.org/10.1145/2240116.2240122

[24] S. K. Seelan, S. Laguette, G. M. Casady, and G. A. Seielstad, "Remote sensing applications for precision agriculture: A learning community approach," *Remote Sensing of Environment*, vol. 88, no. 12, pp. 157 – 169, 2003, doi:10.1016/j.rse.2003.04.007. [Online]. Available: //www.sciencedirect.com/science/article/pii/S0034425703002360

[25] D. Anurag, S. Roy, and S. Bandyopadhyay, "Agro-sense: Precision agriculture using sensor-based wireless mesh networks," in *2008 First ITU-T Kaleidoscope Academic Conference - Innovations in NGN: Future Network and Services*, May 2008, doi:10.1109/KINGN.2008.4542291. pp. 383–388.

[26] W. Du, Z. Xing, M. Li, B. He, L. H. C. Chua, and H. Miao, "Optimal sensor placement and measurement of wind for water quality studies in urban reservoirs," in *Proceedings of the 13th International Symposium on Information Processing in Sensor Networks*, ser. IPSN '14. Piscataway, NJ, USA: IEEE Press, 2014, http://dl.acm.org/citation.cfm?id=2602339.2602358. [Online]. Available: http://dl.acm.org/citation.cfm?id=2602339.2602358 pp. 167–178.

[27] F. Nejjari, R. Sarrate, and J. Blesa, "Optimal pressure sensor placement in water distribution networks minimizing leak location uncertainty," *Procedia Engineering*, vol. 119, pp. 953 – 962, 2015, doi:10.1016/j.proeng.2015.08.979. [Online]. Available: http://www.sciencedirect.com/science/article/pii/S1877705815026491

[28] M. V. Casillas, V. Puig, L. E. Garza-Castan, and A. Rosich, "Optimal sensor placement for leak location in water distribution networks using genetic algorithms," in *2013 Conference on Control and Fault-Tolerant Systems (SysTol)*, Oct 2013, doi:10.1109/SysTol.2013.6693876. pp. 61–66.

[29] M. V. Casillas, L. E. Garza-Castan, and V. Puig, "Optimal sensor placement for leak location in water distribution networks using evolutionary algorithms," *Water*, vol. 7, no. 11, pp. 6496–6515, 2015, doi:10.3390/w7116496. [Online]. Available: http://www.mdpi.com/2073-4441/7/11/6496

[30] N. A. Samad, J. B. Siegel, A. G. Stefanopoulou, and A. Knobloch, "Observability analysis for surface sensor location in encased battery cells," in *2015 American Control Conference (ACC)*, July 2015, doi:10.1109/ACC.2015.7170752. pp. 299–304.

[31] C. Sumana and C. Venkateswarlu, "Optimal selection of sensors for state estimation in a reactive distillation process," *Journal of Process Control*, vol. 19, no. 6, pp. 1024 – 1035, 2009, doi:10.1016/j.jprocont.2009.01.003. [Online]. Available: http://www.sciencedirect.com/science/article/pii/S0959152409000080

[32] D. Georges, "The use of observability and controllability gramians or functions for optimal sensor and actuator location in finite-dimensional systems," in *Proceedings of 1995 34th IEEE Conference on Decision and Control*, vol. 4, Dec 1995, doi:10.1109/CDC.1995.478999. pp. 3319–3324 vol.4.

[33] A. K. Singh and J. Hahn, "Determining Optimal Sensor Locations for State and Parameter Estimation for Stable Nonlinear Systems," *Industrial & Engineering Chemistry Research*, vol. 44, no. 15, pp. 5645–5659, 2005, doi:10.1021/ie040212v. [Online]. Available: http://dx.doi.org/10.1021/ie040212v

[34] A. K. Singh and J. Hahn, "On the use of empirical gramians for controllability and observability analysis," in *Proceedings of the 2005, American Control Conference, 2005.*, June 2005, doi:10.1109/ACC.2005.1469922. pp. 140–146.

[35] A. K. Singh and J. Hahn, "Determining optimal sensor locations for state and parameter estimation for stable nonlinear systems," *Industrial & Engineering Chemistry Research*, vol. 44, no. 15, pp. 5645–5659, 2005, doi:10.1021/ie040212v. [Online]. Available: http://dx.doi.org/10.1021/ie040212v

[36] A. K. Singh and J. Hahn, "Determining optimal sensor locations for state and parameter estimation for stable nonlinear systems," *Industrial & Engineering Chemistry Research*, vol. 44, no. 15, pp. 5645–5659, 2005, doi:10.1021/ie040212v. [Online]. Available: http://dx.doi.org/10.1021/ie040212v

[37] F. van den Berg, H. Hoefsloot, H. Boelens, and A. Smilde, "Selection of optimal sensor position in a tubular reactor using robust degree of observability criteria," *Chemical Engineering Science*, vol. 55, no. 4, pp. 827 – 837, 2000, doi:10.1016/S0009-2509(99)00360-7. [Online]. Available: //www.sciencedirect.com/science/article/pii/S0009250999003607

[38] R. Mushini and D. Simon, "On optimization of sensor selection for aircraft gas turbine engines," in *18th International Conference on Systems Engineering (ICSEng'05)*, Aug 2005, doi:10.1109/ICSENG.2005.61. pp. 9–14.

[39] F. Zenatti, D. Fontanelli, L. Palopoli, D. Macii, and P. Nazemzadeh, "Optimal placement of passive sensors for robot localisation," in *IEEE International Conference on Intelligent Robots and Systems*, vol. 2016-November, 2016, doi:10.1109/IROS.2016.7759675. [Online]. Available: https://www.scopus.com/inward/record.uri?eid=2-s2.0-85006384949&doi=10.1109 pp. 4586–4593.

[40] F. Arrichiello, G. Antonelli, A. P. Aguiar, and A. Pascoal, "An observability metric for underwater vehicle localization using range measurements," *Sensors*, vol. 13, no. 12, pp. 16 191–16 215, 2013, doi:10.3390/s131216191. [Online]. Available: http://www.mdpi.com/1424-8220/13/12/16191

[41] S. Martnez and F. Bullo, "Optimal sensor placement and motion coordination for target tracking," *Automatica*, vol. 42, no. 4, pp. 661 – 668, 2006. [Online]. Available: http://www.sciencedirect.com/science/article/pii/S000510980600015X

[42] X. Wang, G. Xing, J. Chen, C. X. Lin, and Y. Chen, "Towards optimal sensor placement for hot server detection in data centers," in *2011 31st International Conference on Distributed Computing Systems*, June 2011, doi:10.1109/ICDCS.2011.20. pp. 899–908.

[43] E. Lovisari, C. C. de Wit, and A. Y. Kibangou, "Optimal sensor placement in road transportation networks using virtual variances," in *2015 54th IEEE Conference on Decision and Control (CDC)*, Dec 2015, doi:10.1109/CDC.2015.7402638. pp. 2786–2791.

[44] A. Mainwaring, D. Culler, J. Polastre, R. Szewczyk, and J. Anderson, "Wireless sensor networks for habitat monitoring," in *Proceedings of the 1st ACM International Workshop on Wireless Sensor Networks and Applications*, ser. WSNA '02. New York, NY, USA: ACM, 2002, doi:10.1145/570738.570751. [Online]. Available: http://doi.acm.org/10.1145/570738.570751 pp. 88–97.

[45] Y. Zhang and A. Srivastava, "Accurate temperature estimation using noisy thermal sensors for gaussian and non-gaussian cases," *IEEE Transactions on Very Large Scale Integration (VLSI) Systems*, vol. 19, no. 9, pp. 1617–1626, Sept 2011, doi:10.1109/TVLSI.2010.2051567.

[46] A. N. Nowroz, R. Cochran, and S. Reda, "Thermal monitoring of real processors: Techniques for sensor allocation and full characterization," in *Design Automation Conference*, June 2010, doi:10.1145/1837274.1837291. pp. 56–61.

[47] Q. Li, T. Cui, Y. Weng, R. Negi, F. Franchetti, and M. D. Ilic, "An information-theoretic approach to pmu placement in electric power systems," *IEEE Transactions on Smart Grid*, vol. 4, no. 1, pp. 446–456, March 2013, doi:10.1109/TSG.2012.2228242.

[48] K.-J. Lee, K. Skadron, and W. Huang, "Analytical model for sensor placement on microprocessors," in *2005 International Conference on Computer Design*, Oct 2005, doi:10.1109/ICCD.2005.23. pp. 24–27.

[49] S. O. Memik, R. Mukherjee, M. Ni, and J. Long, "Optimizing thermal sensor allocation for microprocessors," *IEEE Transactions on Computer-Aided Design of Integrated Circuits and Systems*, vol. 27, no. 3, pp. 516–527, March 2008, doi:10.1109/TCAD.2008.915538.

[50] X. Li, W. Jiang, and W. Zhou, "Optimising thermal sensor placement and thermal maps reconstruction for microprocessors using simulated annealing algorithm based on pca," *IET Circuits, Devices Systems*, vol. 10, no. 6, pp. 463–472, 2016, doi:10.1049/iet-cds.2016.0201.

[51] F. Zanini, D. Atienza, and G. D. Micheli, "A combined sensor placement and convex optimization approach for thermal management in 3d-mpsoc with liquid cooling," *Integration, the {VLSI} Journal*, vol. 46, no. 1, pp. 33 – 43, 2013, doi:10.1016/j.vlsi.2011.12.003. [Online]. Available: http://www.sciencedirect.com/science/article/pii/S016792601100109X

[52] H. Wang, S. X. D. Tan, S. Swarup, and X. X. Liu, "A power-driven thermal sensor placement algorithm for dynamic thermal management," in *2013 Design, Automation Test in Europe Conference Exhibition (DATE)*, March 2013, doi:10.7873/DATE.2013.252. pp. 1215–1220.

[53] H. Zhou, X. Li, C. Y. Cher, E. Kursun, H. Qian, and S. C. Yao, "An information-theoretic framework for optimal temperature sensor allocation and full-chip thermal monitoring," in *DAC Design Automation Conference 2012*, June 2012, https://ieeexplore.ieee.org/document/6241574/. pp. 642–647.

[54] Y. Zhang and A. Srivastava, "Adaptive and autonomous thermal tracking for high performance computing systems," in *Proceedings of the 47th Design Automation Conference*, ser. DAC '10. New York, NY, USA: ACM, 2010, doi:10.1145/1837274.1837293. [Online]. Available: http://doi.acm.org/10.1145/1837274.1837293 pp. 68–73.

[55] J. Liu and A. Terzis, "Sensing data centres for energy efficiency," *Philosophical Transactions of the Royal Society of London A: Mathematical, Physical and Engineering Sciences*, vol. 370, no. 1958, pp. 136–157, 2011, doi:10.1098/rsta.2011.0245. [Online]. Available: http://rsta.royalsocietypublishing.org/content/370/1958/136

[56] S. Sarma, N. Dutt, P. Gupta, N. Venkatasubramanian, and A. Nicolau, "Cyberphysical-system-on-chip (cpsoc): A self-aware mpsoc paradigm with cross-layer virtual sensing and actuation," in *2015 Design, Automation Test in Europe Conference Exhibition (DATE)*, March 2015, pp. 625–628.

[57] S. c. Lin and K. Banerjee, "An electrothermally-aware full-chip substrate temperature gradient evaluation methodology for leakage dominant technologies with implications for power estimation and hot-spot management," in *2006 IEEE/ACM International Conference on Computer Aided Design*, Nov 2006, doi:10.1109/ICCAD.2006.320176. pp. 568–574.

[58] X. Li, M. Rong, R. Wang, T. Liu, and L. Zhou, "Reducing the number of sensors under hot spot temperature error bound for microprocessors based on dual clustering," *IET Circuits, Devices Systems*, vol. 7, no. 4, pp. 211–220, July 2013, doi:10.1049/iet-cds.2012.0314.

[59] S. Lu, R. Tessier, and W. Burleson, "Collaborative calibration of on-chip thermal sensors using performance counters," in *2012 IEEE/ACM International Conference on Computer-Aided Design (ICCAD)*, Nov 2012, https://ieeexplore.ieee.org/document/6386583/. pp. 15–22.

[60] Y. Zhang, A. Srivastava, and M. Zahran, "Chip level thermal profile estimation using on-chip temperature sensors," in *2008 IEEE International Conference on Computer Design*, Oct 2008, pp. 432–437.

[61] P. J. Tannous, S. R. T. Peddada, J. T. Allison, T. Foulkes, R. C. N. Pilawa-Podgurski, and A. G. Alleyne, "Dynamic temperature estimation of power electronics systems," in *2017 American Control Conference (ACC)*, May 2017, doi:10.23919/ACC.2017.7963482. pp. 3463–3469.

[62] H. Sun and O. Bykztrk, "Optimal sensor placement in structural health monitoring using discrete optimization," *Smart Materials and Structures*, vol. 24, no. 12, p. 125034, 2015, doi:10.1088/0964-1726/24/12/125034. [Online]. Available: http://stacks.iop.org/0964-1726/24/i=12/a=125034

[63] M. I. Friswell and R. Castro-Triguero, "Clustering of sensor locations using the effective independence method," *AIAA Journal*, vol. 53, no. 5, pp. 1388–1391, Mar. 2015, doi:10.2514/1.J053503. [Online]. Available: https://doi.org/10.2514/1.J053503

[64] D. A. N. I. E. L. C. KAMMER, "Sensor placement for on-orbit modal identification and correlation of large space structures," *Journal of Guidance, Control, and Dynamics*, vol. 14, no. 2, pp. 251–259, Mar. 1991, doi:10.2514/3.20635. [Online]. Available: https://doi.org/10.2514/3.20635

[65] Y. Lei, C. Barth, S. Qin, W. C. Liu, I. Moon, A. Stillwell, D. Chou, T. F. Z. Ye, Z. Liao, and R. Pilawa-Podgurski, "A 2 kW, Single-Phase, 7-Level Flying Capacitor Multilevel Inverter with an Active Energy Buffer," *IEEE Transactions on Power Electronics*, 2017, doi:10.1109/TPEL.2017.2650140.

[66] V. Tzoumas, A. Jadbabaie, and G. J. Pappas, "Sensor placement for optimal kalman filtering: Fundamental limits, submodularity, and algorithms," in *2016 American Control Conference (ACC)*, July 2016, doi:10.1109/ACC.2016.7524914. pp. 191–196.

[67] K. Deng, S. Goyal, P. Barooah, and P. G. Mehta, "Structure-preserving model reduction of nonlinear building thermal models," *Automatica*, vol. 50, no. 4, pp. 1188 – 1195, 2014, doi:10.1016/j.automatica.2014.02.009. [Online]. Available: http://www.sciencedirect.com/science/article/pii/S0005109814000478

[68] K. Skadron, T. Abdelzaher, and M. R. Stan, "Control-theoretic techniques and thermal-rc modeling for accurate and localized dynamic thermal management," in *Proceedings of the 8th International Symposium on High-Performance Computer Architecture*, ser. HPCA '02. Washington, DC, USA: IEEE Computer Society, 2002, http://dl.acm.org/citation.cfm?id=874076.876476. [Online]. Available: http://dl.acm.org/citation.cfm?id=874076.876476 pp. 17–.

[69] P. Mller and H. Weber, "Analysis and optimization of certain qualities of controllability and observability for linear dynamical systems," *Automatica*, vol. 8, no. 3, pp. 237 – 246, 1972, doi:10.1016/0005-1098(72)90044-1. [Online]. Available: http://www.sciencedirect.com/science/article/pii/0005109872900441

[70] A. K. Singh and J. Hahn, "State estimation for high-dimensional chemical processes," *Computers and Chemical Engineering*, vol. 29, no. 1112, pp. 2326 – 2334, 2005, doi:10.1016/j.compchemeng.2005.05.009. [Online]. Available: http://www.sciencedirect.com/science/article/pii/S009813540500150X

[71] J. Wilson and S. Guhe, "Observability matrix condition number in design of measurement strategies," in *European Symposium on Computer-Aided Process Engineering-15, 38th European Symposium of the Working Party on Computer Aided Process Engineering*, ser. Computer Aided Chemical Engineering, L. Puigjaner and A. Espua, Eds. Elsevier, 2005, vol. 20, pp. 397 – 402, doi:10.1016/S1570-7946(05)80188-9. [Online]. Available: http://www.sciencedirect.com/science/article/pii/S1570794605801889

[72] R. Kannan and C. L. Monma, "On the computational complexity of integer programming problems," in *Optimization and Operations Research*, R. Henn, B. Korte, and W. Oettli, Eds. Berlin, Heidelberg: Springer Berlin Heidelberg, 1978, pp. 161–172.

[73] A. M. Newman and M. Weiss, "A survey of linear and mixed-integer optimization tutorials," *INFORMS Transactions on Education*, vol. 14, no. 1, pp. 26–38, 2013, doi:10.1287/ited.2013.0115. [Online]. Available: https://doi.org/10.1287/ited.2013.0115

[74] S. Joshi and S. Boyd, "Sensor selection via convex optimization," *Trans. Sig. Proc.*, vol. 57, no. 2, pp. 451–462, Feb. 2009, doi:10.1109/TSP.2008.2007095. [Online]. Available: http://dx.doi.org/10.1109/TSP.2008.2007095

[75] A. Rietz, "Sufficiency of a finite exponent in simp (power law) methods," *Structural and Multidisciplinary Optimization*, vol. 21, no. 2, pp. 159–163, 2001, doi:10.1007/s001580050180. [Online]. Available: http://dx.doi.org/10.1007/s001580050180

[76] X. E. Yu, Y. Xue, S. Sirouspour, and A. Emadi, "Microgrid and transportation electrification: A review," in *2012 IEEE Transportation Electrification Conference and Expo (ITEC)*, June 2012, doi:10.1109/ITEC.2012.6243464. pp. 1–6.

[77] D. B. Doman, "Fuel flow control for extending aircraft thermal endurance," *Journal of Thermophysics and Heat Transfer*, vol. 32, no. 1, pp. 35–50, Jan. 2017, doi:10.2514/1.T5142.

[78] S. Park and D. Jung, "Design of vehicle cooling system architecture for a heavy duty series-hybrid electric vehicle using numerical system simulations," *Journal of Engineering for Gas Turbines and Power*, vol. 132, no. 9, p. 092802, Sep. 2010, doi:10.1115/1.4000587.

[79] M. Ouchi, Y. Abe, M. Fukagaya, H. Ohta, Y. Shinmoto, M. Sato, and K.-i. Iimura, "Thermal management systems for data centers with liquid cooling technique of CPU," in *IEEE Intersociety Conference on Thermal and Thermomechanical Phenomena in Electronic Systems*, San Diego, CA, USA, 2012, doi:10.1109/ITHERM.2012.6231507. pp. 790–798.

[80] N. Jain and A. Alleyne, "Exergy-based optimal control of a vapor compression system," *Energy Conversion and Management*, vol. 92, pp. 353–365, 2015. [Online]. Available: http://dx.doi.org/10.1016/j.enconman.2014.12.014

[81] J.-K. Kim and R. Smith, "Cooling water system design," *Chemical Engineering Science*, vol. 56, no. 12, pp. 3641–3658, June 2001, doi:10.1016/S0009-2509(01)00091-4.

[82] M. H. Panjeshahi, A. Ataei, M. Gharaie, and R. Parand, "Optimum design of cooling water systems for energy and water conservation," *Chemical Engineering Research and Design*, vol. 87, no. 2, pp. 200–209, Feb. 2009, doi:10.1016/j.cherd.2008.08.004.

[83] C. J. Muller and I. K. Craig, "Energy reduction for a dual circuit cooling water system using advanced regulatory control," *Applied Energy*, vol. 171, pp. 287–295, June 2016, doi:10.1016/j.apenergy.2016.03.069.

[84] D. J. Delia, T. C. Gilgert, N. H. Graham, U. Hwang, P. W. Ing, J. C. Kan, R. G. Kemink, G. C. Maling, R. F. Martin, K. P. Moran, J. R. Reyes, R. R. Schmidt, and R. A. Steinbrecher, "System cooling design for the water-cooled IBM enterprise system/9000 processors," *IBM Journal of Research and Development*, vol. 36, no. 4, pp. 791–803, July 1992, doi:10.1147/rd.364.0791.

[85] J.-K. Kim, G. C. Lee, F. X. X. Zhu, and R. Smith, "Cooling system design," *Heat Transfer Engineering*, vol. 23, no. 6, pp. 49–61, 2002, doi:10.1080/01457630290098754.

[86] H. C. Pangborn, J. P. Koeln, M. A. Williams, and A. G. Alleyne, "Experimental validation of graph-based hierarchical control for thermal management," *Journal of Dynamic Systems, Measurement, and Control*, vol. 140, no. 10, p. 101016, Oct. 2018, doi:10.1115/1.4040211.

[87] D. R. Herber, T. Guo, and J. T. Allison, "Enumeration of architectures with perfect matchings," *Journal of Mechanical Design*, vol. 139, no. 5, p. 051403, May 2017, doi:10.1115/1.4036132.

[88] M. A. Patterson and A. V. Rao, "GPOPS-II: a matlab software for solving multiple-phase optimal control problems using hp-adaptive gaussian quadrature collocation methods and sparse nonlinear programming," *ACM Transactions on Mathematical Software*, vol. 41, no. 1, Oct. 2014, doi:10.1145/2558904. [Online]. Available: http://doi.acm.org/10.1145/2558904

[89] J. T. Betts, *Practical Methods for Optimal Control and Estimation Using Nonlinear Programming. SIAM.*, 2010, doi:10.1137/1.9780898718577.fm. [Online]. Available: https://epubs.siam.org/doi/abs/10.1137/1.9780898718577.fm

[90] K. McCarthy, E. Walters, A. Heltzel, R. Elangovan, G. Roe, W. Vannice, C. Schemm, J. Dalton, S. Iden, P. Lamm, C. Miller, and A. Susainathan, "Dynamic thermal management system modeling of a more electric aircraft," in *Power Systems Conference*, no. Paper no. 2008-01-2886, Nov. 2008, doi:10.4271/2008-01-2886.

[91] E. Ganev and M. Koerner, "Power and thermal management for future aircraft," in *AeroTech Congress & Exhibition*, no. 2013-01-2273, Sep. 2013, doi:10.4271/2013-01-2273.

[92] E. Kim, K. G. Shin, and J. Lee, "Real-time battery thermal management for electric vehicles," in *ACM/IEEE International Conference on Cyber-Physical Systems*, Berlin, Germany, Apr. 2014, doi:10.1109/ICCPS.2014.6843712. pp. 72–83.

[93] J. P. Koeln, M. A. Williams, H. C. Pangborn, and A. G. Alleyne, "Experimental validation of graph-based modeling for thermal fluid power flow systems," in *ASME Dynamic Systems and Control Conference*, no. DSCC2016-9782, Minneapolis, MN, USA, Oct. 2016, doi:10.1115/DSCC2016-9782.

[94] K. L. Moore, T. L. Vincent, F. Lashhab, and C. Liu, "Dynamic consensus networks with application to the analysis of building thermal processes," *IFAC Proceedings Volumes*, vol. 44, no. 1, pp. 3078–3083, Jan. 2011, doi:10.3182/20110828-6-IT-1002.02549.

[95] M. A. Williams, J. P. Koeln, H. C. Pangborn, and A. G. Alleyne, "Dynamical graph models of aircraft electrical, thermal, and turbomachinery components," *Journal of Dynamic Systems, Measurement, and Control*, vol. 140, no. 4, p. 041013, Apr. 2018, doi:10.1115/1.4038341.

[96] H. A. Preisig, "A graph-theory-based approach to the analysis of large-scale plants," *Computers & Chemical Engineering*, vol. 33, no. 3, pp. 598–604, Mar. 2009, doi:10.1016/j.compchemeng.2008.10.016.

[97] D. B. West, *Introduction to Graph Theory*, 2nd ed. Pearson, 2001.

[98] T. H. Cormen, C. E. Leiserson, R. L. Rivest, and C. Stein, *Introduction to Algorithms*, 3rd ed. MIT Press, 2009.

[99] J. Riordan, "The enumeration of trees by height and diameter," *IBM Journal of Research and Development*, vol. 4, no. 5, pp. 473–478, Nov. 1960, doi:10.1147/rd.45.0473.

[100] "A000041," The on-line encyclopedia of integer sequences, https://oeis.org/A000041.

[101] J. D'Errico, "Partitions of an integer," MATLAB File Exchange, 2008, https://www.mathworks.com/matlabcentral/fileexchange/12009.

[102] T. Guo, D. R. Herber, and J. T. Allison, "Reducing evaluation cost for circuit synthesis using active learning," in *ASME 2018 International Design Engineering Technical Conferences*, no. DETC2018-85654, Quebec City, Canada, Aug. 2018, doi:10.1115/DETC2018-85654.